12-2015

Computational Simulation of Mass Transport and Energy Transfer in the Microbial Fuel Cell System

Shiqi Ou
University of Tennessee - Knoxville, sou@vols.utk.edu

To the Graduate Council:

I am submitting herewith a dissertation written by Shiqi Ou entitled "Computational Simulation of Mass Transport and Energy Transfer in the Microbial Fuel Cell System." I have examined the final electronic copy of this dissertation for form and content and recommend that it be accepted in partial fulfillment of the requirements for the degree of Doctor of Philosophy, with a major in Mechanical Engineering.

Matthew M. Mench, Major Professor

We have read this dissertation and recommend its acceptance:

Kivanc Ekici, Feng-Yuan Zhang, Vasilios Alexiades

Accepted for the Council:
Carolyn R. Hodges

Vice Provost and Dean of the Graduate School

(Original signatures are on file with official student records.)

Computational Simulation of Mass Transport and Energy Transfer in the Microbial Fuel Cell System

A Dissertation Presented for the
Doctor of Philosophy
Degree
The University of Tennessee, Knoxville

Shiqi Ou
December 2015

ACKNOWLEDGEMENTS

First of all, I would like to thank my Ph.D. academic advisor Dr. Matthew M. Mench, for providing me the opportunity to pursue a doctoral degree at the University of Tennessee. I can never achieve this step without his guidance, encouragement, support and patience for me.

I would also like to express my appreciation to off-campus advisor Dr. John M. Regan from Penn State University who provided insight and expertise that greatly assisted the research. Also I want to say thank to my PhD committee members: Dr. Kivanc Ekici, Dr. Feng-Yuan Zhang and Dr. Vasilios Alexiades for their instructions, help and support. I gratefully thank the US Army Research Office, which funds me and supports my research. I appreciate the introductions and helps from Dr. Qunlong Dong, who led me to apply my Ph.D. knowledge into the industrial products in the Volvo Trucks North America Inc.

Finally, I want to express my deep appreciation to my parents for the unceasing encouragement, support and attention. I would like to give my special thanks to my wife Shasha Jiang, for all of her love, encouragement and company. I also thank all my lab colleagues and friends in Knoxville and State College, for all the knowledge and happiness we share together.

ABSTRACT

This doctoral dissertation introduces the research in the computational modeling and simulation for the microbial fuel cell (MFC) system which is a bio-electrochemical system that drives a current by using bacteria and mimicking bacterial interactions found in nature. The numerical methods, research approaches and simulation comparison with the experiments in the microbial fuel cells are described; the analysis and evaluation for the model methods and results that I have achieved are presented in this dissertation.

The development of the renewable energy has been a hot topic, and scientists have been focusing on the microbial fuel cell, which is an environmentally-friendly and promising technology. The MFC full cell is a complex system which has different reactions, coupled with mass and electrons transport in bulk liquid. Therefore, this research contains interdisciplinary fields. The methods will be adopted includes: (1) numerical methods (finite volume method/finite difference method/ parallel computation/ multiple step times etc.); (2) computational fluid dynamics method (diffusion equation, Nernst-Planck equation etc.); (3) experimental electrochemical analysis methods; (4) the biological treatment process (biofilm growth, anaerobic/aerobic bacteria etc.). The uniqueness of this work: (1) a comprehensive computational bioelectrochemical fuel cell models was firstly constructed in the research; (2) the primary physical phenomena have been systematically analyzed in both steady and transient states; (3) The simulation evaluated the MFC system which are

hardly obtained directly in the experiments. The computational work in MFC modeling achieved four goals: (1) Characterized the primary factors which affect the MFC performance and used them to describe a complex microbial fuel cell model; (2) Derived a series of appropriate electrochemical /biological /chemical reactions equations for the analysis of the mechanics in MFC; (3) Applied computational methods in the model construction and built a series of sub-models for the MFC system; (4) Simulated the models and compared with the experimental results, gave the analysis for the MFC phenomena which are used for optimizing the design of the MFC system.

TABLE OF CONTENTS

LIST OF TABLES

LIST OF FIGURES

CHAPTER I

INTRODUCTION AND GENERAL INFORMATION

1.1 The Energy and Renewable Energy

The development of modern society and industrialization has caused enormous demands for the human activities: residential, commercial, transportation, industrial, and electric power [1]. The world total energy consumption has increased from 102,569 terawatt-hours in year 1990 to 143,851 terawatt-hours in year 2008, representing a 40.25 % increase in only 18 years [2]. Fossil fuels which are the representative for the traditional energy is the main source for the power supply for a long time, it has occupied more than 80 % of the energy consumption around the world [1] and the demand is substantially increasing after the third Industrial Revolution. The largely depletion of the energy has brought severe environmental problems and the increase of the industrial cost, the first and second oil shocks in 20th century have showed how import the energy is to the human society.

With the consumption of the traditional energy and improvement of the sense of environmental protection, the renewable energy has been a crucial role in energy structure and development pattern for the human society. Based on the REN21's 2014 report, renewables contributed 19 % to our energy consumption and 22 % to our electricity generation in 2012 and 2013, respectively [3]. The renewable energy has become an important and promising part in the energy

structure. The renewable energy source includes biomass, hydropower, geothermal, solar, wind and marine energies [4]. Among the options of the renewable energy, bioenergy is a widely available energy that supplies combustion for motor fuels, electricity power and other fields.

1.2 MFC Technology in Wastewater Treatment

The wastewater treatment plant is a necessary municipal construction, which removes impurities from water by disposal, phase separation and oxidation methods. Since urbanization development after 20^{th} century, the domestic wastewater treatment technology and efficiency have both been improved. However the wastewater treatment still accounts for about 3 % of the U.S. electrical energy load [5]. Therefore the methods to save energy and recycle energy are currently developed by scientists and engineers. The energy-related characteristics of domestic wastewater can be divided into three areas: the energy resource contained in wastewater organics, the external fossil-fuel energy requirements for the production of equivalent amounts of the fertilizing elements nitrogen (N) and phosphorus (P), and the energy that might be gained from wastewater's thermal content [5]. The renewable energy wastewater treatment technology will be helpful for the energy saving and cost reduction in the wastewater treatment industry.

The microbial fuel cell (MFC) research is one of the newest and promising approaches for the electricity generation and energy production in the wastewater treatment field. The electron source of the MFC technology is

domestic wastewater, which is widely and cheaply available in the urban area. This system is ideal for the stationary application in the wastewater treatment plant: the electrons are collected through the biomass by digesting the organic matters; the bioelectricity is generated in the anode and conducted in a closed electric out circuit which is able to supply limited amount of power. Although this interesting phenomenon that the electrons are able to be generated and transferred out of cells by the specific bacteria has been found in around 100 years ago [6], the basic theories for electron transfer by the bacteria and realization for power generation have just been achieved breakthrough results in recent decades. It is known from the name of this wastewater treatment technology that the research approach and analysis methods for it have much in common with the traditional fuel cell technology (e.g. proton exchange membrane fuel cells (PEM fuel cells), solid oxide fuel cells (SOFC)), except some structure differences (e.g. the electrolyte is a bioenvironmental nutrient solution in the wastewater treatment).

1.3 The Mechanism in MFC System

The MFC system is a bioenvironmental reactor with electrochemical and biological reactions which can produce electricity and generate renewable energy. In general, the electrons from the organic matters (e.g. glucose, acetate) are only used for the biomass growth and new cell synthesis by the microorganisms. In the MFC wastewater treatment reactor, however, some specific bacteria are able to transfer electrons outside the cells besides utilize the

electrons for growth and fission. These specific species of bacteria are called as *exoelectrogens* in this dissertation [7]. The *exoelectrogens* in the MFC reactor consume the organic matter under an anaerobic environment in the anodic electrode and transfer extra electrons from the organic matter which acts as the electron donors (e.g., glucose, acetate etc.) in the reactions. The electrons are transported from anodic electrode through the external circuit to anodic electrode, and are reacted with the electron acceptor in the cathode. It is promising to focus on the bioelectrochemical reactions and mass transport mechanisms in the microbial fuel cell to establish a better reactor design to generate more current and power from the wastewater.

1.3.1 Bioelectricity generation

In the natural environmental, a diversity of bacteria has the capability of various extroelectrogenic activities as well as electron transfer efficiencies. Two common *exoelectrogens*: *Shewanella* and *Geobacter* are dissimilar metal reducing genera found by researchers [7]. They both have c-Type cytochromes which are ubiquitous in nearly all living organisms, where they play vital roles in mediating electron transfer reactions associated with respiration [8]. In the general MFC experiments, the *exoelectrogens* are not isolated unless specific species is studied. Previous work has showed that a mixture bacteria culture in the MFC reactor produces more power than pure bacteria cultures [9]. The free-floating microorganisms cluster on the electrode (anode and cathode) surfaces and form a thin living film named as biofilm (Both anaerobic bacteria and aerobic

bacteria have the biofilm features). In the biofilm, the adherent bacteria cells are frequently embedded within a self-produced matrix of extracellular polymeric substance (EPS) which is supposed to be electrically conductive [10]. In the anode, the EPS is a significant contributor to electron transport across the biofilm to the electrode [7]. In some experimental and modeling publications, the electrons were thought to be transferred by the added chemical mediators which could carry electrons from inside the cell to exogenous electrodes [11]. This hypothesis was not challenged until year 1999 when it was realized that the added chemical mediators are unnecessary in the electron transport [12]. Presently, two mechanics are believed to explain the electron transport on the cell surface in the MFC system: electron shuttling via self-produced mediators or membrane-bounded electron carriers [7].

1.3.2 Structure classification

With the development in the MFC technology, scientists have created different structures of MFC reactors for experiments in the laboratories. MFC classification is based on the reactor architecture, cathode reaction or anode cultures or other features. According to the reactor architecture, the MFC is divided into: two-chamber MFC (Figure 1.1 (a)); and single-chamber MFC (Figure 1.1 (b)). The two-chamber MFCs have two separate reactors (anode reactor and cathode reactor) which are connected by a tunnel. The protons or cations are able to exchange through the Proton Exchange Membrane (PEM) or Cation Exchange Membrane (CEM) which is located in the connect tunnel,

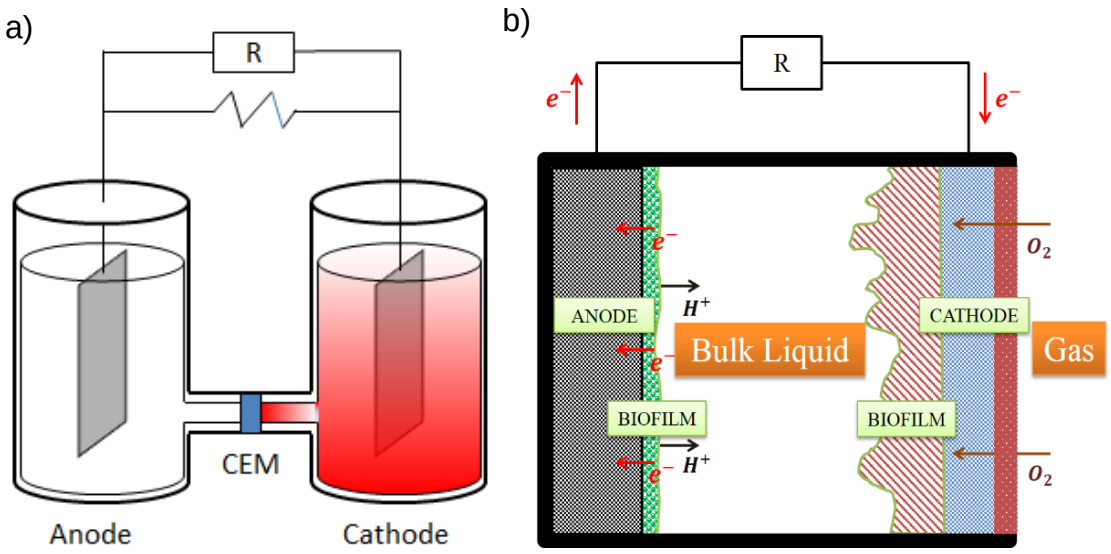

Figure 1.1 MFC reactor structures: (a) Two-chamber reactor, (b) Single-chamber air-cathode reactor.

shown in Figure 1.1 (a). The structure of the single-chamber MFCs is simpler and has significantly lower internal resistance compared to the two-chamber MFC. Since the single-chamber design shortens the distance between anode and cathode which reduces the ohmic resistance, the experimental results presented that the single-chamber MFC is able to generate more power than the two-chamber MFC does [7]. Because of the separation of the anodic reactions and cathodic reactions in MFC, the two-chamber MFCs are tend to be used for power generation and bioelectrochemical reaction mechanism analysis [13, 14]. Additionally, there are different electron acceptors in the cathodic electrode for different types of MFCs. Different chemical species can work as the electron acceptors such as oxygen [15], ferricyanide [16, 17], per chlorate [18], or nitrate [19, 20]. Among these electron acceptors in MFC cathode, oxygen is one of the most common oxidizers. The oxidation reaction of oxygen is simple and oxygen is easy to be access to comparing with other oxidizers (e.g., permanganate, ferricyanide) [7]. Besides the structural classification for MFC reactor, it can be classified by the anodic bacteria cultures as well, such as MFC reactor with mixture bacteria, MFC reactor with *Shewanella* and *Geobacter*, etc. Since the mixed bacteria cultures generally perform better in MFC reactor than individual culture works, the microorganism cultivated in the MFC reactor in our research experiments is directly from the local wastewater plant.

Figure 1.2 shows the 3D structure of the single chamber air-cathode MFC reactor which is adopted by our experimental and modeling research. This

reactor is 4×4×4 cm cubic container, and the hollow part is a cylinder with 4 cm long and 3 cm diameter. The bulk liquid is filled into the reactor hollow cylinder, and the bulk liquid is used for supplying electrons for the anodic biomass reactions, balancing the pH, and creating an anoxic environment for anodic biomass. Similar to analysis for the fuel cell research, the MFC reactor is generally broken down into three structure parts: bulk liquid as electrolyte part, anodic electrode part, and cathodic electrode part. (shown from left to right in Figure 1.2). The *exoelectrogens* accumulate, attach to the anodic carbon paper surface (the anode carbon paper was changed to the graphite fiber brush for the cathodic reactions research.) and form the biofilm which convert and transport the electrons to anodic electrode. The electrons are collected by the current collector on the anode and transported to the external loaded resistance. The circuit connects into the cathodic current collector so that the electrons are able to transport to the cathode and have reduction reactions with the oxygen in cathode materials.

1.3.3 The electrodes and electrolyte in MFC

The bulk liquid works as the electrolyte in the MFC reactor, the bulk liquid also supplies the microorganisms the necessary nutrients: organic matters. The acetate was adopted as the dominant substrate for the biomass growth and electron donors in the MFC reactor in both experimental and modeling research. The buffer solution is added to adjust the pH environment and to improve the conductivity of the electrolyte in MFC reactor, different buffer solutions would be

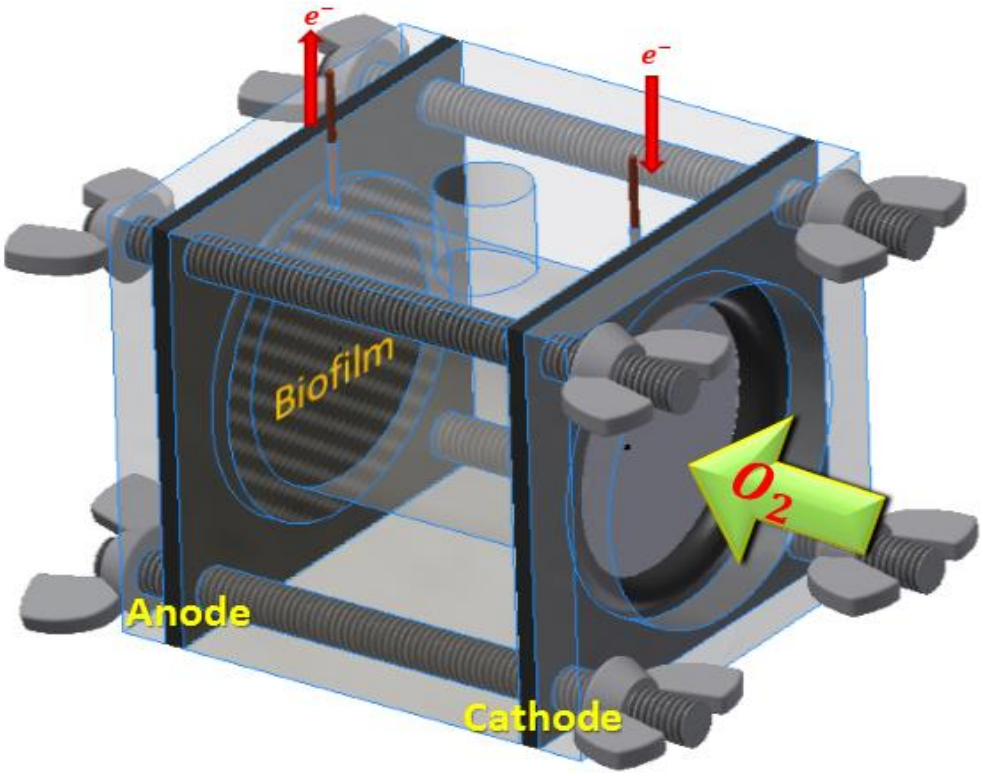

Figure 1.2 Single chamber air-cathode reactor structure.

tested and compared in our research. In the anode, most electrons from the acetate are used for the new cell synthesis, and the remaining electrons are transported from acetate to the electrode in the biofilm. The biofilm thickness is influenced by the reactor microenvironments and parameters (biofilm attachment coefficient and fluid flow velocity in reactor [7]). In the MFC reactor, the anodic biofilm is the place where the electrons converted, and the cathodic biofilm is for the biological oxygen consumption reactions. The change of the biofilm growth and density in both anode and cathode is a significant factor to the MFC power generation. The MFC transient model will focus on the biofilm growth in MFC reactor. In the MFC modeling filed, the MFC performance affected by the cathodic parameters was rarely simulated, though the cathode reaction has been shown to limit the overall power generation of many MFC systems in some experimental research [21-24]. In the air-cathode reactor, oxygen functions as the electron acceptor and is reduced in the metal catalyst layer, typically with the Platinum (Pt) catalyst in the carbon cloth. Besides the metal catalyst, the cathodic biofilm is also able to catalyze cathode oxidation, though it seems to contribute relatively little to the external current [25]. In addition, the abiotic regions of common air-cathode designs do not comprise a homogeneous layer; these multiple layers differentially affect gas- and liquid-phase mass transport through the cathode [16].

1.4 Computational Tools for Modeling

The research in the MFC technology focused more on the biological experiment, while the fundamental mechanisms of mass transport and electrochemical reactions should be valued. The goal of this research is to develop a mechanistically based, multispecies microbial full-cell model to explore the phenomena in the MFC reactor and to validate the hypotheses derived from experimental data. To realize the systematical modeling for the MFC system, the thoughts of software development were adopted in this process.

Different commercial software, mathematical methods and programming languages were applied for the MFC model series development. At initially stage, the commercial software MATLAB was used for the anodic transient model and the simulation software COMSOL was adopted for 2-D steady state model. With more equations added and more conditions considered in the MFC model, the operating speed greatly limited the simulation. At the same time, in order to manually distribute the computing threads and space, the C++ programming in Linux system with parallel computing method was applied for later on MFC modeling work. One of the parallel computing – OpenMP was utilized into the model coding to use multiple threads and to speed up the simulation calculation. The computing work was realized by the high performance computer – NEWTON which is a cluster computing system designed for use by researchers at the University of Tennessee, Knoxville. The high performance computing efficiently improved the calculating speed and also simplified the procedures for modifying

the modeling codes. The research also applied with the GIT for the MFC model series development. The GIT is a distributed revision control system that traces, integrates and stores the programming workflows, therefore it is useful for the modeling application by changing and adding further parameters and equations into the MFC model codes during the development process. A series of MFC models with C++ coding in Linux system were developed based on the GIT, the model system became more complex and contained more equations and parameters to explain the performance and internal relations in the MFC reactor.

It is common that the MFC experiments take at least several weeks or even months for the biomass growth in the reactor before the stable power output is achieved. The computational models have the ability to validate the hypotheses and optimize the MFC design by shortening the running period for the research, which provides a strong incentive for pursuit of this work. The computational simulation work was meaningful and valuable to improve the design of the MFC technology.

1.5 Dissertation Organization

The statement of this dissertation is based on the model series of the single chamber air-cathode MFC reactor: anodic model, cathodic model and full cell model. In every chapter for the model description, it includes the methods, algorithms, results and discussions. This dissertation is organized with a literature review for the MFC technology progress and bioelectrochemical model development in Chapter II, the model construction and analysis for anodic half-

cell in MFC in Chapter III, the model construction and analysis for cathodic steady state half-cell in MFC in Chapter IV, cathodic transient state half-cell in Chapter V, and the MFC full cell steady state model construction and the buffer system analysis in Chapter VI.

CHAPTER II

LITERATURE REVIEW

The computational modeling has been widely used in different disciplines, the primary function of a model is to reduce a complex system to the minimum terms essential for its description so that those terms may be manipulated, thereby helping the researchers to know how the system will respond under a variety of conditions to improve the design and understand the internal relations of the system [26]. Before starting the model construction for the MFC reactor, the knowledge in chemical, electrochemical and biological relations, MFC structure and the features of the electrodes/electrolyte materials should be studied and measured.

2.1 Biofilm and MFC Models

Numerical simulation has been applied for the MFC regional design and analysis such as the biofilm growth on the anode [27], and the electrochemical reactions in MFC [10]. The initial MFC models started from the simulations on the steady-state biofilm growth, and developed into multi-factor transient mixed-culture states of electrochemical reactions and bacterial growth processes [28, 29]. Rittmann et al. [28] presented the steady-state biofilm film with the Monod relation which described the substrate utilization at any location in the biofilm. The Monod equation is shown in Eqn. (2.1).

$$\frac{\partial S_f}{\partial t} = -\frac{kX_f S_f}{K_S + S_f} \tag{2.1}$$

where S_f is the rate-limiting substrate concentration in the anodic/cathodic biofilm ($M_S L^{-3}$), K_S is the half-velocity coefficient ($M_S L^{-3}$), k is the maximum specific rate of substrate utilization ($M_S M_X^{-1} T^{-1}$), and t is the time (T) (The unit of the time is generally “day” since the biofilm growth is a slow process, while the time unit is transferred to “second” in the MFC modeling since the electrochemical changes are instantaneous reactions). Wanner et al. [29] highlighted the complex, transient, 1-D microbial biofilm growth process which considers nutrient consumption, multispecies competition, and electrode materials. In the MFC reactor, the mass transport is a significant impact. The biofilm change process is considered as an advective flux in the simulation. Additionally, the transport process of the chemical components is modeled as an effective diffusive flux [30]. The biofilm simulation becomes more complex when considering the biofilm liquid phase volume fraction, detachment and attachment of cells, as well as the mass transport of dissolved components in bulk liquid and biofilm [31], as illustrated in Figure 2.1.

Besides, some other factors in the reactor such as local electrochemical conditions and proton (H^+)/hydroxide (OH^-) transport are important to system performance and biofilm growth. The bacterial growth in MFC system does not only depends on nutrient concentration but also relies on other elements such as the local electrical potentials [9], the local pH environment [22, 32, 33], the microbial community composition [34], and the extracellular electron transfer (e.g. EPS conductivity) [35]. The modeling in MFC system becomes quite

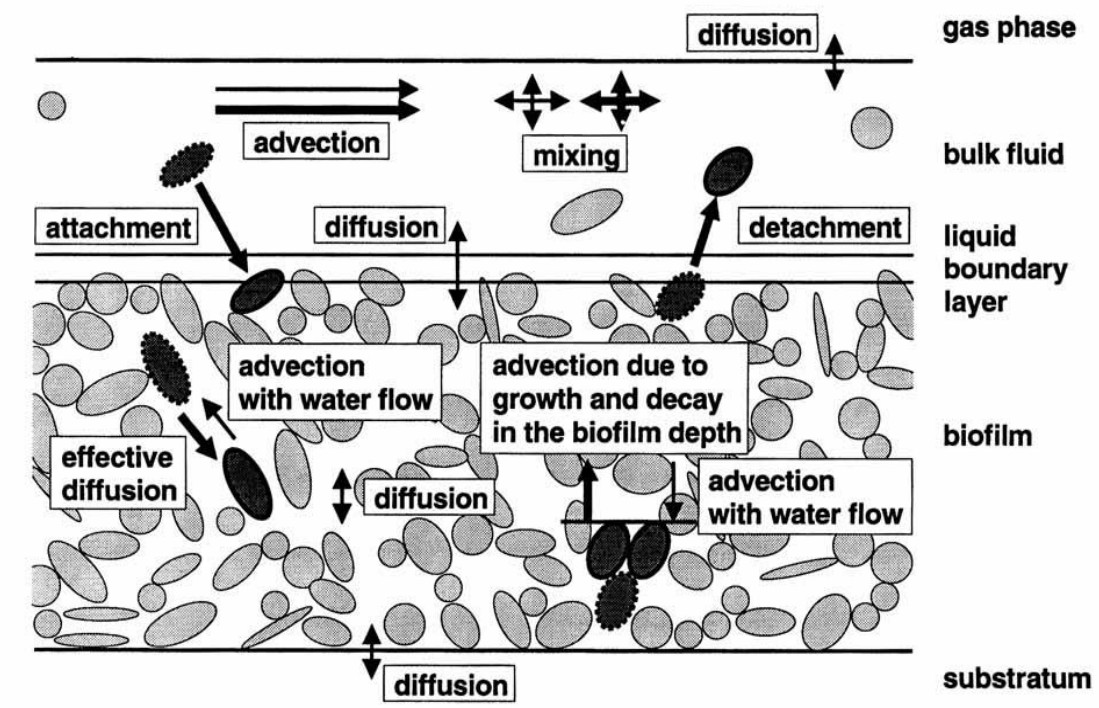

Figure 2.1 Transport processes considered in the mixed-culture biofilm model. Thick arrows refer to particulate, thin arrows to dissolved components. [30]

complex with more elements and impacts are taken into account, therefore most modelers only consider a regional part simulation in MFC reactor, resulting in few developed for the full cell models [10, 27]. The biofilm-focused model developed by Picioreanu [27] successfully described three-dimensional biofilm growth as well as current density and power production. However the electrochemical reactions for electrons transfer at the anode surface are simplified through the oxidized/reduced mediators, the equation is shown in Eqn. (2.2). While it has been recognized that the mediators did not need to be added for the electron transfer [12].

$$\mathrm{M_{red}} = \mathrm{M_{ox}} + 2\mathrm{H^+} + 2\mathrm{e^-} \tag{2.2}$$

The relation of current density and reaction rate of oxidized/reduced mediators are expressed as:

$$\mathrm{M_{red}} = -\frac{\mathrm{i}}{2\mathrm{F}}, \mathrm{M_{ox}} = \frac{\mathrm{i}}{2\mathrm{F}} \tag{2.3}$$

Although Picioreanu et al. [27] successfully built the anode based MFC model and the relations with the chemical substances in reactor, the model did not reflect its essence attribute of the electron transfer of the biomass in the anode. Therefore Torres et. al. [36] studied the protons transport within the anodic biofilm and considered the diffusion and electric migration influence in the mass transport equation. Marcus et. al. [10] built the anodic model based on the conductive biofilm and presented the relation between the biofilm growth and biomass concentration.

Most of these steady state or transient models focused on the anode local mass transport or electrochemical performance, the cathode reactions were usually simplified to one oxygen reduction reaction (ORR) in the full-cell system simulations. Although the model designed by this method gives a general simulation in the electron flow trends, the mutual influence from both the anodic and cathodic parameters has to be ignored. The goal of this PhD research is to develop a series of computational models including the regional models for both anodic and cathodic electrodes and the comprehensive full cell model which reflects the overall performance from all parts in the MFC reactor.

2.2 MFC Materials

A single-chamber air-cathode reactor is adopted as the MFC structure during the PhD research for both experiment and computational modeling work. The single chamber air-cathode MFC is a simple structure conducive to scale-up and can generate relatively higher power compared with other MFC designs. There are some requirements for the anode materials: highly conductive, non-corrosive, high specific surface are, high porosity, non-fouling, inexpensive, and easily made and scaled to larger sizes [7]. In the single-chamber reactor, the anode is generally made of graphite brushes. The graphite brushes can supply higher specific surface area and higher porosity compared to the flat plate graphite structure [7] . These advantages can induce anode *exoelectrogens* to form more biofilm on the anode to generate as much electricity as possible. The

cathode material is generally made up of the carbon paper pre-loaded with a platinum catalyst on one side [7].

The materials and cathodic structure also affects the power generation and organic substrate removal in MFCs [24]. On the one hand, the cathode materials should allow the oxygen transport into the reactor efficiently and have a low ohmic resistance to reduce the ohmic overpotential; on the other hand, the materials should reduce the water leakage from the reactor. Santoro et al. [24] compared three groups of cathode materials and examined the MFC performance in the reactors with different cathode, it concluded that the three-layer (GDL, micro porous layer (MPL) and CL) as cathodic materials had a low ohmic resistance and produced a high cathode open circuit potential.

2.3 Limitations in the MFC Reactor

2.3.1 Electrochemical relations

The MFC system is a special fuel cell, the analysis methods in the electrochemical field and electricity generation for the MFC system are the same as other types of fuel cells. The polarization curve, which represents the cell voltage-current relationship, is the standard figure of merit for evaluation of fuel cell performance. Voltage versus current density, scaled by geometric electrode area, is typically shown, so that the results are scalable between differently sized cells [37]. The potential loss of the fuel cell can be divided into 5 parts: activation overpotential, ohmic overpotential, concentration overpotential, the loss that

represent the departure from the Nernst thermodynamic equilibrium potential, and the loss represent the departure from the maximum thermal voltage. The five regions labeled on the polarization curve of Figure 2.2 [37]. The relations for the cell voltage V_{cell} and various polarizations:

$$V_{cell} = E^0(T,P) - \eta_{act,a} - |\eta_{act,c}| - \eta_r - \eta_{con,a} - |\eta_{con,c}| - \eta_x \quad (2.4)$$

$$V^0(T,P) = E_C^0 - E_A^0,\ \eta_x \approx 0 \quad (2.5)$$

where $V^0(T,P)$ is the theoretical equilibrium open-circuit potential of the cell, calculated from the Nernst equation; E_C^0 is the equilibrium cathode voltage and E_A^0 is the equilibrium cathode voltage (V); $\eta_{act.a}$ and $\eta_{act.c}$ are activation overpotential in anode and cathode, respectively; $\eta_{con,a}$ and $\eta_{con,c}$ are concentration overpotential in anode and cathode, respectively; η_r is the ohmic overpotential in reactor, η_x is the departure from the Nernst equilibrium voltage.

2.3.2 Oxygen mass transport limitations

The air-cathode MFC reactor also has oxygen reduction reaction (ORR) in the cathode, which is the same as PEM fuel cells. Traditionally the oxygen reduction reaction (ORR) in an MFC was thought that oxygen has reactions with protons transported from the cathodic current collector. The reaction is presented in Eqn. (2.6) which is also found in a polymer electrolyte fuel cell, as Eqn. (2.6) shows:

$$0.25O_2 + e^- + H^+ \rightarrow 0.5H_2O \quad (2.6)$$

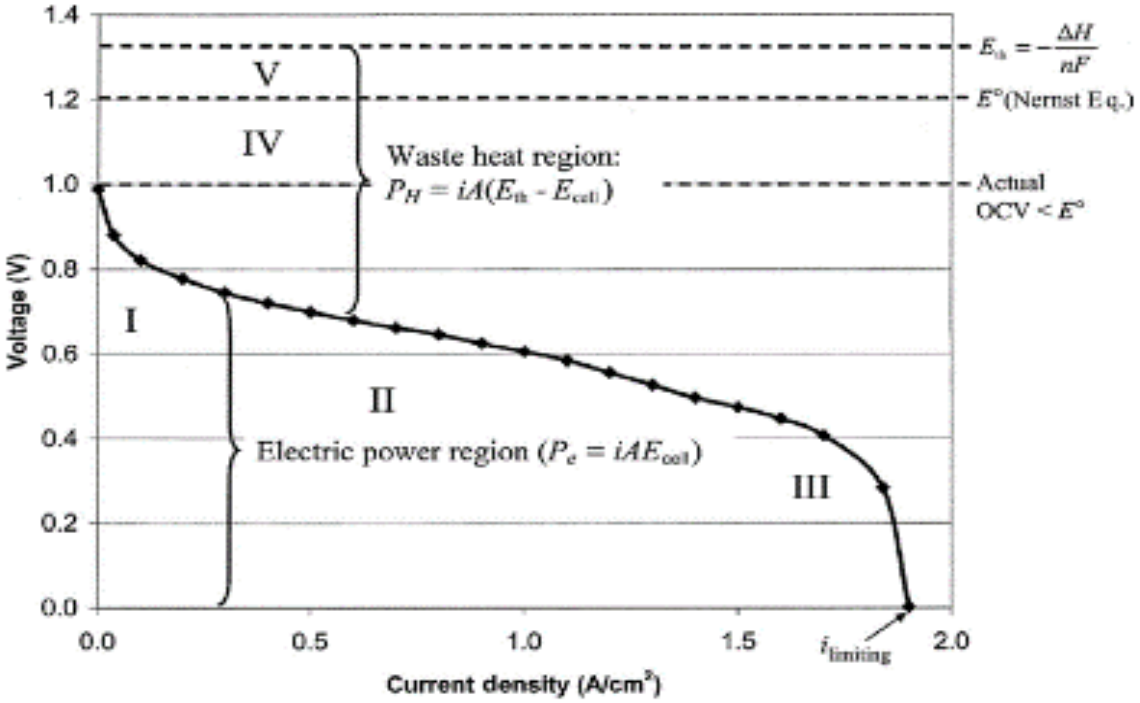

Figure 2.2 Typical polarization curve for fuel cell with significant kinetic, ohmic, concentration, and crossover potential losses. [37]

It is regarded that the hydroxide ions govern potential losses in the cathode catalyst layer in recent research [22, 23]. The ORR follows Eqn. (2.7). Biofilm growth at the cathode surface affects the distribution of hydroxide and other ions [15], and the resultant pH strongly affects Pt-catalyzed oxygen reduction, microbial growth, and overall power generation [18]. Thus, hydroxide and oxygen transport in the cathode should be considered in MFC cathode models.

$$0.25O_2 + e^- + 0.5H_2O \rightarrow OH^- \qquad E^0 = +0.40\ V \tag{2.7}$$

Oxygen transport is another significant limitation for the MFC system performance. In the fuel cell field, Benziger et al. [38] examined the oxygen transport across the cathode gas diffusion layer (GDL) in PEM fuel cells by varying the O_2/N_2 ratio and the area of the GDL. The same phenomenon is found in the MFC reactor: the oxygen transports through the MFC cathode layers and reacts as the electron acceptor in ORR, the amount of oxygen concentration and transport speed of oxygen both influence the cathodic ORR and change the MFC performance [39]. It concludes that the oxygen diffusive coefficient in the gas for air-cathode MFC reactor is the possible factor that affects the power density in MFC [39].

2.3.3 pH environment in MFC reactor

In the single chamber air-cathode MFC reactor, the mixed bacteria cultures need a moderate pH environment for biological growth and minimization

of electrochemical overpotential. Therefore the study of pH in the environment in MFC reactor and the buffer solutions for adjusting the pH is necessary in the MFC technology.

Jung et al. [40] studied the impedance characteristics and polarization behavior of the MFC along with the change of pH and found that pH oppositely influences anode and cathode performance. He et al. [41] measured the electricity production by comparing the pH influence to the anodic and cathodic reaction rate. The microbial activities preferred to have a neutral pH while the cathodic reaction was improved by higher pH. The protons (H^+) are accumulated in the anode biofilm and the hydroxides (OH^-) are accumulated in the cathodic reactions. The proton and hydroxide transport in the single chamber mutually affect the electrodes. The buffer solutions are applied to adjust the pH environment to supply a good MFC performance. Popat et al. [42] simulated the buffer solutions for improving the oxygen reactions in the cathode, and Picioreanu et al. [33] simulated the buffer solutions for adjusting the pH environment in MFC anode in a transient state.

In following chapters, the models will be addressed for the anode, cathode and full cell reactor. The limitations and factors will be contained in the models: the biofilm growth limitations by the chemical substance, the oxygen transport and oxygen reactions in different cathodic materials, the buffer solutions and pH environment comparisons in the whole reactor.

CHAPTER III

ANODIC HALF-CELL MODEL IN MFC

In the research, the MFC system model includes both anode and cathode which can influence the overall energy generation, bulk liquid nutrient consumption, reactant transport to the electrodes, and proton transfer. The PhD project focused on the anode model, cathode model and full cell model including the anions/cations, solvable nutrients and buffer chemical solutions in the reactor which influence to the whole system. The MFC model has two mutually supportive tasks which are also based on the air-cathode MFC structure: (1) the biofilm growth which mainly consists of anode-respiration-bacteria (ARB) (e.g., *Geobacter* or *Shewanella*), and (2) the design of an MFC air-cathode model exploring the effects of cathode mass transport and biomass growth on the overall system performance. The procedure for the mode development in MFC system are : a) Adopt reasonable assumptions based on physical structure and materials; b) Analyze electron transfer based on mass transport; c) Derive the mathematical electrochemical/biological equations and build the mass transport governing equations; d) Adopt appropriate numerical methods for simulations, shown in Figure 3.1.

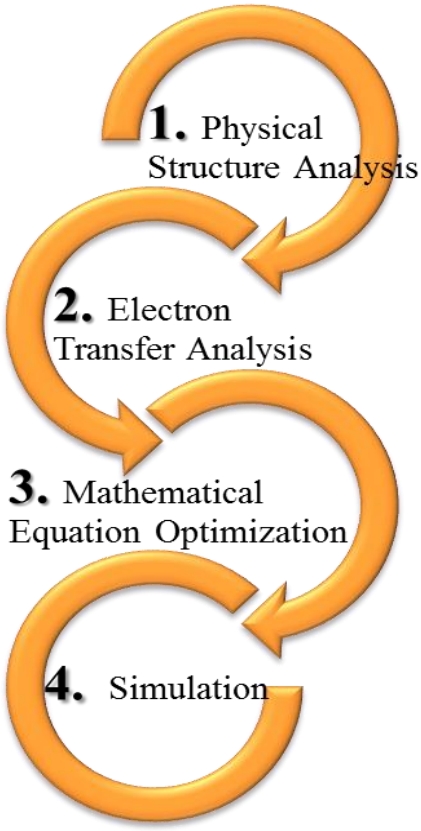

Figure 3.1 Simulation process for the MFC system.

3.1 Methods for Anodic Electrode Model

In the anode biofilm, the ARB consumes the electron donor (acetate) and transports the electrons from the acetate to the anodic electrode and to the biomass growth. An appropriate model for the anodic electrode was constructed to describe and to analyze the relationships for the parameters. It has been proved that extracellular mediators are not necessary for electron shuttling in MFCs, but the mechanism behind electron transport is still unknown and a topic of interest in molecular biology [21]. Research has shown that ferric iron reduction by *Shewanella* involves membrane-bound electron carriers [7]. However the competition among bacteria for the anode surface which is the main electron generation area has not been examined yet [7]. Bacteria “nanowires” are now considered as conductive appendages for both *Geobacter* and *Shewanella* species [35, 43]. The unique extracellular electron transfer ability of the dissimilatory metal-reducing bacteria is significant to improve the current density of microbe-catalyzed electrode reactions [44].

The MFC microorganisms were inoculated from wastewater implies the presence of a mixed microbial population, including methanogenic, anodophilic, and anaerobic microorganisms [45]. Only some of these microorganisms can generate electricity. The microorganisms which are able to generate electricity is the research object in this anode model. The distribution and the morphologic change of the microorganisms can impact the MFC performance, the design for the specific surface area; and anodic material porosity can change the power

density [46]. Figure 3.2 shows the structure of the MFC anode in this model. There are three domains in anode: anode metal (electrons collection), graphite plate and anodic biofilm. The graphite fibers and brushes are the common anodic design for MFC reactor in a single chamber air-cathode MFC which has the highest specific surface area and porosities for *exoelectrogens* growth [7]. However in this model, the biofilm is attached to the planar surface instead of graphite fiber brush's anode structure. This design avoids the affects from the irregular shape of the graphite fiber brush to the fluid flow and the biomass attached coefficient which leads to the mathematical description difficulty.

In the anode model, some assumptions need to be made so that the mathematical model can be reasonable and applied to explain the anodic phenomena in the MFC system. The microorganisms were batch-fed a pH-buffered medium containing 1.0 g/L sodium acetate as the sole electron donor. Suspended bacteria growth in the bulk liquid was neglected this model. The system coulombic efficiency changes with time as the biofilm grows and develops, and has been reported over a large range from 0.04 % to 97 % [45]; a constant anodic coulombic efficiency 80 % was assumed here to simplify the stoichiometric relations for anode biofilm growth. Therefore, 20 % of acetate-derived electrons were consumed by the anode-respiring bacteria (ARB) for endogenous respiration and new biomass growth, while the remaining 80 % were conducted to the anode through the EPS and *exoelectrogens*, as shown in Figure 3.2. This model was for 4 × 4 × 4 cm cubic reactor that the velocity of fluid

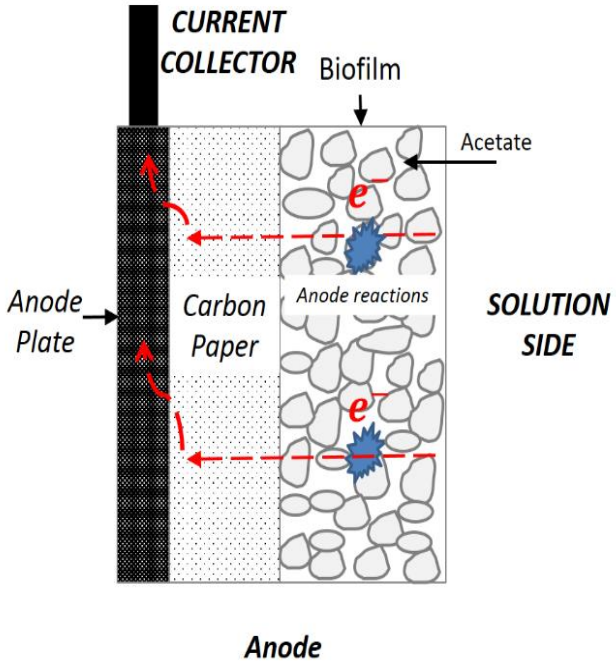

Figure 3.2 Schematic of MFC anode side.

flow is reasonable to be zero. The anodic steady state model focused on the MFC performance from different terms (diffusion, electric field, and advection) in the mass transport. The growth rate of biofilm thickness was assumed to be balanced with the decay rate of biofilm thickness in this steady state model, which the biofilm was assumed to be fully grown and has a constant (0.01 mm in this model [27]). The anode transient model focused on the anodic biofilm growth, acetate concentration changes in the bulk liquid and within the biofilm due to biofilm consumption, and anode reduction by ARB. In this transient model, the anode reduction was simulated to be conducted by the diffusible mediators and the biofilm's EPS was assumed as a self-produced mediator. The total mediator concentration in the anode was assumed to be 1.0 mM, and the initial acetate concentration was 0.1 g/L. In this anode half-cell model (both steady state model and transient model), the cathodic potential was fixed so the influence from the cathode electrochemical changes were neglected in the calculations.

3.1.1 Current generation

Electricity generation is the most important measurement index in determining MFC performance. MFC structure design and analysis of the electron transport mechanism are both carried out to improve the current and power output of MFCs. In Picioreanu's paper [27], the anode model considered only one bacteria species in the anode biofilm. The biofilm in this model consisted of active ARB and inactive ARB, and the increase of its thickness was

by consuming acetate when the growth rate of biofilm thickness was larger than the biomass decay rate. The active ARB obtained the electrons by the transport of electron mediator which was reduced, and was then oxidized at the anode surface. The chemical process is shown in the Eqn. (2.2). Eqn. (2.2) reveals that the mass of the added mediators is neither increased nor decreased in the reaction, which process is the same as the self-produced electron shuttling in the ARB.

According to the electron mediator relation with current density (Eqn. (2.3)), and the Butler-Volmer equation for current density [37], the current density can be derived by the following function [47]:

$$i_j = i_{0,ref}\left(\frac{c_{E,Mred}}{c_{ref,Mred}}\right)\left(\frac{c_{E,Mox}}{c_{ref,Mox}}\right)^{-1}\left(\frac{c_{E,H}}{c_{ref,H}}\right)^{-2} \times \left[e^{\left(\frac{2.303}{b}\eta_{act,a}\right)} - e^{\left(-\frac{2.303}{b}\eta_{act,a}\right)}\right] \quad (3.1)$$

where i_j is the current density on the anode surface (A/m^2), $i_{0,ref}$ is the exchange current density in anode (A/m^2), c_E is the concentration for oxidized/reduced mediators and protons (mol/m^3) on the anode surface, c_{ref} is the reference concentration for oxidized/reduced mediators and protons (mol/m^3), b is the Tafel coefficient, $\eta_{act,a}$ is the activation overpotential in anode (V).

The electrons for the current in this MFC system are collected at the anode surface. Let the anode contact surface area to be A_S, the current can be integrated from the current density distributed at the anode local surface:

$$I = \int_{A_s} \sum_j i_j \, dA_S \quad (3.2)$$

where I is the current (A), and A_S is the anode surface area (m^2).

According to the Eqn. (2.4), the operating voltage of an MFC is represented as the departure from ideal voltage caused by the various polarizations, similar to other fuel cell systems. The limiting current is a result of the combined effect of all polarization in the system, which includes ohmic, kinetic, mass transfer, and crossover or shorting [37].

Because only the anodic parameters were considered in this half-cell model, the cathode voltage was assumed to be a constant. The cathode voltage V_C is:

$$V_C = E_C^0 - |\eta_{act,c}| - |\eta_{con,c}| \tag{3.3}$$

The cell voltage V_{cell} is

$$V_{cell} = IR_{ext} \tag{3.4}$$

where R_{ext} is the external loaded resistor (Ω). The ohmic overpotential is

$$\eta_r = IR_{int} \tag{3.5}$$

where the R_{int} is the total internal resistance from anodic materials, cathodic materials, and bulk liquid. The anode concentration overpotential $\eta_{con,a}$ is calculated by the Eqn. (3.6) [48]:

$$\eta_{con,a} = \frac{RT}{2F} \ln \frac{c_{Mox} c_H^2}{c_{Mred}} \tag{3.6}$$

where R is the gas constant (8.314 J/(mol·K)), T is the reaction temperature (298.15 K), and F is the Faraday constant (96485 C/mol). Combining with Eqn. (2.4), the anode activation overpotential is calculated by Eqn. (3.7) [27]:

$$\eta_{act,a} = V_C - I(R_{int} + R_{ext}) - \left(E_M^0 + 0.059\text{pH} + \frac{0.059}{2} \log \frac{c_{E,Mox}}{c_{E,Mred}}\right) \tag{3.7}$$

where the E_M^0 is the redox potential for electron mediator in anode (V), and is the pH value is the anode.

3.1.2 Reactions in bulk liquid & anode biofilm

Since it was assumed that only ARB exits in the anode model, all the acetate was consumed only by this *exoelectrogens* for cell synthesis and current generation. Figure 3.3 shows the electrons transport path from the electron donor (acetate) to Electron acceptor or debris [26]. If both the biomass production rate and the fraction of electrons in each path are known, the number of electrons transported from the acetate to the anode is able to be derived. With the acetate utilization rate calculated by the Double-Monod equation, the biomass production rate is obtained according to the relevant stoichiometry relation (Eqn. (3.9)). In this model, the fraction of electrons from the electron donor used for energy generation to support cell synthesis was assumed to be fe^0 = 0.90. Eqn. (3.8) presents the acetate oxidation equation [49]:

$$CH_3COO^- + 4H_2O \rightarrow 2HCO_3 + 7H^+ + 8e^- \quad (3.8)$$

Combined with the electron mediator relations in Eqn. (2.2), the stoichiometry relation can be derived by the following reaction:

$$\text{Acetate} + Y_{Mox}M + Y_N NH_4^+ + Y_W H_2O \leftrightarrow$$

$$Y_X \text{Biomass} + Y_{Car} HCO_3^- + Y_{Mred} MH_2 + Y_H \quad (3.9)$$

According to the Double-Monod equation [26], the acetate utilization rate was described by the Eqn. (3.10).

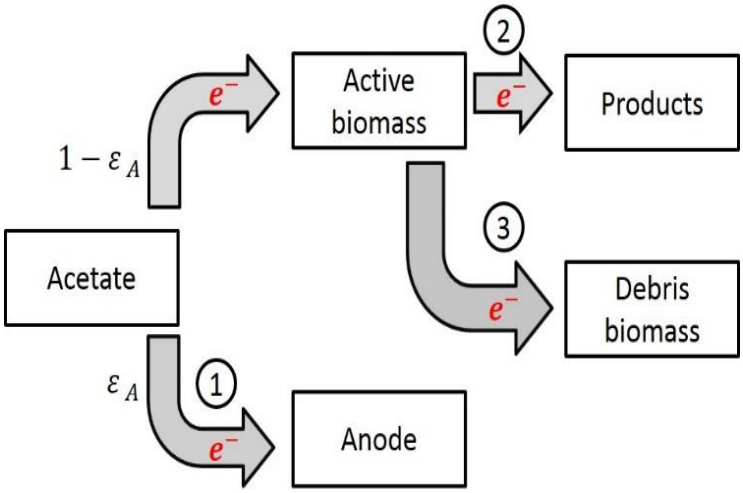

ε_A: Fraction of electrons donated to anode;
Path 1: Electrons transferred from acetate to anode through biomass;
Path 2: Electrons used for endogenous respiration;
Path 3: Electrons terminating in inactive biomass;

Figure 3.3 Electron transfer paths in MFC anode side.

$$r_{Ac} = -q_{Ac,\,max} c_B \frac{c_{Ac}}{K_{Ac}+c_{Ac}} \frac{c_{Mox}}{K_{Mox}+c_{Mox}} \tag{3.10}$$

where r_{Ac} is acetate reaction rate (mol/(m^3·s)), $q_{Ac,max}$ is the maximum specific rate of acetate utilization (mol Acetate/(g Biomass·s)), c_B is the active biomass concentration (g/m^3), c_{Ac} is the acetate concentration (mol/m^3), K_{Ac} is half-maximum-rate for acetate concentration (mol/m^3), c_{Mox} is the oxidized mediator concentration (mol/m^3), and K_{Mox} is the half-maximum-rate for oxidized mediator concentration (mol/m^3). The biomass growth rate, the reduced mediator production rate, and the oxidized mediator consumption rate were calculated based on their respective stoichiometric relations. In the biofilm growth modeling process, some ARB reproduction become new active biomass and benefit the electron transfer, while some ARB become inert biomass debris due to the decay rate [26]:

$$r_{decay} = f_D b_{decay} c_B \tag{3.11}$$

where r_{decay} is the biomass decay rate (g/(m^3·s)), f_D is the fraction of cells contributing to debris, and b_{decay} is the decay coefficient (s^{-1}).

Though most *exoelectrogens* exist in biofilm, while with the effect of the liquid flow, temperature change or biofilm growth etc., a few of them detach from the biofilm and suspend in the bulk liquid. A parameter is used to estimate the detachment rate of biomass to the bulk liquid, which is called the detachment velocity coefficient κ_{det}. The equation for calculating the detachment rate shown in the Eqn. (3.12) [31].

$$u_{det} = \kappa_{det} \frac{L_f^2}{\rho} \tag{3.12}$$

where κ_{det} is the detachment velocity coefficient (g/(m^4·s)), L_f is the biofilm thickness (m), and ρ is the individual microbial density (defined as the mass divided by the volume of the cell) (g/m^3).

3.1.3 Mass balance in bulk liquid & biofilm

In the wastewater treatment, the motion of chemical substance in fluid usually involves diffusive, convective transport [50]. In the electrochemical physical system, the flux of ions also under the influence of the electric field [51]. The mass transport for the charged chemical substances in a fluid environment is affected by the advection, diffusion concentration gradient and electric field, and this equation is called as Nernst-Planck. While the advection term was not included in this model since the fluid flow is reasonably assumed to be zero in the 4 × 4 × 4 cubic reactor. The mass transport equation is shown in the Eqn. (3.13).

$$\frac{\partial c_i}{\partial t} = -\frac{\partial}{\partial x}\left(F_{diff} + F_{mig}\right) + r_i \tag{3.13}$$

The F_{diff} is the diffusion flux term:

$$F_{diff} = -D_i^{eff}\frac{\partial c_i}{\partial x} \tag{3.14}$$

The F_{mig} is the electric migration flux term [36]:

$$F_{mig} = -\frac{z_i F}{RT} D_i^{eff}\frac{\partial V}{\partial x} \tag{3.15}$$

where i is the charged chemical species, c_i is the species concentration, D_i^{eff} is the effective diffusion coefficient, z_i is the charge of the ion, V is the local electric potential and r_i is the reaction rate. In the anode steady state model, the mass

transport was the study subject and the chemical substrate concentration was different in different location (through the anodic boundary diffusion layer, anodic biofilm, carbon paper) in the MFC system. The effective diffusion in the porous media depends on the porosity [52].

$$D_i^{eff} = \theta D_i \tag{3.16}$$

where D_i is the diffusion coefficient. Eqn. (3.18) [31, 53] for the anode biofilm porosity θ can be written as:

$$\theta = 1 - \sum_{i=1}^{n} \frac{c_{B,i}}{\rho_{B,i}} \tag{3.17}$$

where $c_{B,i}$ is the concentration of the biomass species i in the biofilm (n = 1 since only ARB is considered) (g/m^3), $\rho_{B,i}$ is the individual microbial density (g/m^3).

Because the system is a batch reactor (without agitator in the one chamber MFC system), there is no real time substrate flow in or out of the reactor. Since this transient model focused on the overpotential changes and mass transport in the electrode instead of the bulk liquid part, the substances distribution in the bulk liquid part was ignored and the amount of the chemical substances was signified by the average concentration in the bulk liquid. The acetate concentration balance is:

$$\frac{dc_{Ac}}{dt} = r_{Ac,B} + \frac{1}{v_F} \int_{V_F} r_{Ac,F} dV \tag{3.18}$$

The oxidized mediator concentration:

$$\frac{dc_{Mox}}{dt} = r_{Mox,B} + \frac{1}{v_F} \int_{V_F} r_{Mox,F} dV + \frac{1}{A_s} \int_{V_F} r_{Mox,E} dA_s \tag{3.19}$$

The reduced mediator concentration:

$$\frac{dc_{Mred}}{dt} = r_{Mred,B} + \frac{1}{v_F}\int_{V_F} r_{Mred,F}dV + \frac{1}{A_S}\int_{A_S} r_{Mred,E}dA_S \quad (3.20)$$

The active biomass concentration:

$$\frac{dc_{B,B}}{dt} = r_{X,B} + r_{det}\frac{A_F}{v_B} \quad (3.21)$$

The inactive biomass concentration [54]:

$$\frac{dc_{D,B}}{dt} = r_{decay} = f_D b_{decay} c_{B,B}(t) \quad (3.22)$$

where r_B is the reaction in the bulk liquid, r_F is the reaction in the biofilm, r_E is the reaction on the electrode surface (g/(m^3·s)); $c_{B,B}$ is the ARB active biomass concentration in biofilm (g/m^3); $c_{D,B}$ is the ARB inactive biomass concentration in biofilm (g/m^3); r_{det} is the active biomass detachment rate (g/(m^2·s)); r_{decay} is the inactive biomass decay (g/(m^3·s)); f_D is biomass decay ratio (%); b_{decay} is biomass decay rate (g/(m^3·s)).

3.1.4 Biofilm growth

The *exoelectrogens* were directly inoculated from the wastewater in the experiments in this research, therefore the anode biofilm usually consisted of multiple cultures of microbes, probably acetoclastic and methanogenic microorganisms [55, 56]. To simplify the properties study of the anodic biofilm species, the model assumed that the electricigenic microbes (ARB) were the main species for current generation while the influence of other bacteria cultures was negligible (e.g., the CH_4 produced by methanogens is what by controlling the MFC environment). The biofilm thickness L_F (m) change was decided by the

thickness displaced velocity u_F (m/s) and biofilm detachment velocity u_{det} (m/s). The thickness displaced velocity was derived previously [53, 57]:

$$u_F(x) = \frac{1}{1-\theta}\int_0^{L_F}\sum_{i=1}^{n}\frac{r_{B,i}}{\rho_{B,i}}dx \tag{3.23}$$

where θ is the anode biofilm porosity which has been derived by the Eqn. (3.17), L_F is the biofilm thickness (m), $r_{B,i}$ is the reaction rate of biomass species i (g/(m^3·s)), $\rho_{B,i}$ is the individual microbial density of species i (g/m^3). The displacement velocity u_F of a cell at location position (m/s) is equal to the added net specific mass production of all microbial species of the biofilm matrix out to that location in the biofilm. The biomass concentration in the biofilm was described by

$$\frac{\partial c_{B,i}}{\partial t} = D_{B,i}\frac{\partial^2(c_{B,i})}{\partial x^2} + r_{B,i} \tag{3.24}$$

In addition, D_B is the biomass diffusion coefficient in the biofilm (g/(m^2·s)), the anode biofilm thickness L_F (m) was described by:

$$\frac{dL_F}{dt} = u_F|_{x=L_F} - u_{det} \tag{3.25}$$

where u_F is the biofilm thickness displacement velocity calculated in the Eqn. (3.23), and u_{det} is the global biofilm detachment velocity (m/s) which has been described by the Eqn. (3.12).

All the governing equations and parameters needed to build a complete MFC system model based on the mediator transport mechanisms have been presented in this section. With this model, the current density was obtained with

a function of time, the biofilm thickness growth rate, and the acetate and mediator consumption rates.

3.2 Anode Steady State Model Analysis

3.2.1 Anode steady state model algorithm

The one-dimensional cathodic steady state model was constructed by C++ programming in Linux system. The algorithm of the anode steady state model was constructed with these equations shown in above and Butler-Volmer equation [37]. The algorithm is shown in Figure 3.4.

The cathode potential was fixed so that the anode activation overpotential can be calculated based on the Eqn. (3.7) (first principle electrochemical relation), then the current density was derived from the Bulter-Volmer equation by the calculated overpotentials. According to the stoichiometric relations for the substance in the anodic model, the reaction rates were derived and the source term in the mass transport equation were known and applied for calculating the substance concentration distribution in the anode different layers. With the relations in the Eqn. (2.2) and the Eqn. (2.3), the amount of the electron collection on the anode surface was calculated and the current can be integrated. The updated current was compared with the current in last step time, and if the residual was smaller than the tolerance, the computational stopped or the updated current would be used for the calculation in next step time.

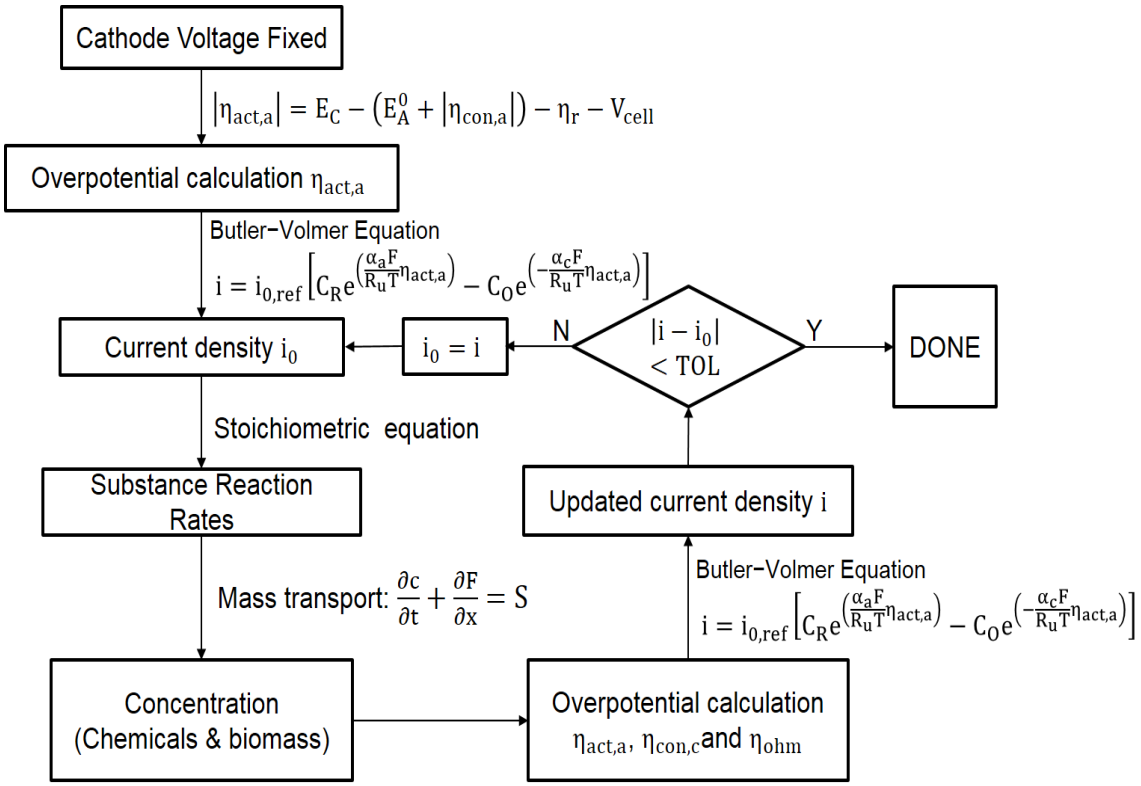

Figure 3.4 Computational algorithm for anode steady state model.

3.2.2 Comparison of the ions diffusion and electric migration in anode steady state model

Based on the anode steady state model, the influence of the electric migration in the MFC system was evaluated. The ions transport only considered the diffusion and electric migration in the anode steady state model. The mechanism for electron transport in this simulation utilized electron mediators, which is a common method in MFC anode modeling [27, 44]. As shown in Eqn. (2.2) and Eqn. (2.3), the electron mediator concentrations M_{ox} and M_{red} on the anode surface depend only on current density. Eqn. (3.8) and Eqn. (3.10) describe the changes in acetate concentration due to biofilm biomass consumption. The polarization and power density curves were presented by Figure 3.5 to compare the influence from electric field in mass transport to the MFC performance. The simulation results of mass transport (including both diffusion and electric field) has good fitting with the experimental profile, the polarization curve average deviation is less than 2.20 %. Also the simulation results of mass transport (diffusion only) produced very close power density and polarization curves based on the anode model, which average difference is only 1.92 %. Therefore the electric field has very small influence to increase the power generation and MFC performance from the anodic based MFC model. Some previous anodic modeling research neglected the electric field in the mass transport [27, 58].

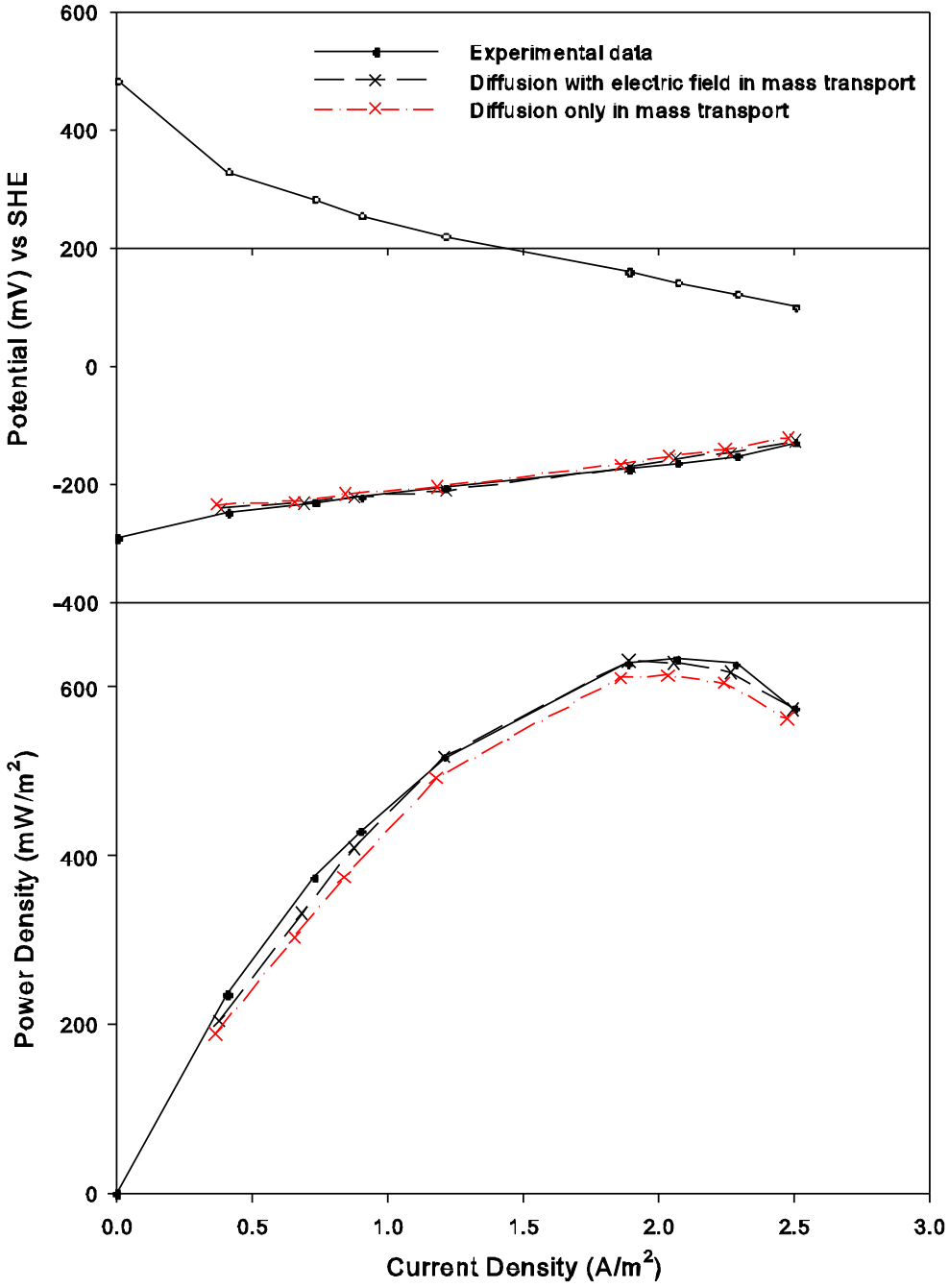

Figure 3.5 The comparison of polarization and power density curves for diffusion and electric field in mass transport.

3.3 Anode Transient Model Analysis

3.3.1 Anode transient model algorithm

The anode transient model was built by MATLAB code. The algorithm is presented by the Figure 3.6. The computational algorithm is similar to the algorithm for the steady state model, but the suspended biomass as well as the ARB in biofilm consumption with the acetate were both considered. When the new current density i^n was obtained, this new current density i^n would be the current density for calculating the electrochemical parameters (ohmic overpotential η_r and activation overpotential $\eta_{act,a}$) in next step time till the time ends. The model simulated 14 days anodic biomass and biofilm growth, the acetate and electron mediators (M_{OX} and M_{red}) were changed based on the reactions and consumption by the ARB and suspended biomass.

3.3.2 Prediction of the anode biofilm growth and dissolved species transport

This transient model predicted the anode biofilm growth and dissolved substance reactions and consumptions. In order to establish a common basis for electron transport with the work reported by Picioreanu [27], the mechanism for electron transport in this simulation utilized electron mediators. As shown in the Eqn. (2.3), the mediators M_{OX} and M_{red} depend only on current density. The Eqn. (3.8) and Eqn. (3.10) show that changes in acetate concentration occur mainly due to biofilm biomass consumption (Figure 3.7 a)). In the Figure 3.7 b) and the

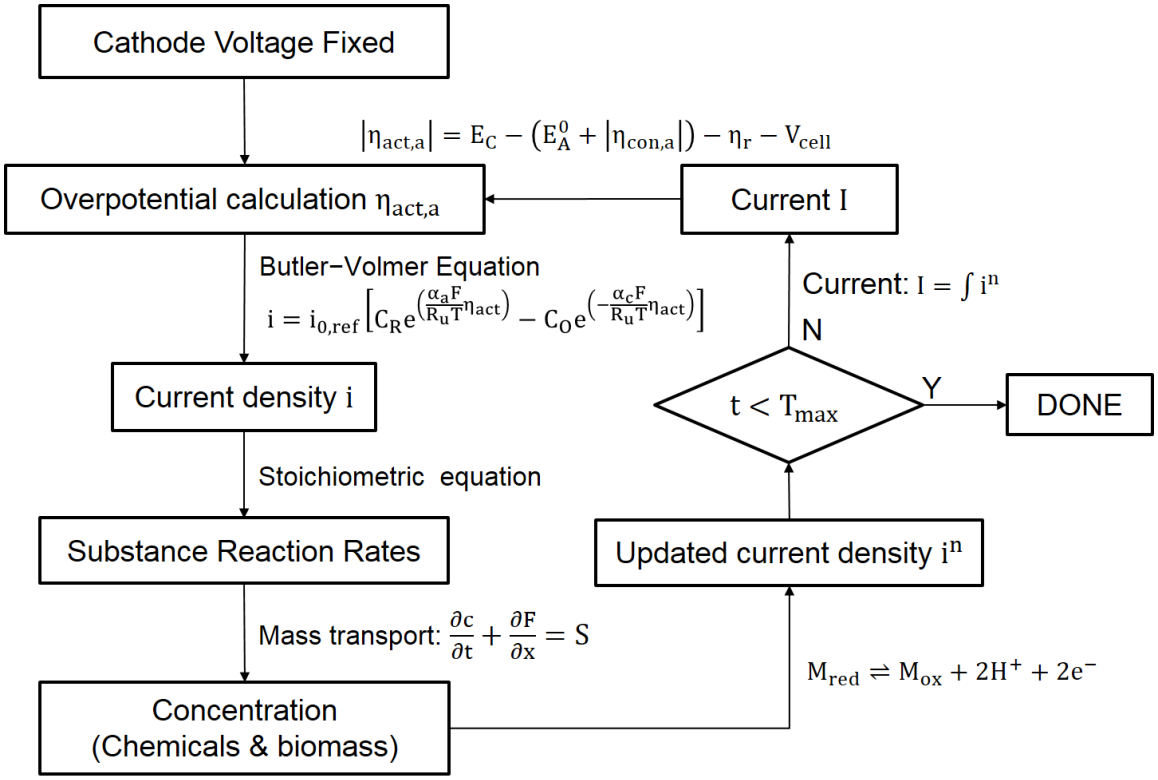

Figure 3.6 Computational algorithm for anode transient model.

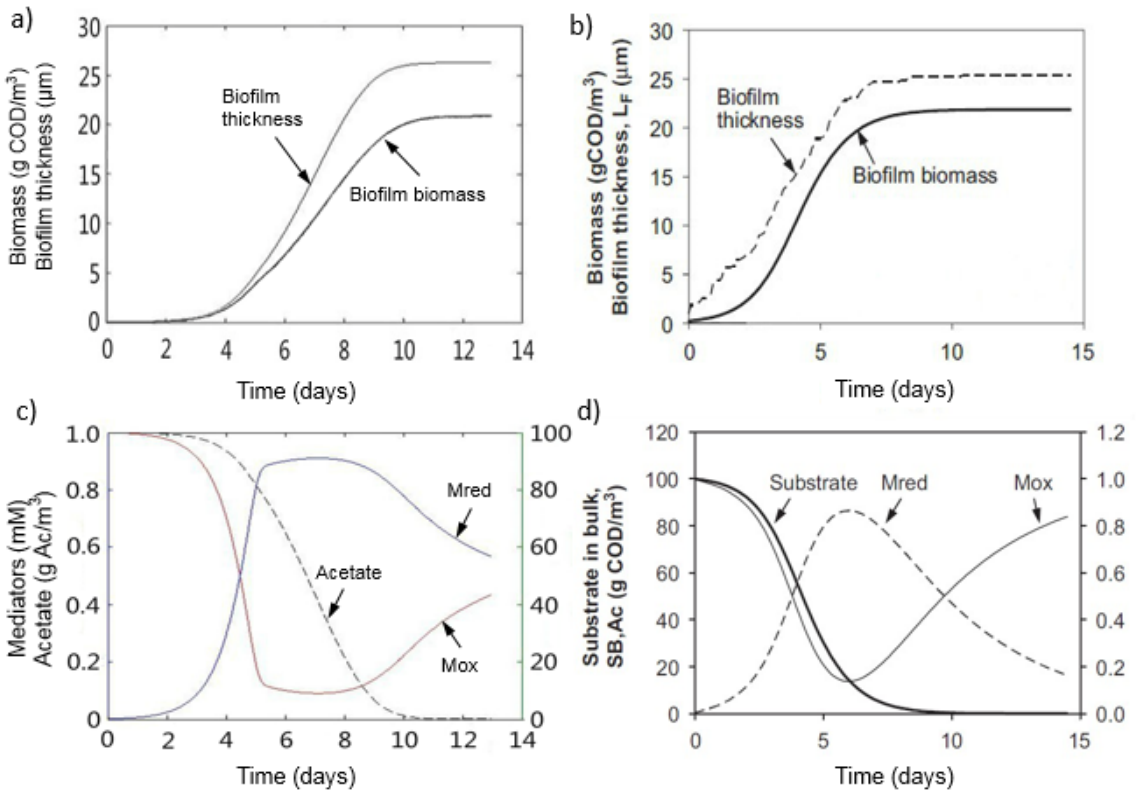

Figure 3.7 Comparison of this work with established anode biofilm model: a) and b) simulation of anode biofilm biomass and thickness, and substrate concentration over time; c) and d) Simulation of biofilm biomass and thickness, and substrate concentration over time from the reference [27].

Figure 3.7 d), the mediators tend to revert to their original concentrations coincidentally with the depletion of acetate, thus stopping the flow of current. The plateau for biomass concentration in the biofilm and biofilm thickness can be inferred from Eqns. (3.22), (3.23) and (3.25), evident in Figure 3.7 a). In addition, the thickness of biofilm also increases the diffusion resistance of the acetate substrate in biofilm. After approximately four days' growth, the biofilm biomass growth accelerates, resulting in a commensurate acceleration of biofilm thickness increase, as shown in Eqn. (3.23). The steady state biofilm thickness and biomass observed in Figure 3.6 a) are predicted by Eqn. (3.25). While this work used a different method and values for parameters compared to Picioreanu et al. [27], it is apparent that similar trends developed for Figure 3.7 a) and b) (our work) vs. Figure 3.7 c) and d). As the method utilized to develop the anode model was intended to be adapted for a cathode-only analysis and, ultimately, a whole cell model, such agreement is considered promising.

3.4 Conclusion

In the anode model work, a systematic series of equations to describe the physical, chemical, biological, and electrochemical phenomena in an air cathode MFC system was established. A steady state anode model was utilized to describe the diffusion and electric field in the ions transport. The electric field has a minor impact to the MFC performance based on the anodic model, therefore the electric field can be neglected in the mass transport analysis. A transient anode model was also utilized to describe the growth and establishment of the

biofilm while also tracking mediator concentrations over time. The anode model and its method will be adapted for the anode part in the full cell model in Chapter V.

CHAPTER IV

CATHODIC HALF-CELL STEADY STATE MODEL IN MFC

Many MFC models neglected the influence of biomass growth and the air cathode on the whole system. Biomass growth and the air cathode have been found to affect the full cell performance, shown experimentally [23]. In the single chamber air-cathode MFC reactor, the cathode usually supplies the aerobic bacteria a better living environment that the oxygen is transported through the cathodic materials into reactor. The cathodic oxygen-enriched environment benefits the growth of the aerobic bacteria which tend to be more competitive and adaptable for the nutrients from the bulk liquid than the ARB on the anodic side in the reactor. Additionally, the oxygen (O_2) and hydroxide (OH^-) mass transfer have been approved that impact the electricity generation and power output in the MFC [22]. Although these phenomena have already been discovered experimentally in labs, few models and hypotheses systematically were applied to analyze the cathode experimental data and to give methods to remedy the cathode design for the energy efficiency improvement of the whole system. In order to better understand the internal relations between the mass transfer and electrochemical reactions in the cathode, it is meaningful to build the cathode steady state model for the single chamber air-cathode MFC reactor. It was assumed that the potential losses were governed by the transport of hydroxide from the Pt/C catalyst layer to the bulk liquid instead of the availability of protons [23]. The chemical substance transport in the cathodic materials and

bulk liquid in different current density was presented and the cathodic catalyst was compared in the cathodic steady state model in this chapter.

4.1 Cathode Structure and Materials

The properties of cathodic materials have significant effects on the power generation; the experimental data from the previous research have shown that the power generation would be different with diverse cathode structures and components [24]. Thus it is important to understand the structure and properties of the materials in the cathode before modeling. With the research group member's help, the images for the cathodic materials by scanning electron microscope (SEM) was presented (shown in Figure 4.1) and the cathode structures were calibrated (shown in Table 4.1). In the Figure 4.1 a), from the left to right are: PTFE layer (dense channels and interlocking mesh of structure which is helpful for water-proof), carbon cloth (irregular sparse and reticulate carbon structure which results large porosity and is easy for substance diffusion), and Pt/C catalyst layer (the structure is consist of chunks which are the Pt/C catalyst, and the tortuosity and porosity in channels through the chunks are both much higher in the Pt/C catalyst layer).

Based on the analysis for the cathode materials, the cathodic modeling domains were divided into 6 layers. Figure 4.2 presents the schematic of the cathode structure (from air side to liquid side): the PTFE layer, the carbon cloth, the Pt/C catalyst layer, the cathodic biofilm. The reactor liquid part was divided

Table 4.1. Thickness of each layer at cathode cross section (Personal communicate with Hiroyuki Kashima).

	Averaged thickness (μm)	S.D.(μm)
PTFE diffusion layer	22.82	2.56
Carbon cloth	173.21	12.50
Pt/C Catalyst layer	32.50	5.68

a)

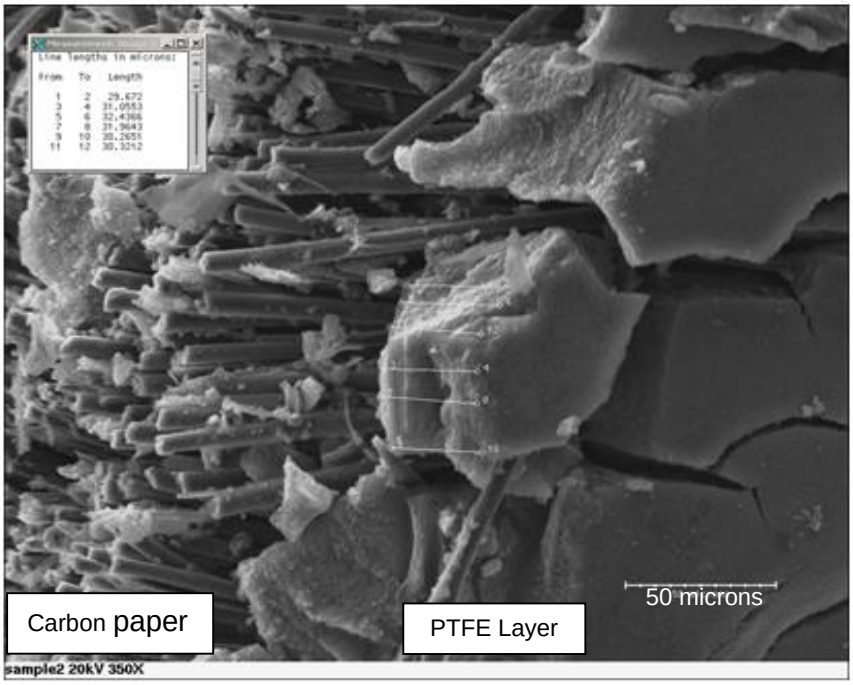

b)

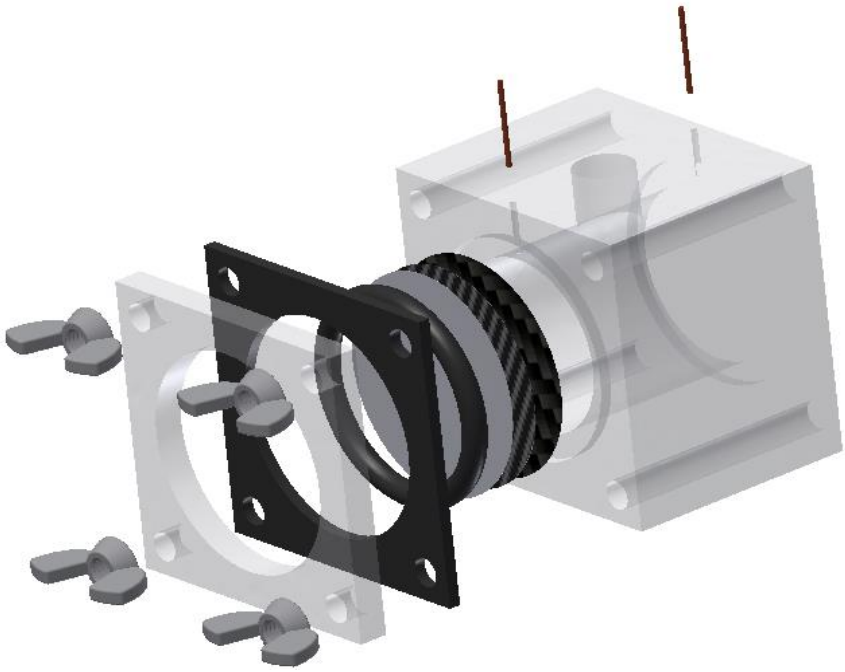

Figure 4.1 a) Scanning electron microscope (SEM) picture for MFC cathodic materials; b) 3D schematic for the cathodic structure in MFC.

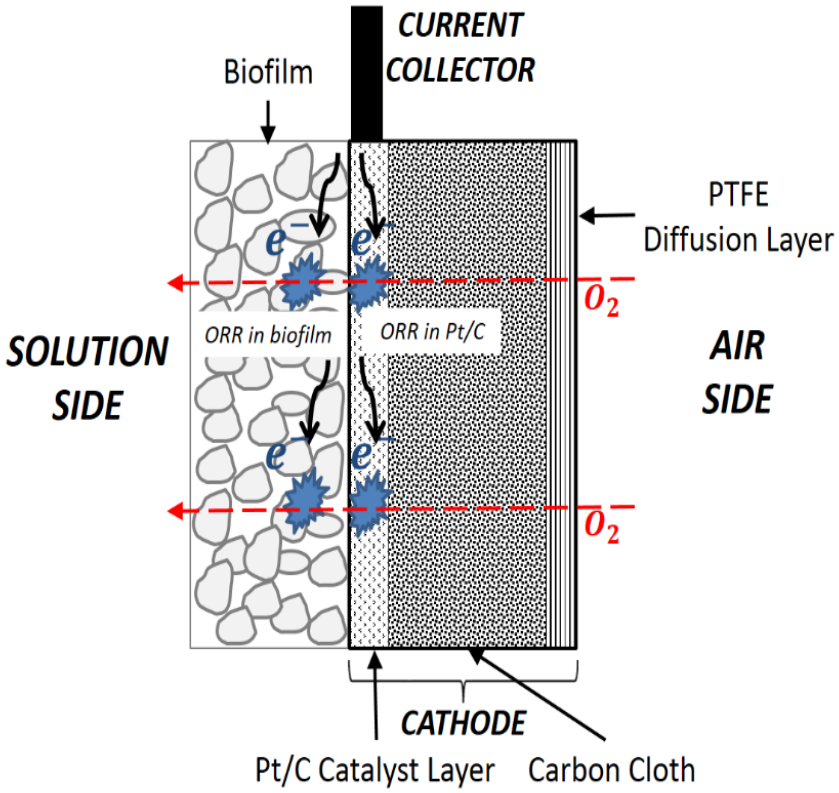

Figure 4.2 Schematic of the MFC air-cathode.

into the diffusion boundary layer (this domain is still part of the bulk liquid, and it is a thin layer which is a transition for the mass transport between cathodic biofilm domain and bulk liquid domain.) and bulk liquid domain (the nutriment source). The carbon cloth and Pt/C catalyst layers are both saturated with the liquid, and the Pt/C catalyst is the primary place where the ORR takes place, while the PTFE layer is water-proof and electrically insulating. Meanwhile, the biomass also attach to the cathode materials to form a biofilm which competes with the ARB in the anodic biofilm for the acetate and consume the oxygen transported through the cathode. On the one hand, the cathodic biofilm competes and consumes the nutrients in the bulk liquid, which negatively affects the MFC performance; on the other hand, it consumes the oxygen and create an oxygen-free environment for the anodic biofilm, which is positive influence.

4.2 Methods for Cathodic Steady State Model

The steady state model focused on the mass transport and ORR reactions in the different material layers. In an effort to focus on changes in the cathode, this simulation operated on the assumption that the bulk liquid acetate (c_{Ac} = 800 mg/L) and pH (pH = 7.08) kept unchanged. The bulk liquid, commonly, contains the buffer liquid to maintain the bulk liquid pH balance, supporting the pH assumption. In addition to an unchanging liquid pH environment, the cathode biofilm was assumed to be fully grown, meaning that the biofilm thickness and biomass concentration were constant. Additionally, the biofilm detachment rate and attachment rate were balanced. In the cathode steady state model, a fully

matured cathode biofilm was considered because cathode biofilms are much thicker than anode biofilms and it has obvious effects to the system performance [59], the thickness and biomass density only change in a small range which was assumed to be stable in this mathematical simulation [60], this assumption was also validated in the transient model in the Chapter V. The cathode biofilm thickness can differ considerably among different experiments [61], and it was assumed that a steady-state biofilm thickness of 1 mm in the one chamber MFC reactor [23].

The polarization/power density experiment was implemented when the biofilm had been fully grown and changed to different external resistance to measure the current density, overpotentials. Because polarization curves with an experimental MFC were conducted with external resistors, the model used the external resistance as the control variable in different simulations. The PTFE layer is relatively dense and hydrophobic, which does not allow significant liquid water accumulation under normal operating conditions. The oxygen diffuses in PTFE in the gas phase and then dissolves in the liquid on the boundary between PTFE and carbon cloth according to Henry's law. In the experimental work, a difference in MFC performance was observed when helium-oxygen and nitrogen-oxygen (heliox and nitrox, respectively) gas mixtures were used at the cathode instead of air [39]. To achieve this difference, this model uses the assumption that gas is partially present in the carbon cloth and catalyst layers.

This model also assumed that the cathode biofilm was composed of two broad populations: autotrophic aerobic bacteria (AAB) and heterotrophic aerobic bacteria (HAB). The AAB are biological catalysts for the ORR at the cathode, acting as electron acceptors for the external circuit. The HAB do not depend on the circuit for electrons, but they are able to influence the mass transport of the substances and hydroxide distribution in the cathode. For simplification, all the anode electrical potentials were known constants in every external resistance situations, so that the anode electrochemical changes were reasonably neglected in the modeling calculation.

The ORR occurs in the metal catalyst and biofilm layers in the cathode model. Local reaction stoichiometry is affected by the electron distribution. Electrons from the cathode current collector follow two paths (Figure 4.3): most electrons are consumed by the platinized Pt/C catalyst layer, while the remaining electrons are used to support the synthesis of the AAB in the cathode biofilm. The cathodic biofilm has the same capability as the Pt/C catalyst layer (metal catalyst) for the electrons consumption, the cathodic biofilm was named as biocatalyst in the MFC cathode [62].

4.2.1 Mass transport in PTFE diffusion layer

When the air transports across a phase boundary (e.g., gas into a solid), the concentration discontinuity across the phase boundary between a solid and gas can be typically modeled with Henry's law:

$$c^{0}_{O_2,P}\left(\frac{mol}{L}\right) = \frac{y_{O_2,gas\ side} P_{gas\ side}}{H(T)} \cdot \frac{1000cm^3}{L} \quad (4.1)$$

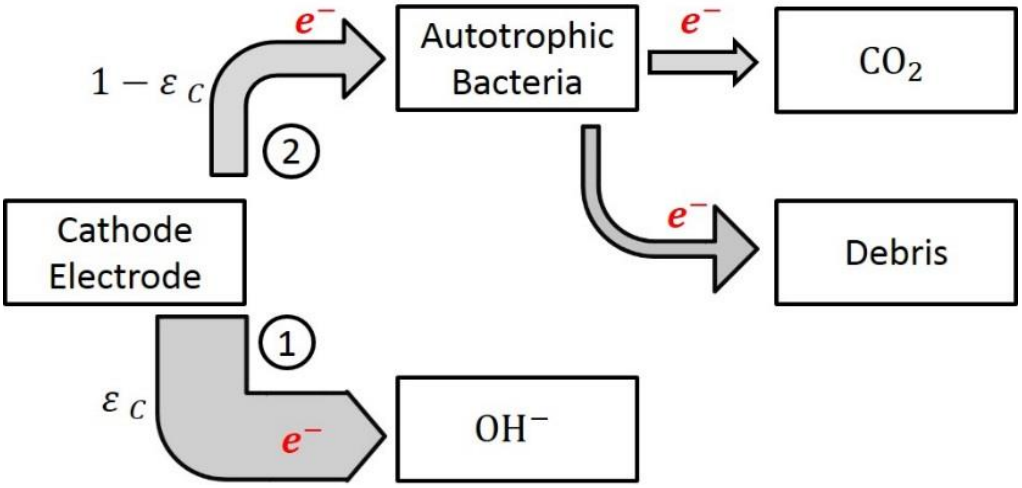

ε_C: Fraction of electrons used for oxygen reduction on the cathode;
Path 1: Electrons transferred from cathode to platinized ORR.
Path 2: The electrons used to support autotrophic growth.

Figure 4.3 Electron transfer paths on cathode.

where $y_{O2,gas\ side}$ is the oxygen mole fraction in the gas (dimensionless), the volume fraction: 21 % oxygen and 79 % nitrogen; $P_{gas\ side}$ is the gas pressure (atm). The oxygen henry constant $H_{O2\text{-}Nafion}$ in the PTFE layer can be calculated by the Eqn. (4.2).

$$\mathrm{H_{o_2-Nafion}}\left(\frac{\mathrm{atm\cdot cm^3}}{\mathrm{mol}}\right) = \exp\left(\frac{-666.0}{\mathrm{T}} + 14.1\right) \tag{4.2}$$

The oxygen transport in the cathode is obstructed by a thin layer of liquid and ionomer at the catalyst surface, resulting in additional film resistance [37], it was assumed in the simulation that the gas is dissolved in the bulk liquid at the boundary between the PTFE and the carbon cloth. In the experiment, it was compared for the current generation of two air-cathode MFC reactors with two gas sources: O_2/N_2 and O_2/He separately. The results showed that the power produced by the reactor with O_2/He is higher than the power from the reactor with O_2/N_2. It has been known that the oxygen diffusion coefficient in helium is higher than the oxygen diffusion coefficient in the nitrogen. The Maxwell-Stefan diffusivities in gas can be described with an empirical equation [63] based on the kinetic gas theory:

$$\mathrm{D_{ij}} = \mathrm{k_{ij}}\frac{\mathrm{T^{1.75}}}{\mathrm{P\left(v_i^{1/3}+v_j^{1/3}\right)^2}}\left[\frac{1}{\mathrm{M_i}}+\frac{1}{\mathrm{M_j}}\right]^{1/2} \tag{4.3}$$

where D_{ij} is the gas diffusion coefficient in the mixture gas (m^2/s), k_{ij} is a constant with the value 3.16×10^{-8} ($Pa\cdot m^2/s$), T is the temperature (K), P denotes the pressure (Pa), v_i equals the molar diffusion volume of species i (m^3/mol), M_i is the molar mass of species i (kg/mol), the molar diffusion volume of oxygen v_{O2} is

16.6×10^{-8} (m^3/mol), and the molar diffusion volume of nitrogen v_{N2} is 17.9×10^{-6} (m^3/mol) [64]. The calculation for oxygen diffusion coefficient in PTFE Diffusion Layer is expressed by the Eqn. (4.4).

$$D_{o_2,PTFE} = D_{o_2,air}\phi_P^{1.5} \tag{4.4}$$

where $D_{O2,PTFE}$ is the oxygen diffusion coefficient in PTFE layer (m^2/s), $D_{O2,air}$ is the oxygen diffusion coefficient in air (m^2/s), and Φ_P is the porosity volume fraction in the PTFE diffusion layer (dimensionless).

Then, the oxygen flux can be calculated from the following equation,

$$F_{o_2,gas} = \frac{P_{gas}}{RT}\frac{\phi}{\tau}\left(\frac{y_{O_2}}{y_{N_2}}D_{N_2,gas} + D_{o_2,gas}\right)\frac{dy_{O_2}}{dx} \tag{4.5}$$

where $F_{O2,\ gas}$ is the oxygen flux in the mixture gas (mol/m^2·s), P_{gas} is the gas pressure in the mixture gas (Pa), τ is the tortuosity if the gas is diffused in the channels (dimensionless), y_{O2} is the mole fraction oxygen in the mixture gas (dimensionless), and y_{N2} is the mole fraction nitrogen in the mixture gas (dimensionless), and $D_{N2,PTFE}$ is the nitrogen diffusion coefficient in the mixture gas (m^2/s).

During oxygen is diffused through the PTFE Diffusion Layer, the oxygen flux can be derived by Eqn. (4.6):

$$F_{o_2,PTFE} = D_{o_2,PTFE}\frac{c_{o_2,PTFE}^{L_P} - c_{o_2,PTFE}^{0}}{L_P} \tag{4.6}$$

where $F_{O2,\ PTFE}$ is the oxygen flux in the PTFE layer (mol/m^2·s), $c_{O2,PTFE}^{Lp}$ is the oxygen concentration at PTFE layer boundary by the carbon cloth, and $c_{O2,PTFE}^{0}$ is the oxygen concentration at PTFE layer boundary by the air side, and L_P is

length of the PTFE layer. The calculation for the oxygen concentration at the PTFE layer boundary by the carbon cloth side is shown by the Eqn. (4.7).

$$c_{O_2,PTFE}^{L_P} = \frac{F_{O_2,PTFE} L_P}{D_{O_2,PTFE}} + c_{O_2,PTFE}^{0} \quad (4.7)$$

4.2.2 Mass transport in the carbon cloth

The carbon cloth is the dominant part in the MFC cathode. Since the porosity is enough large, It has shown that the microbes can go through into this layer and exist here from the experiments [65]. In the cathodic steady state model, only the PTFE layer was assumed to have solid and gas phase, while the carbon cloth and catalyst layer were assumed with both solid and liquid phase. Specifically, in the simulation for the N_2/O_2 and He/O_2 comparison, it was assumed that the carbon cloth had all three phases: solid, liquid and gas. Both liquid and gas phases were in the pores in the carbon cloth.

It was known that the MFCs produced consistent and reproducible currents under the 1000 ohm acclimation conditions (Figure 4.4), with a good agreement between duplicate reactors. The peak current densities of MFCs separated after they were changed to different gas conditions, with heliox-fed cathodes producing the highest current densities and air-fed cathodes producing the lowest.

The polarization tests were performed after the duplicated MFCs had identical and consistent voltages under different gas conditions. The maximum power density produced by the heliox MFC was 1320 ± 50 mW/m^2 at 75 Ω

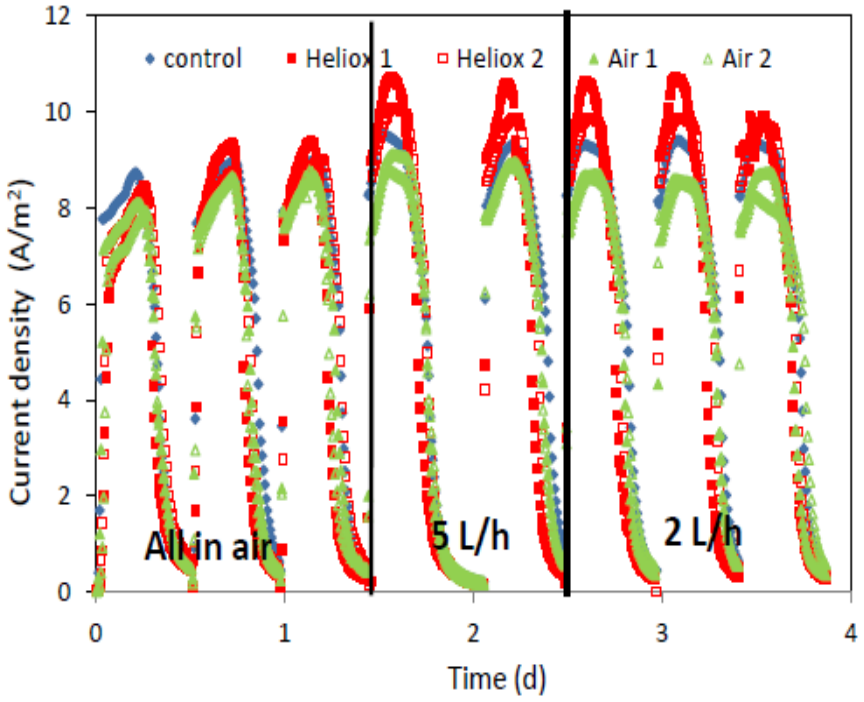

Figure 4.4 Current generated by MFCs under different air and heliox flow rate [39].

external resistance, while the nitrox-fed MFC reached a maximum power of 1280 ± 50 mW/m^2, and the air-fed MFC showed the lowest maximum power at 1050 ± 40 mW/m^2. In Figure 4.5, experiment results showed that the oxygen diffusion coefficient in the cathode affects the oxygen concentration in the cathode side which results in different electricity generation and power output of MFC [39]. The MFC cathodic steady state model was able to give the hypothesis and explain this phenomenon which has been shown in the thesis [39].

Additionally, the gas-liquid mass transfer mechanics in the cathode of MFCs was also adopted in this cathodic steady state model. The gas-liquid mass transfer is modeled by the two-film theory [66], as Figure 4.6 shows. The flux F_{O2} through two films (gas film and liquid film) is described as the oxygen concentration difference across the film layer. The flux across the gas film is given by the Eqn. (4.8)

$$F_{o_2,g} = k_g\left(P_{o_2} - P_{o_2,b}\right) = -D_{o_2}\frac{c_{o_2} - c_{o_2,b}}{\delta} \tag{4.8}$$

where P_{O2} is the partial pressure of oxygen in the mixed gas (Pa), and $P_{O2,\,b}$ is the corresponding partial pressure in the gas (Pa) (on the film boundary) that corresponds to the equilibrium concentration $c_{O2,b}$ (on the film boundary) (mol/m^3), k_g is the gas phase mass transfer coefficient (mol/N·s).

The flux across the liquid film is calculated by the Eqn. (4.9) [67],

$$F_{o_2,l} = k_l\left(c_{o_2} - c_{o_2,b}\right) \tag{4.9}$$

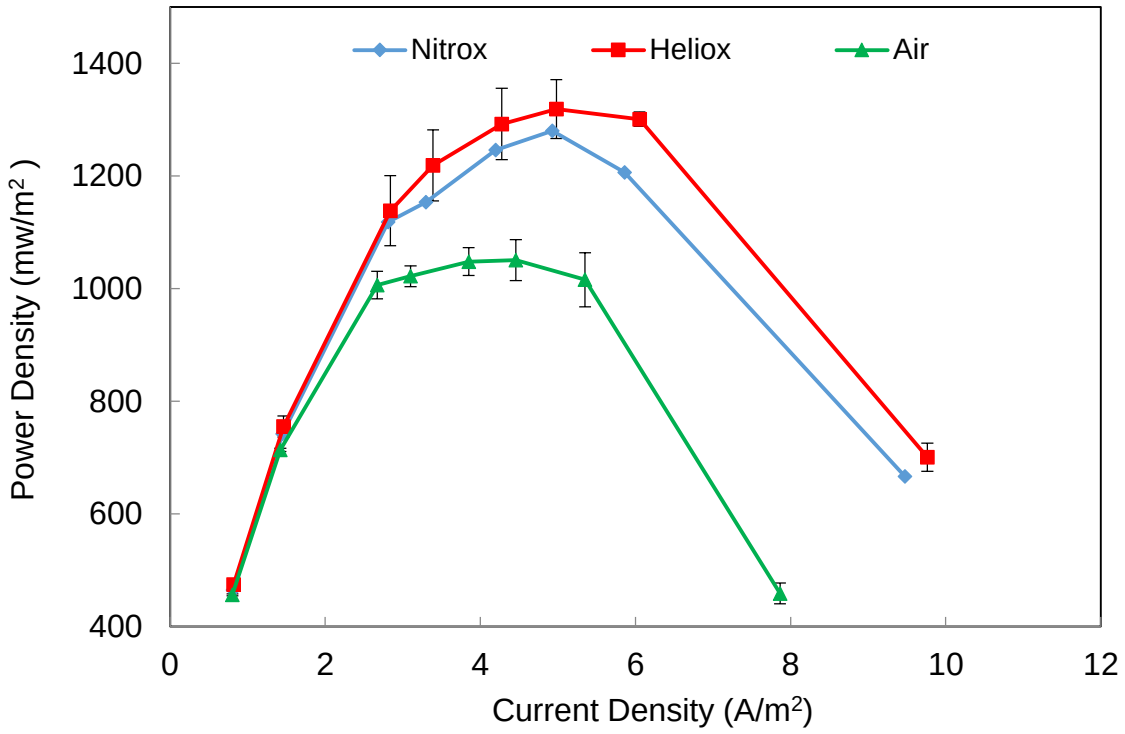

Figure 4.5 Power density curves [39].

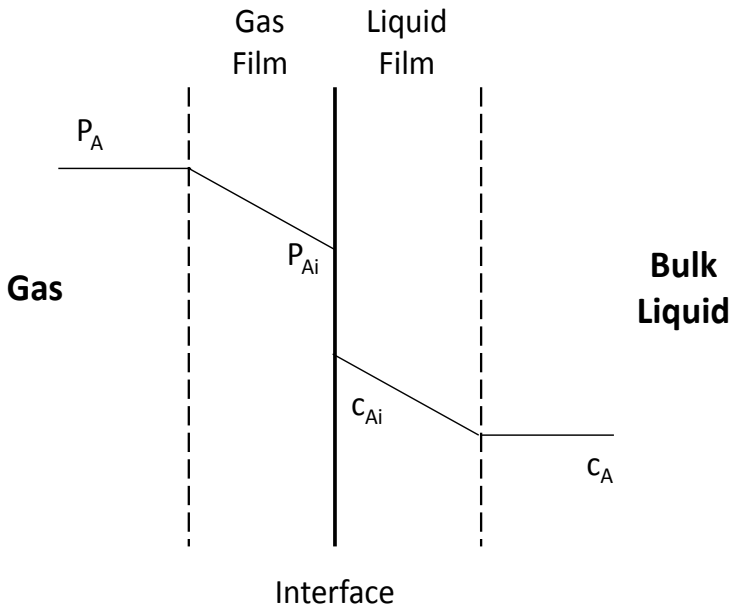

Figure 4.6 Gas-liquid mass transfer.

where $F_{O2,l}$ is the oxygen flux in liquid part (mol/m^2·s), k_l is the liquid phase mass transfer coefficient (m/s). The equilibrium concentrations on each side of the gas-liquid interface can be related to each other by Henry's law [68]:

$$P_{o_2,b} = H_{o_2} c_{o_2,b} \tag{4.10}$$

where H_{O2} is the Henry law's constant, the research adopted 769.23 (L·atm/mol) and 3.181×10^{-2} (dimensionless) as the values for the oxygen Henry law's constant [69].

4.2.3 Energy balance in cathode biofilm

The aerobic bacteria grow and attach to the cathodic plate surface because the oxygen supplied from the air side and the acetate or CO_2 from the bulk liquid that guarantee an appropriate environment for aerobic bacteria growth. In the cathodic biofilm, it consists of different species of microbes. In the cathodic model, two groups are considered based on the electron sources: one is the heterotrophic aerobic bacteria (HAB) which depend on acetate and oxygen, the electron source comes from the acetate in the bulk liquid; the other one is the autotrophic aerobic bacteria (AAB) which depend on CO_2 and O_2, the electrons source comes from the electrons from the cathodic electrode.

a.) Autotrophic Aerobic Bacteria

For the AAB, which depends on CO_2 and O_2 concentrations, the cathode was considered to be the electron donor, thus no donor reaction is specified. The

electron acceptor reaction (R_a) and cell synthesis reaction (R_c) are shown in Eqn. (4.11) and Eqn. (4.12).

$$R_a: \frac{1}{4}O_2 + \frac{1}{2}H_2O + e^- \rightarrow OH^- \qquad \Delta G^{0'} = -78.72\ \mathrm{kJ/e^-\ eq} \tag{4.11}$$

$$R_c: \frac{1}{5}CO_2 + \frac{1}{20}HCO_3^- + \frac{1}{20}NH_4^+ + \frac{11}{20}H_2O + e^- \rightarrow \frac{1}{20}C_5H_7O_2N + OH^- \tag{4.12}$$

where the catabolic reaction $\Delta G_r^{0'}$ is the difference between the electron donor and the electron acceptor and is assumed to be $\Delta G_r^{0'}$ = -78.32 kJ/e$^-$ eq, while the carbon source (cathode) conversion to pyruvate is $\Delta G_p^{0'}$ = 35.09 kJ/e$^-$ eq, and conversion of pyruvate into biomass ($C_5H_7O_2N$) is $\Delta G_{pc}^{0'}$ = 18.81 kJ/e$^-$ eq. An electron and energy balance between anabolism and catabolism of AAB is shown in Eqn. (4.13) [26]:

$$\frac{f_e^0}{f_s^0} = \frac{-\left(\frac{\Delta G_p^{0'}}{\sigma^n} + \frac{\Delta G_{pc}^{0'}}{\sigma}\right)}{\sigma \Delta G_r^{0'}} \tag{4.13}$$

where f_e^0 is the fraction of electrons directed by AAB from the cathode to O_2, f_s^0 is the fraction of electrons that go from the cathode to biomass ($f_e^0 + f_s^0 = 1$), σ is the efficiency of the energy transfer (typical value of 0.6 [26]), and n is an influence factor that equals to 1 if $\Delta G_p^{0'} > 0$, or equals to -1 if $\Delta G_p^{0'} < 0$ ($n = 1$ in this situation because is $\Delta G_p^{0'}$ = 35.09 kJ/e$^-$ eq). For this reaction, the fraction f_e^0/f_s^0 equals to 1.912, so f_e^0 = 0.657 and f_s^0 = 0.343. Based on the energy and electron transfer analysis of AAB growth on the cathode, the derived stoichiometric equation is shown below:

$$0.16425O_2 + 0.0686CO_2 + 0.01715NH_4^+ + 0.01715HCO_3^- + 0.51715H_2O + e^- \rightarrow 0.01715C_5H_7O_2N + OH^- \tag{4.14}$$

From Eqn. (4.14), AAB biomass yield $Y_{B,AAB}$ is 0.1044 (mol AAB)/(mol O_2), AAB hydroxide yield $Y_{OH,AAB}$ is 6.088 (mol OH^-)/(mol O_2), and the electron equivalence of oxygen $Y_{e^-,AAB}$ in AAB reaction is 6.088 (mol e^-)/(mol O_2). The reaction rate of biomass and hydroxide can then be calculated:

$$r_{B,AAB} = -Y_{B,AAB} r_{O2,AAB} \quad (4.15)$$

$$r_{OH,AAB} = -Y_{OH,AAB} r_{O2,AAB} \quad (4.16)$$

b.) Heterotrophic Aerobic Bacteria

When only acetate serves as the carbon source in the MFC reactor, the electron donor reaction (R_d), electron acceptor reaction (R_a), and the cell synthesis reaction (R_c) for HAB are shown in Eqn. (4.17), Eqn. (4.18) and Eqn. (4.19).

$$R_d: \frac{1}{8}CH_3COO^- + \frac{3}{8}H_2O \rightarrow \frac{1}{8}CO_2 + \frac{1}{8}HCO_3^- + H^+ + e^-;\ \Delta G^{0'} = -27.04\ kJ/e^-\ eq \quad (4.17)$$

$$R_a:\ \frac{1}{4}O_2 + \frac{1}{2}H_2O + e^- \rightarrow OH^+;\quad \Delta G^{0'} = -78.72\ kJ/e^-\ eq \quad (4.18)$$

$$R_c: \frac{1}{5}CO_2 + \frac{1}{20}HCO_3^- + \frac{1}{20}NH_4^+ + H^+ + e^- \rightarrow \frac{1}{20}C_5H_7O_2N + \frac{9}{20}H_2O \quad (4.19)$$

Based on Eqn. (4.18) and (4.19), the total energy transfer between acetate oxidation and oxygen reduction $\Delta G_r^{0'}$ = -105.36 kJ/e^- eq. Energy for acetate to pyruvate conversion ($\Delta G_p^{0'}$) should be the sum of the energy of reaction for the donor reaction ($\Delta G^{0'}$ = -27.04 kJ/e^- eq) in Eqn. (4.18) and the pyruvate production reaction (35.09 kJ/e^- eq), therefore $\Delta G_p^{0'}$ is 8.05 kJ/e^- eq. Finally, conversion of pyruvate into biomass ($C_5H_7O_2N$) $\Delta G_{pc}^{0'}$ is 18.81 kJ/e^- eq. Based on Eqn. (4.13), f_e^0 can be calculated to be 0.415 and f_s^0 can be calculated

to be 0.585, giving the following calculated stoichiometric relation for HAB growth on the cathode:

$$CH_3COO^- + 0.83O_2 + 0.234NH_4^+ + 0.064H_2O \rightarrow 0.234C_5H_7O_2N + 0.064CO_2 + 0.766HCO_3^- \quad (4.20)$$

By calculating the biochemical reaction for the cathode biofilm, the resultant HAB biomass yield $Y_{B,HAB}$ is 0.234 (mol HAB)/(mol Acetate), and HAB oxygen yield on acetate $Y_{O2,HAB}$ is 0.83 (mol O_2)/(mol Acetate). The reaction rate of biomass and oxygen can be calculated by Eqn. (4.21) and Eqn. (4.22).

$$r_{B,HAB} = -Y_{B,HAB} r_{Ac,HAB} \quad (4.21)$$

$$r_{O2,HAB} = Y_{O2,H} r_{Ac,HAB} \quad (4.22)$$

where $r_{XB,H}$ is the reaction rate of HAB biomass in cathode biofilm (g VSS)/m^3·s, and $r_{O2,H}$ is the reaction rate of HAB oxygen in cathode biofilm (mol O_2)/m^3·s.

The acetate and oxygen are both reactants to create new biomass in cathode biofilm. The mass balance can be written as:

$$\frac{\partial c_F}{\partial t} = \frac{\partial}{\partial x}\left(D\frac{\partial c_F}{\partial x}\right) + \frac{\partial}{\partial y}\left(D\frac{\partial c_F}{\partial y}\right) + \frac{\partial}{\partial z}\left(D\frac{\partial c_F}{\partial z}\right) + r_{S,F} \quad (4.23)$$

In order to better focus on the hydroxide and oxygen diffusion in the cathode, we only consider diffusion in the x-direction. One-dimensional partial differential equations are following equations:

$$\frac{\partial c_{Ac,F}}{\partial t} = D_{Ac,F}\frac{\partial^2 c_{Ac,F}}{\partial x^2} + r_{Ac,H} \quad (4.24)$$

$$\frac{\partial c_{O_2,F}}{\partial t} = D_{O_2,F}\frac{\partial^2 c_{O_2,F}}{\partial x^2} + r_{O_2,A} + r_{O_2,H} \quad (4.25)$$

$$\frac{\partial c_{OH,F}}{\partial t} = D_{OH,F}\frac{\partial^2 c_{OH,F}}{\partial x^2} + r_{OH,A} \quad (4.26)$$

4.3 Cathode Steady State Model Analysis

4.3.1 Cathode steady state model algorithm

The one-dimensional cathodic steady state model was constructed by the C++ programming in Linux system, the polarization and power density curves were compared with the experimental data. Also the two-dimensional steady state model was built by software COMSOL to analyze the ORR in the biocatalyst and metal catalyst. The algorithm is shown in Figure 4.7.

The anode potential was fixed to be know so that the cathode activation overpotential was calculated based on the first principle electrochemical relation, and the current density was derived from the Bulter-Volmer equation by the calculated overpotentials. According to the stoichiometric relations for the substance in the cathodic model, the reaction rates were derived and the source term in the mass transport equation was applied for calculating the substance concentration distribution in the cathode different domains. The updated current was compared with the current in the previous step time, the computational stopped if the residual was smaller than the tolerance, or the updated current would be used for the calculation loop in next step time.

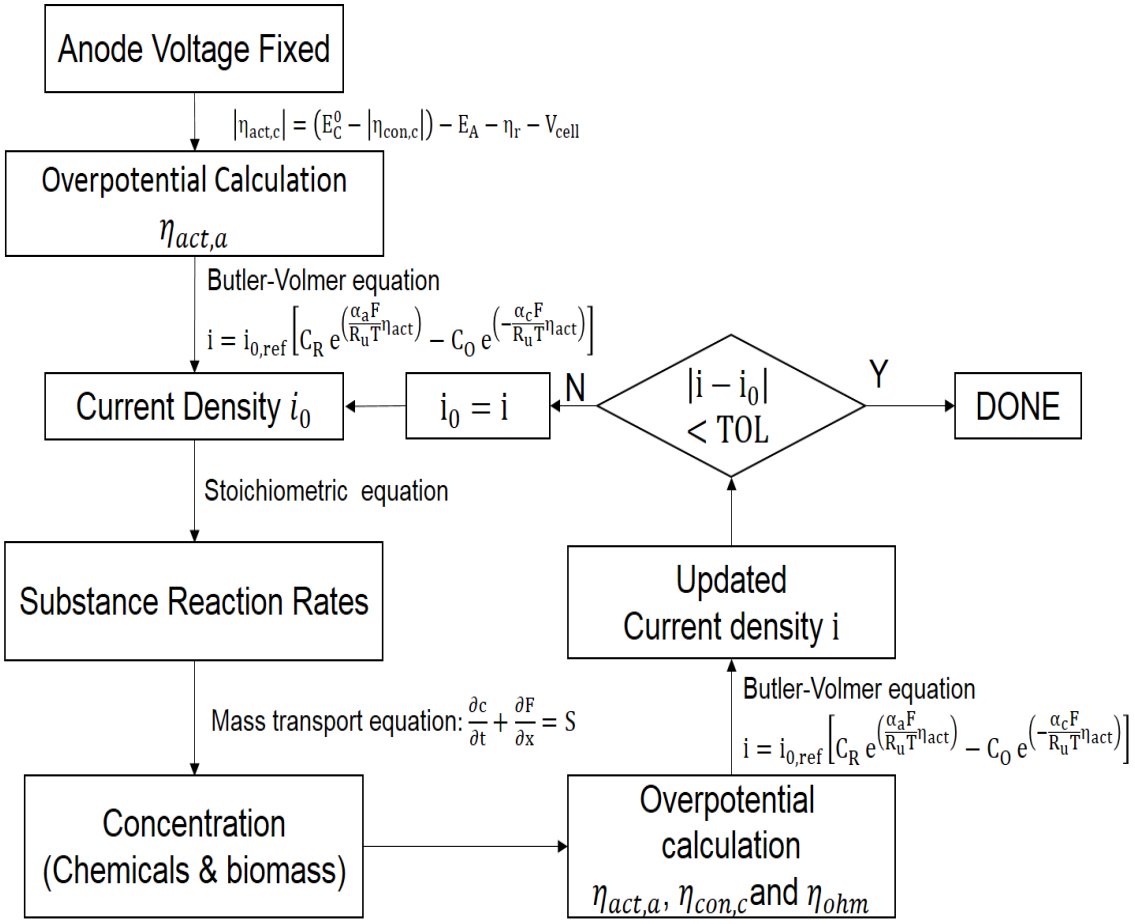

Figure 4.7 Polarization curve and power density results from the cathode model for carbon paper MFC system.

4.3.2 Power output prediction and cathodic limitations analysis for the MFC cathode system

Following completion of the anodic half-cell model, the cathode model that includes contributions from the metal catalyst and biological catalyst were constructed. Sources of cathode overpotential, including cathodic activation, ohmic resistance, mass transport losses, and substrate crossover, have recently been studied and found to have significant influence on system performance [25]. In this cathode model the anode potential was taken from experimental data (the red anodic potential line shown in Figure 4.8 a)), allowing the anode overpotential to be obtained at every external resistance, steady-state situation. It is apparent that the simulated cathode potentials are comparable to the experimental cathode potentials (Figure 4.8 a)) and that, in the operating cell, the cathode overpotential increases twice as much as anode overpotential with increasing current density. The largest deviation between polarization curves is 7.7 % (Figure 4.8 a)), and the largest deviation between power density curves is 8.8 % (Figure 4.8 b)).

The cathode model was formulated to delineate the various sources of overpotential associated with driving current. Specifically, concentration overpotential, activation overpotential, and ohmic overpotential were all separated; bulk liquid ohmic drop was also considered. The activation overpotential was the primary loss for a MFC system at low current density (Figure 4.9). The ohmic overpotential linearly grew as the current density

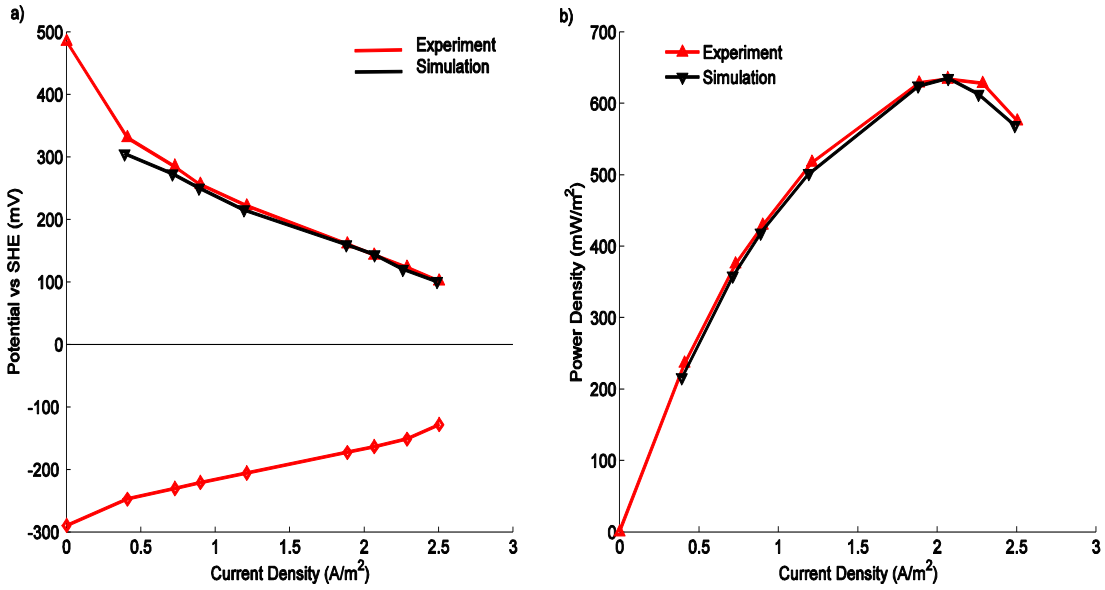

Figure 4.8 Polarization curve and power density results from the cathode model for carbon paper MFC system.

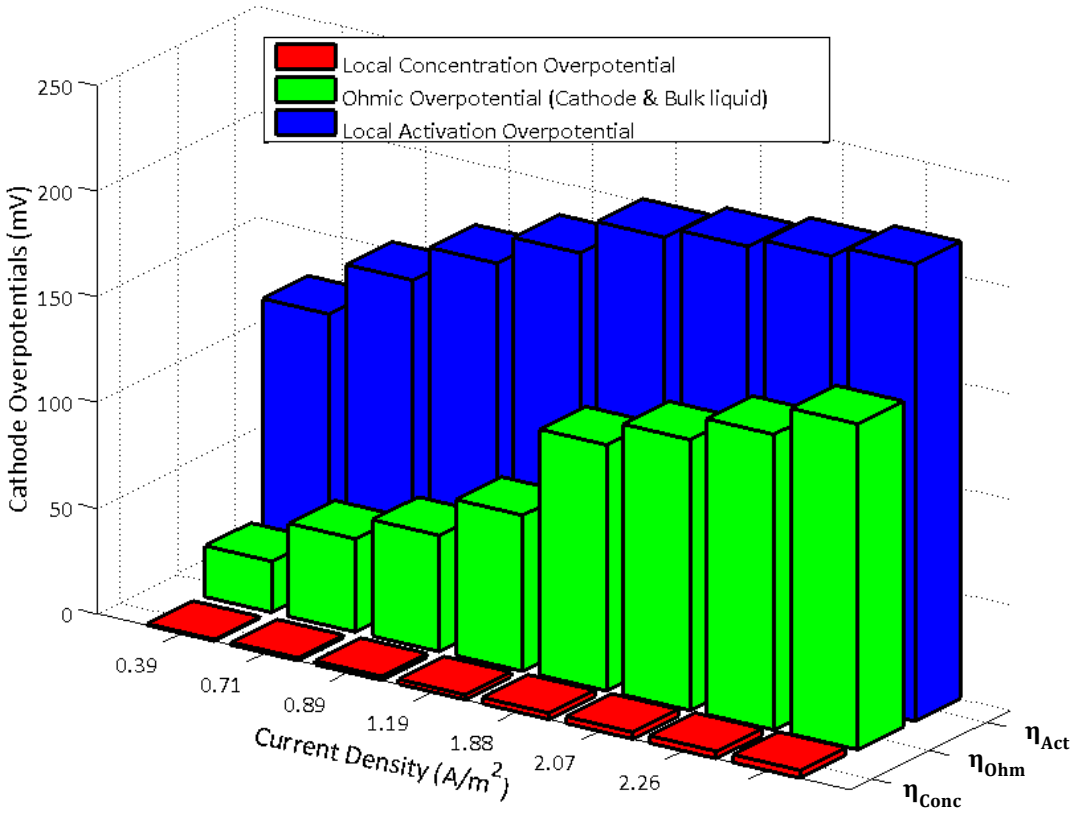

η_{Conc} *: Local concentration overpotential (mV);*
η_{Ohm} *: Ohmic overpotential in cathode and bulk liquid (mV);*
η_{Act} *: Local kinetic activation overpotential (mV).*

Figure 4.9 Comparison of the local activation overpotential and the ohmic overpotential.

increased, and both the ohmic overpotential and activation overpotential dominated voltage loss in the operating MFC. Concentration overpotential was a very minor component of the cathode total overpotential; this supports the assumption of neglecting mass transport limitations in some papers [10, 58]. In light of these findings, minimizing overpotentials in the cathode provides the most efficient path to improving MFC performance.

4.3.3 Comparison of the performance of metal catalyst and biocatalyst in cathode

Direct comparison of metal catalyst and biocatalyst performance in the cathode is rare in the literature [25]. This simulation included the contributions comparison from the Pt metal catalyst and biological catalyst. When the biocatalyst and the Pt catalyst are in the same system, others have found that the biocatalyst contribution to oxygen reduction is minor compared to that of the Pt metal catalyst [22]. Figure 4.10 shows modeling results of the polarization curve and power density for both biocatalyst-only cathode configuration and the biocatalyst with Pt metal catalyst cathode configuration. As expected, the biocatalyst-only cathode showed much poorer performance than the combined biocatalyst and metal catalyst. The highest power density for the biocatalyst-only simulation was 21 mW/m^2 while the highest power density for the biocatalyst with metal catalyst simulation was 239 mW/m^2. The biofilm only contributed 8.8 % of the total power in the combined catalyst simulation. Pt/C as the cathode material only produces 0.55 mW/$, thus this material greatly increases the cost of an

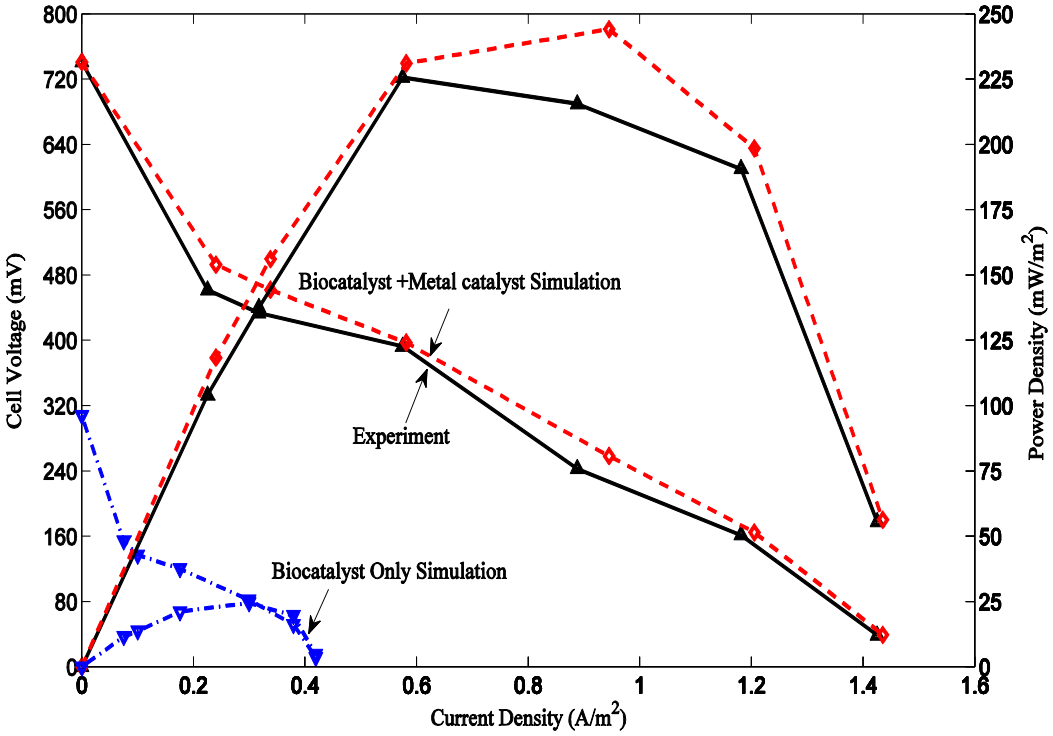

Figure 4.10 Polarization curves and power density simulation results for the biocatalyst cathode and metal catalyst cathode in carbon brush MFC system.

MFC system [70]. On the other hand, if the fraction of AAB in cathode biofilm could be increased, the AAB would improve the power output and potentially decrease the cost for cathode materials.

The physical modeling software COMSOL was adopted into the analysis to aid in better describing the catalyst performance. In Figure 4.11, pH is used as an indicator of cathode activity; pH would be much higher in a situation where the ORR happens more rapidly. Figure 4.11 a) and Figure 4.11 b) show the COMSOL model results comparing the pH distribution of Pt/C catalyst and the biofilm cathode (model parameters and variables are shown in the Appendix). Figure 4.11 a) and Figure 4.11 b) are both 1mm × 1mm sectional views of the cathode. In the simulation these two MFC systems were assumed to have the exact same reactor structure and same operating conditions so that any difference resulted only from the catalyst. It is apparent that the pH in the Pt/C catalyzed cathode is much higher than in the AAB biocatalyst cathode; this indicates that the metal catalyst is a much more effective catalyst since the ORR product is hydroxide. Because this research only focused on the cathode, the bulk liquid pH was maintained at 7.08 during simulation, instigating the rapid drop in pH at the far left of each plot in Figure 4.11.

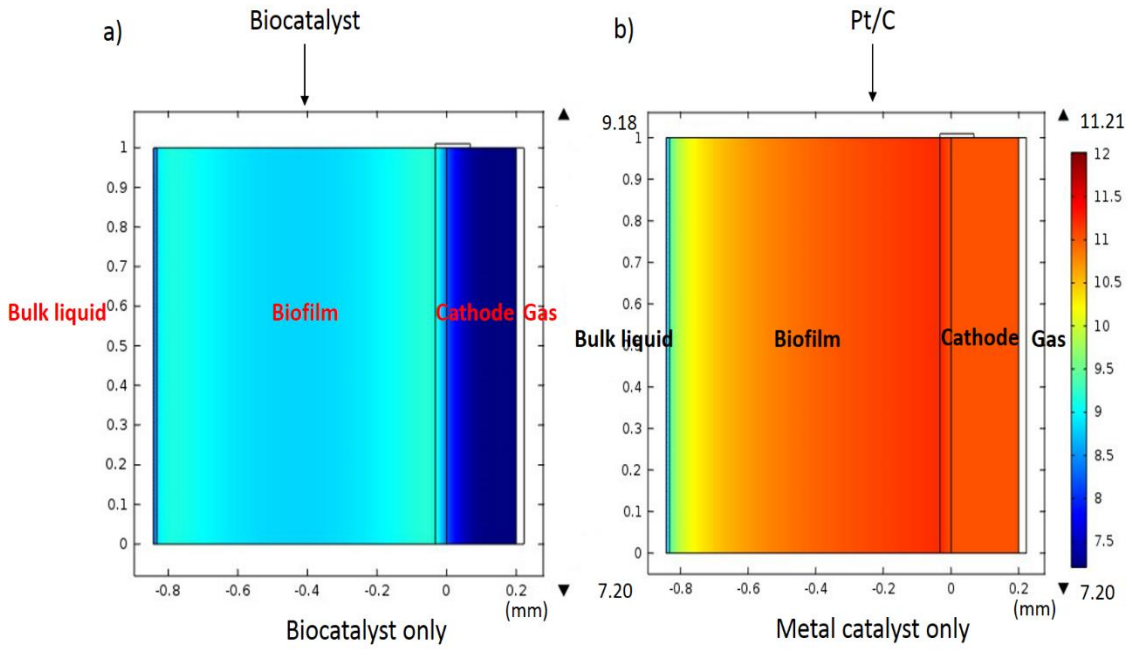

Figure 4.11 pH distribution simulation of the biocatalyst cathode and metal catalyst cathode (Modeling external resistance is 50Ω).

4.3.4 Comparison of the performance of nitrox and heliox as the gas source for air cathode MFC system

Experimental polarization and power density curves were compared for different cathode atmospheres as shown in Figure 4.12 a) [39]. The same flow of nitrox (composed of 80% nitrogen (N_2) and 20% oxygen (O_2)) and heliox (composed of 80% helium (He) and 20% oxygen (O_2)) was employed. As shown in the Figure 4.12 a), the heliox-fed reactor produced slightly more power than the nitrox-fed MFC reactor. The air-fed reactor was passively exposed to air, thus the markedly higher power density yielded by the nitrox/heliox reactors is predominately due to increased gas pressure and improved mass transport; in addition to greater power density, the nitrox/heliox performance was more stable than the passive air reactor. The maximum power density produced by the heliox MFC was 1320 ± 50 mW/m^2 at 75 Ω external resistance, while the nitrox-fed MFC reached a maximum power of 1280 ± 50 mW/m^2, and the air-fed MFC shew the lowest maximum power at 1050 ± 40 mW/m^2. The maximum difference in power density between heliox and nitrox was 95 mW/m^2 at 50 Ω external resistance. Compared the power density curves, the maximum percentage difference is 9.0 %, and average percentage difference is around 3.5 %. Individual electrode potentials were recorded; it is apparent that the cathode potential changed much more than the anode potential indicating much greater cathode overpotential. From the experiment, the heliox and nitrox mixtures clearly yielded better performance for the oxygen-consuming MFC cathode.

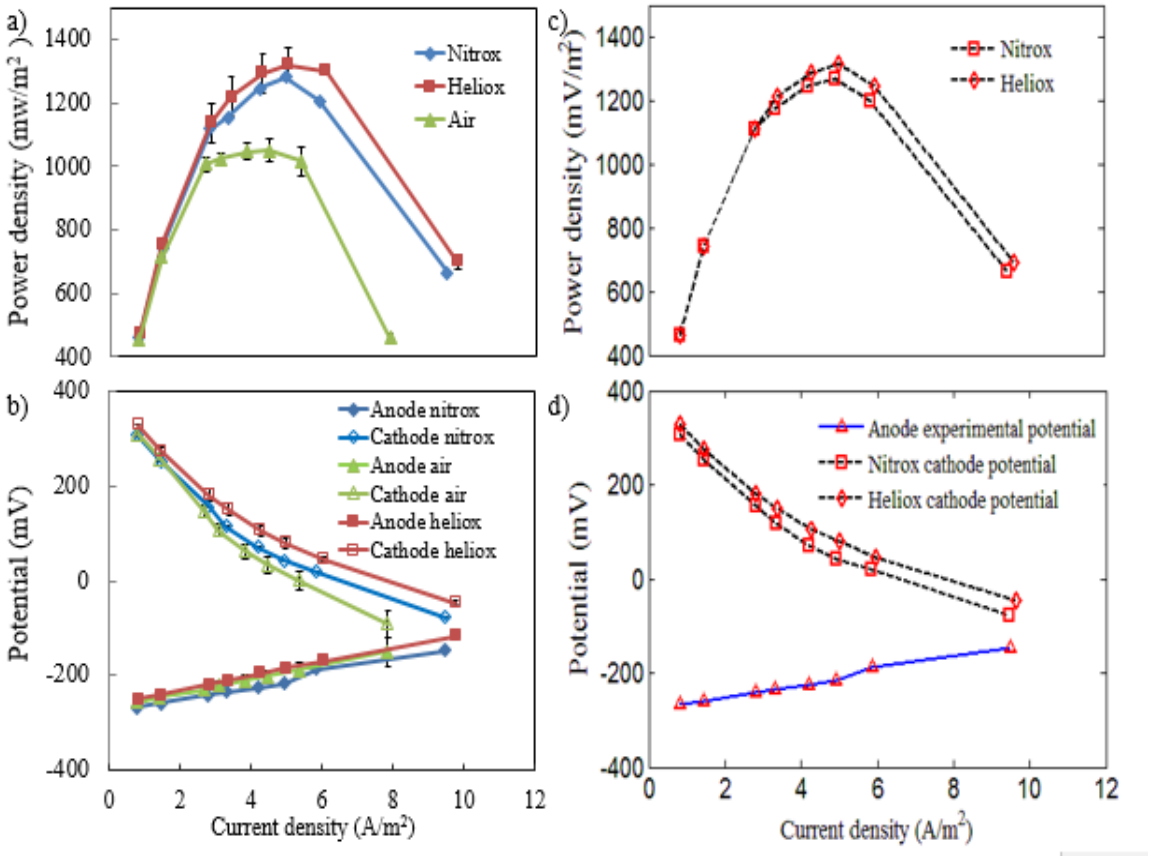

Figure 4.12 Experimental results for nitrox-fed, heliox-fed and air-fed MFCs: a) power density curves; b) polarization curves; steady state simulation results for nitrox-fed, and heliox-fed MFCs: c) power density curves; d) polarization curves.

Because of a small difference in oxygen diffusivity in helium and nitrogen, the heliox facilitated oxygen transport into the cathode, slightly improving performance over the nitrox mixture.

a.) The phenomenon hypothesis

While the performance difference between the nitrox-fed reactor and heliox-fed reactor was small in experiments, it was also consistent. A possible explanation is that oxygen transport and reactions under these two different mixture gases is slightly different. The diffusion coefficient of oxygen is 8.6×10^{-5} m^2/s in helium, compared to 2.3×10^{-5} m^2/s in nitrogen, which allows oxygen to diffuse more rapidly into the cathode, yielding the small performance gain over nitrox. The calculation of binary gas-phase diffusion coefficients can be derived from the Eqn. (4.27),

$$D_{12}\left(\frac{m^2}{s}\right) = \frac{a}{P}\left(\frac{T}{\sqrt{T_1 T_2}}\right)^b (P_1 P_2)^{1/3}(T_1 T_2)^{5/12}\left(\frac{1}{M_1}+\frac{1}{M_2}\right)^{1/2} \qquad (4.27)$$

where D_{12} is the diffusion coefficient of species 1 into species 2, temperature T is in Kelvin and pressure P is in atmosphere. For a nonpolar gas pair, a and b are 2.745×10^{-8} and 1.823, respectively [50]. Diffusion of oxygen into the liquid that floods the carbon cloth does not account for the observed performance difference; however, inclusion of a small volume of gaseous oxygen in the mostly-flooded cathode layer provides enough oxygen to support the results observed. To achieve the performance difference between nitrox and heliox

observed experimentally, the simulated carbon cloth layer required 3 % gas phase and the catalyst included 1 % gas phase by volume.

b.) The assumptions for the simulation

In the cathodic steady state simulation, it was assumed that there were three phases in the carbon cloth domain: solid (carbon cloth), liquid (growth medium) and gas (air, heliox, or nitrox) in the carbon cloth channels. The solid carbon decides the porosity of the diffusion media. The oxygen was assumed to be able to diffuse in both the liquid and gas, noting that all oxygen was fully dissolved at the carbon cloth – Pt/C layer interface. A schematic of the cathode layers is shown in Figure 4.13. The 1-D diffusion equation in the carbon cloth is shown in Eqn. (4.28) [71].

$$\theta \frac{\partial c_{liq}}{\partial t} + a_v \frac{\partial c_{gas}}{\partial t} = \nabla^2 D_{liq} c_{liq} + \nabla^2 D_{gas} c_{gas} \tag{4.28}$$

where θ is the liquid porosity in the carbon cloth (dimensionless), a_v is the gas porosity in the carbon cloth (dimensionless), c_{gas} and D_{gas} are the substance gas phase concentration (mol/m^3) and effective diffusion coefficient (mol/m^2·s) specifically, c_{liq} and D_{liq} are the substance liquid phase concentration (mol/m^3) and effective diffusion coefficient (mol/m^2·s) specifically. Based on the Eqn. (4.10), the Henry's law constant can also show in Eqn. (4.29)

$$H_i = \frac{c_{liq,i}}{c_{gas,i}} \tag{4.29}$$

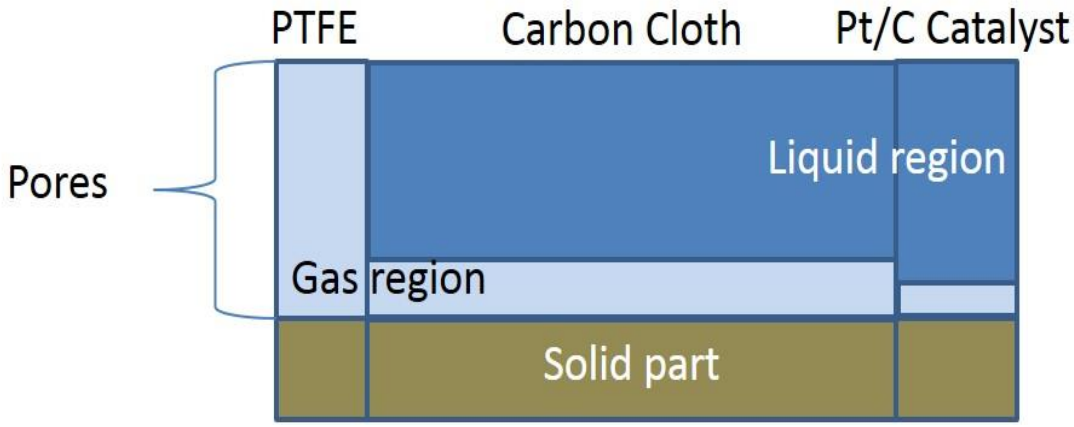

Figure 4.13 The gas diffusion in the cathode materials.

where H_i is the Henry's law constant (dimensionless). The gas effective diffusion coefficient and liquid effective diffusion coefficient can be calculated by the Eqn. (4.30) and Eqn. (4.31).

$$D_{liq} = \theta \pi_L D_L \tag{4.30}$$

$$D_{gas} = a_v \pi_G D_G \tag{4.31}$$

where π_L and π_G are the liquid and gas tortuosity (dimensionless), D_L and D_G are the liquid and gas diffusion coefficient (mol/m^2·s). The Eqn. (4.29), Eqn. (4.30) and Eqn. (4.31) were substituted into Eqn. (4.28), the Eqn. (4.32) was derived.

$$\left(\theta + \frac{a_v}{H_i}\right)\frac{\partial c_{liq}}{\partial t} = \nabla^2 \left(D_L + \frac{D_G}{H_i}\right) c_{liq} \tag{4.32}$$

Then, Eqn. (4.30) and Eqn. (4.31) can be substituted into Eqn. (4.32) to obtain Eqn. (4.33), which described oxygen mass transport in the cathode.

$$\left(\theta + \frac{a_v}{H_i}\right)\frac{\partial c_L}{\partial t} = \nabla^2 \left(\theta \pi_L D_L + \frac{a_v \pi_G D_G}{H_i}\right) c_L \tag{4.33}$$

The cathodic steady state model was evaluated at external resistances of: 10 Ω, 50 Ω, 75 Ω, 100 Ω, 150 Ω, 200 Ω, 500 Ω, 1000 Ω. The measured anodic potentials for the external resistance settings are presented in the Table 4.2. The parameters are also presented in the Table 4.3. With the above considerations regarding oxygen diffusivity in nitrogen and helium, simulated power density and polarization curves are shown in Figure 4.12 c) and Figure 4. 12 d). The simulated maximum power density produced by the heliox reactor is 1314 mW/m^2 at 75 Ω external resistance, while the nitrox reactor achieves a maximum power of 1269 mW/m^2 at 75 Ω external resistance. The simulated maximum

Table 4.2. The anode potential values in different external resistors.

External resistor (Ω)	Anode potential (mV) v.s. Ag/AgCl
10	-147.79
50	-186.13
75	-217.27
100	-225.32
150	-234.96
200	-242.19
500	-259.51
1000	-266.60

Table 4.3. The parameters in the cathodic steady state model.

Name	Description	Values	Unit
$c_{Ac,0}$	Initial Concentration, sodium acetate[a]	800	mg/L
$c_{O2,g}$	Boundary concentration, gaseous oxygen[a]	237.66	mg/L
$c_{O2,ref}$	Reference concentration in reactor, oxygen	3.79	mg/L
$D_{Ac,liq}$	Diffusion coefficient in liquid, acetate[b]	1.21×10^{-9}	m^2/s
$D_{OH,liq}$	Diffusion coefficient in liquid, hydroxide[c]	4.59×10^{-9}	m^2/s
$D_{O2\text{-}He}$	MS diffusivity, O2-He component[b]	8.60×10^{-5}	m^2/s
$D_{O2\text{-}N2}$	MS diffusivity, O2-N2 component[b]	2.30×10^{-5}	m^2/s
$D_{O2,liq}$	Diffusion coefficient in liquid, oxygen[b]	2.10×10^{-9}	m^2/s
E_C^0	Cathode equilibrium voltage[b] (v.s. SHE)	552	mV
F	Faraday constant[b]	96485	C/mol
H_{N2}	Henry constant, nitrogen[b]	1.66×10^{5}	J/mol
H_{O2}	Henry constant, oxygen[e]	7.79×10^{4}	J/mol
i_{lim}	Limit current density	2.5	A/m^2
K_{AcH}	Half-max-rate acetate concentration, heterotrophic biomass	150	mg/mol
K_{O2}	Half-max-rate oxygen concentration in cathode	0.128	mg/L

Table 4.3. Continued.

Name	Description	Values	Unit
K_{O2A}	Half-max-rate oxygen concentration, autotrophic biomass	1.28	mg/L
K_{O2H}	Half-max-rate oxygen concentration, heterotrophic biomass	1.28	mg/L
L_{bio}	Initial length, cathode biofilm	0.01	Mm
L_{bl}	Length, bulk liquid[b]	39.0	Mm
L_{bdl}	Length, boundary diffusion layer[b]	0.5	Mm
L_{cc}	Length, carbon cloth[b]	0.18	Mm
L_{cl}	Length, Pt/C catalyst layer[b]	0.032	Mm
L_{pdl}	Length, PTFE diffusion layer[b]	0.023	Mm
pH_0	pH in bulk liquid	7.08	\
P_0	Gas pressure[b]	1.01×10^{5}	Pa
$q_{max.AcH}$	Maximum specific rate of acetate utilization[e]	5.56×10^{-5}	(mg Ac)/(mg HAB·s)
$q_{max.Acsus}$	Maximum specific rate of acetate utilization	5.56×10^{-6}	(mg Ac)/(mg SUS·s)
$q_{max.O2}$	Maximum specific rate of oxygen utilization	1.46×10^{-7}	g/L·s
$q_{max.AcA}$	Maximum specific rate of oxygen utilization, autotrophic biomass	8.64×10^{-6}	(mg O_2)/(mg AAB·s)
R	Gas constant	8.314	J/mol·K

Table 4.3. Continued.

Name	Description	Values	Unit
$S_{cathode}$	Cathode's cross sectional area in MFC[b]	7.07×10^{-4}	m^2
T	Temperature	303.15	K
ε_{bio}	Porosity, biofilm	0.95	\
ε_{cc}	Porosity, carbon cloth[b]	0.75	\
ε_{cl}	Porosity, Pt/C catalyst layer[b]	0.30	\
ε_{pdl}	Porosity, PTFE diffusion layers	0.10	\
η_K	Cathode half-max overpotential	240.028	mV
ρ_{bl}	Density, bulk liquid[b]	1.05	g/cm^3
ρ_{bio}	Density, bacteria	1.54	g/cm^3
σ	Mass fraction of HAB in biofilm	0.85	\
σ_{bio}	Conductivity, cathode biofilm	0.1	S/m
σ_{bl}	Conductivity, bulk liquid[b]	0.755	S/m
σ_{cc}	Conductivity, carbon cloth	1.00×10^5	S/m

Values for the other model parameters were assumed based on common practical experience.

a from experimental data.

b from Reference [72].

c from Reference [73].

d from Reference [74].

e from Reference [37].

Table 4.3. Continued.

f from Reference [75].

difference in power density is 45 mW/m^2 at 50 Ω external resistance. Compared the power density curves, the maximum percentage difference is 3.6 %, and average percentage difference is around 2.8 %. The simulation results illustrated in Figure 4.12 c) and Figure 4.12 d) show that the simulation results give very good fit to the experimental data in both power density and cathode potentials. It is noted that the two simulated power density curves for nitrox and heliox are slightly closer to each other than they were in the experiments, this phenomena could account for the error range.

In addition to the electrochemical results, the distribution of species such as hydroxide in the cathode was simulated in the steady state model to shed light on the ORR. Figure 4.14 shows the calculated pH distribution in the cathode for heliox-fed and nitrox-fed MFC reactors. The cathode pH in the heliox MFC is consistently higher than that of the nitrox reactor, indicating more rapid oxygen reduction since hydroxide is the product of the ORR. The slope of the pH profile is steeper in the Pt/C catalyst layer than in the biofilm, indicating that the ORR reaction rate in the Pt/C catalyst layer is faster than in the biofilm. As shown in Figure 4.14, the pH of the boundary layer is constrained to 7.08 for the steady state model. One limitation of this current model is that the elevated cathode pH doesn't affect the biomass or catalyst reactions. A future improvement of this model will describe the response of the biomass and Pt/C catalyst layer to the elevated pH present in the cathode.

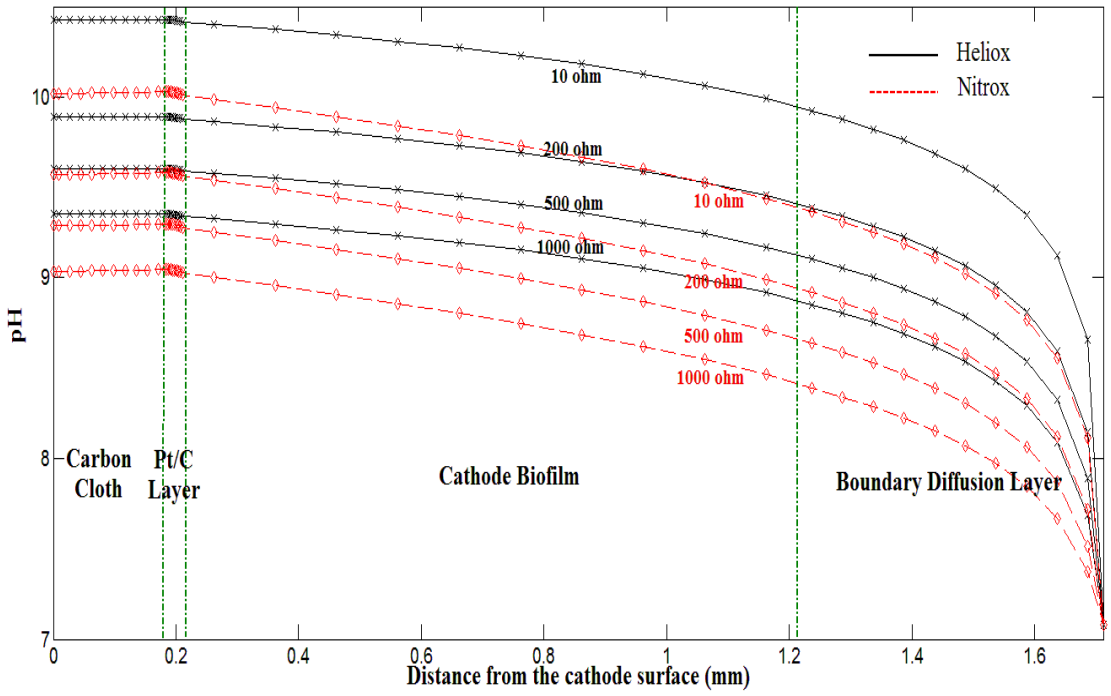

Figure 4.14 Simulation results of pH distribution in cathodic side for nitrox-fed and heliox-fed MFCs.

4.4 Conclusion

The multi-species cathodic steady state model was developed, and a series of simulations was constructed to explore the relationship between power density and electrochemical potentials. The cathode was found to dominate the MFC overpotential at all operating currents, indicating that all three contributions to overpotential are more limiting in the cathode. Such insight provides guidance for the greatest opportunity for improvement in the system. Throughout the range of current density, activation and ohmic overpotentials dominated the full cell performance. Besides, the cathode model predicted that, while both bacteria and Pt perform oxygen reduction in the cathode, the bacterial contribution to current was less than 10 %. With the commercial software COMSOL, the distribution of oxygen in cathode materials were presented to reflect the ORR in the air-cathode MFC system. It is known that the primary contribution of the cathode biofilm bacteria is to prevent oxygen from crossing over to the anaerobic anode.

Combining with the experiment, its results were used to test the hypothesis that mass transport in the cathode strongly affects power output of an air cathode MFC. A heliox-fed reactor produced higher power than the nitrox-fed reactor (the maximum power output of heliox-fed reactor is 1314 mW/m^2, while the maximum power output of the nitrox-fed reactor is 1269 mW/m^2.) Improved diffusion of oxygen in heliox allowed more oxygen in gaseous, porous cathode materials, leading to more rapid oxygen reduction in the cathode. Simulation

results support the experimental result that cathodic overpotentials have a greater influence on the power production than the anode overpotential.

CHAPTER V

CATHODIC HALF-CELL TRANSIENT MODEL IN MFC

This chapter will discuss the construction for the cathodic transient model and its simulation analysis. Biomass growth and the air cathode have been shown to affect total cell performance, shown experimentally [23], while it is hard to observe the change of the chemical substances and biomass species growth directly in experiments. The transient model was used for the evaluation of the materials change and distribution in the reactor over time. This transient model considered the transport of the dissolved oxygen (D.O.), acetate, and hydroxide (OH^-) through both cathodic materials and the bulk liquid in a single chamber MFC reactor. Also the biomass competition would be presented by the transient model: the AAB and the HAB competed in the cathodic biofilm for growth source, the biofilm density and thickness were influenced by the biomass competition and the concentration of the acetate, electrons in the cathodic electron and the dissolved oxygen; at the same time, the suspended biomass was added into this model, and it showed the effects to the distribution to chemical substances in the reactor and to the whole MFC performance as well. Some assumptions in the transient model were the same as they were for the steady state model: It was assumed that potential losses were governed by the production and transport of hydroxide from the cathodic electrode [23]; Additionally, the biomass movement in the biofilm was simulated affected by the diffusion, and the biofilm growth was influenced by the biomass density. The bulk liquid was simulated to be renewed

every 48 hours (the concentration of acetate and dissolved oxygen was reset to initial values), this assumption was similar to the experiment procedure that the MFC reactor liquid is replaced every two days, it avoided the depletion of the acetate and the negative effects to MFC performance.

5.1 Cathode Structure for Transient Model

The model structure in the cathodic transient model was similar to it was in the cathodic steady state model except two differences: The bulk liquid part was considered by the transient model, since the concentration distributions of the suspended biomass, acetate and dissolved oxygen were evaluated and compared with they were in the cathodic materials; The second one was that the transient model deleted the calculation for the gas transport part in the PTFE layer, it was assumed that the oxygen concentration was a constant at the boundary of the cathodic gas phase side.

Figure 5.1 shows the structures, domains, some boundary conditions, and initial values in the transient model. There are five domains in the transient model (from left to right): the carbon cloth, the Pt/C catalyst layer, the biofilm, the boundary diffusion layer, and the bulk liquid. The domain size scale in Figure 5.1 are not the same as it is in the model, the actual sizes are presented in Table 5.1. The material of the boundary diffusion layer is the bulk liquid, it is the region in the vicinity of the cathodic electrode where the concentrations are different from their value in the bulk solution. The definition of the thickness of the

Table 5.1. Domain thickness in the cathodic transient model.

	Thickness (mm)	Initial thickness (mm)
Carbon cloth	0.18	\
Pt/C Catalyst layer	0.032	\
Cathodic biofilm	\	0.01
Boundary diffusion layer	0.50	\
Bulk liquid	39.00	\

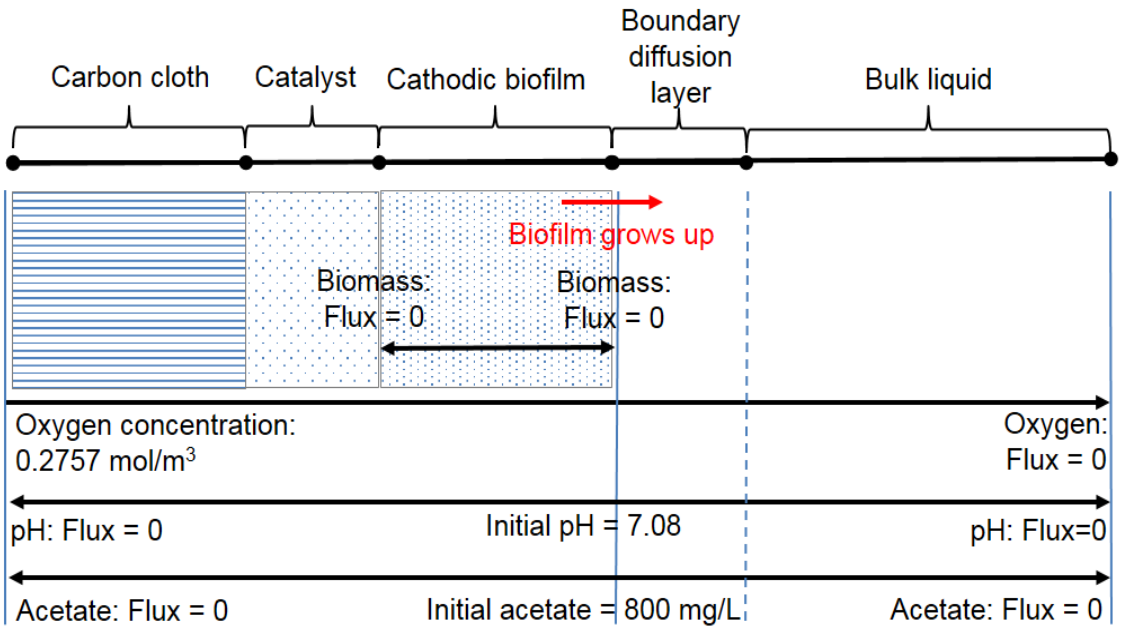

Figure 5.1 The structure for the cathodic transient model**.**

diffusion layer is arbitrary because the concentration approaches asymptotically the value in the bulk solution [76]. In the model, the thickness is defined to be 0.5 mm.

5.2 Methods for Cathodic Transient Model

The cathode biofilm growth, competition between two biomass metabolic cultures, and the mass transport changes in both bulk liquid and cathode over 15 days were described in the transient model. The transient model was written by C++ in the Linux system and computed by the Newton – a high performance computer at the University of Tennessee. The electrochemical equations and biochemical reactions were calculated based on their stoichiometry constants and rate parameters, shown in the Table 5.2. It takes 12 ~ 16 hours to output the concentration of substances in cathode, and the biofilm growth in the external resistor 50 Ω. Some computational skills were applied into this model to speed up the calculation.

5.2.1 Parallel computation

High Performance Computing (HPC) often means heavy-duty computing on clusters or supercomputers with 100s of thousands of cores. The simulation for the cathodic biofilm and substances transport in the cathodic transient model needed the HPC computing skills to realize the modeling in an acceptable time. This transient model applied with the parallel computation.

Table 5.2. Model parameters for cathode simulation.

Name	Description	Values	Unit
b_{decay}	Biomass decay rate[d]	3.00×10^{-6}	1/s
$c_{Ac,0}$	Initial Concentration, sodium acetate[a]	800	mg/L
$c_{O2,g}$	Boundary concentration, gaseous oxygen[a]	237.66	mg/L
$c_{O2,ref}$	Reference concentration in reactor, oxygen	3.79	mg/L
$D_{Ac,liq}$	Diffusion coefficient in liquid, acetate[b]	1.21×10^{-9}	m^2/s
$D_{bio,liq}$	Diffusion coefficient in liquid, biomass	1.50×10^{-11}	m^2/s
$D_{OH,liq}$	Diffusion coefficient in liquid, hydroxide[c]	4.59×10^{-9}	m^2/s
$D_{O2,liq}$	Diffusion coefficient in liquid, oxygen[b]	2.10×10^{-9}	m^2/s
E_C^0	Cathode equilibrium voltage[b] (v.s. SHE)	552	mV
F	Faraday constant[b]	96485	C/mol
i_{lim}	Limit current density	2.5	A/m^2
k_{det}	Biofilm detachment coefficient	1.00×10^{-2}	$g/m^4{\cdot}s$
K_{AcH}	Half-max-rate acetate concentration, heterotrophic biomass	150	mg/mol
K_{O2}	Half-max-rate oxygen concentration in cathode	0.128	mg/L
K_{O2A}	Half-max-rate oxygen concentration, autotrophic biomass	1.28	mg/L

Table 5.2. Continued.

Name	Description	Values	Unit
K_{O2H}	Half-max-rate oxygen concentration, heterotrophic biomass	1.28	mg/L
L_{bio}	Initial length, cathode biofilm	0.01	Mm
L_{bl}	Length, bulk liquid[b]	39.0	Mm
L_{bdl}	Length, boundary diffusion layer[b]	0.5	Mm
L_{cc}	Length, carbon cloth[b]	0.18	Mm
L_{cl}	Length, Pt/C catalyst layer[b]	0.032	Mm
pH_0	pH in bulk liquid	7.08	\
P_0	Gas pressure[b]	1.01×10^{5}	Pa
$q_{max.AcH}$	Maximum specific rate of acetate utilization[e]	5.56×10^{-5}	(mg Ac)/(mg HAB·s)
$q_{max.Acsus}$	Maximum specific rate of acetate utilization	5.56×10^{-6}	(mg Ac)/(mg SUS·s)
$q_{max.O2}$	Maximum specific rate of oxygen utilization	1.46×10^{-7}	g/L·s
$q_{max.AcA}$	Maximum specific rate of oxygen utilization, autotrophic biomass	8.64×10^{-6}	(mg O_2)/(mg AAB·s)
R	Gas constant	8.314	J/mol·K
$S_{cathode}$	Cathode's cross sectional area in MFC[b]	7.07×10^{-4}	m^2
T	Temperature	303.15	K
X_{bio0}	Initial concentration in biofilm, total biomass	3.0	g/L

Table 5.2. Continued.

Name	Description	Values	Unit
X_{sus0}	Initial suspended concentration in liquid, total biomass	0.005	g/L
ε_{bio}	Porosity, biofilm	0.95	\
ε_{cc}	Porosity, carbon cloth[b]	0.75	\
ε_{cl}	Porosity, Pt/C catalyst layer[b]	0.30	\
η_K	Cathode half-max overpotential	240.028	mV
ρ_{bl}	Density, bulk liquid[b]	1.05	g/cm^3
ρ_{bio}	Density, bacteria	1.54	g/cm^3
σ	Mass fraction of HAB in biofilm	0.85	\
σ_{bio}	Conductivity, cathode biofilm	0.1	S/m
σ_{bl}	Conductivity, bulk liquid[b]	0.755	S/m
σ_{cc}	Conductivity, carbon cloth	1.00×10^5	S/m
σ_{cl}	Conductivity, Pt/C catalyst layer	1.00×10^3	S/m

Values for the other model parameters were assumed based on common practical experience.

a from experimental data.

b from Reference [72].

c from Reference [73].

d from Reference [74].

e from Reference [75].

Parallel computing is a form of computation in which multiple calculations are carried out simultaneously [77]. Various substances diffuse through the cathodic materials concurrently, and the chemical/electrochemical/biological reactions were able to adopt in the calculating simultaneously. If the calculation for these substances in MFC system is executed in series, the calculation time for this transient model would be more than 200 hours for 15 days simulation. For this reason, the computational efficiency of the series computing is unsatisfying. If these equations were able to be concurrently executed, the calculation time would be reduced. Generally the parallel computing includes two methods: MPI (Message Passing Interface); and OpenMP (Open Multi-Processing). This transient model applied with the OpenMP to increase the calculation speed in the modeling research.

The MPI is a library specification for message-passing, proposed as a standard by a broadly based committee of vendors, implementers, and users [78]. Distributed memory systems are required for the MPI approach. In the computers (such as clusters of computers, supercomputers with the distributed memory), each processor has its own memory and caches. Specific instructs are needed to transfer the data between processors, and the transferring data is slow. OpenMP can only be used on shared memory systems with a single address space used by all threads. In the computers with the shared memory, all processors have access to the same memory. In the multicore chips, the L1 caches are separated and the L2 caches might be shared [79].

For the multi-threaded program on the dual-core computer, the program code, program counter, call stack are needed to add for the thread control. The threads may be spawned and destroyed as computation proceeds, the flow diagram are shown in the Figure 5.2. The OpenMP is a parallel computation method that implements the multi threads simultaneously by different computer threads. Although the OpenMP has shared memory, it can only successfully use multiple threads when each thread calculation is independent of the calculations occurring on other threads, and it avoids message transfer in different, separated memories and simplifies the coding design. As a result of these features, the OpenMP was applied to the transient model as described by the flow diagram shown in Figure 5.3 which presents the OpenMP coding flow chart in the cathodic transient model. In the substance concentration calculation parts, the reaction rates for different substances in the MFC reactor were computed separately in different threads, and the mass transport equations for different substances were also distributed across several threads for calculation.

5.2.2 Biological time scale consideration

The MFC reactions and transport processes occur at very different time scales [80]. Consideration of the time scales in to the calculation algorithm is helpful to increase computational efficiency, since the physical, chemical, and biological growth in the model has very different reaction rates. The order of magnitude of the characteristic times for molecular diffusive transport, biomass

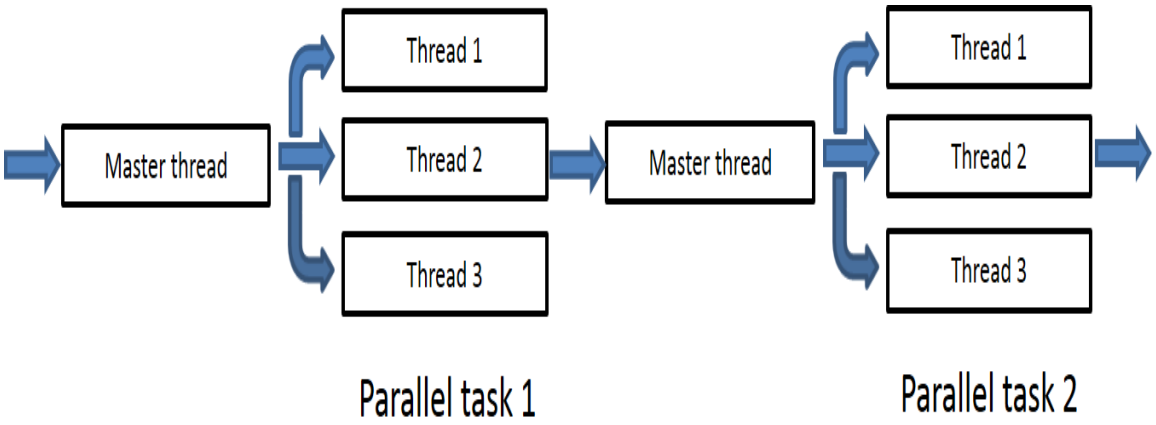

Figure 5.2 OpenMP flow diagram**.**

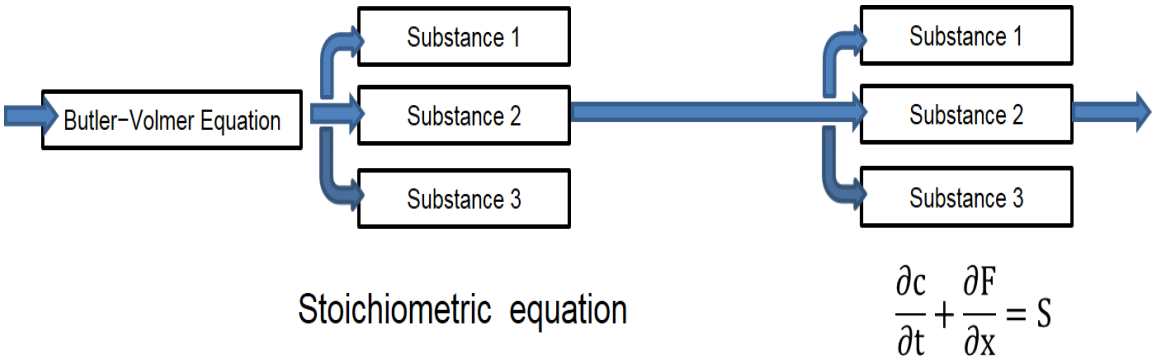

Figure 5.3 Flow diagram of OpenMP applied in the cathodic transient model**.**

growth, biomass decay and biomass detachment are presented in the Table 5.2. The magnitude of the diffusion coefficients in liquid are in the range from 10^{-9} to 10^{-11}, while the magnitude of the biofilm detachment coefficient is 10^{-2}. The processes that impact the biofilm thickness are much slower than the mass transport of chemical substances If only one time scale in the transient model, the smallest chemical time scale must be satisfied [81], determined by the calculation shown in the Eqn. (5.1).

$$\Delta t = \gamma \frac{\Delta x_{min}^{\ 2}}{2D_{max}} \tag{5.1}$$

where Δt is the simulation step time (s), $\gamma = 0.95$ which is the convergence factor (dimensionless), Δx_{min} is the smallest control volume in the model (m), and D_{max} is the largest diffusion coefficient (m^2/s). Because the biomass density and biofilm growth components change relatively slowly, they do not need to be computed in every time step associated with transport or chemical reaction. Therefore, the biofilm growth time step (Δt_{bio}) was adopted in the algorithm. As shown in Figure 5.4, biofilm growth computation was not executed unless the biofilm growth step time Δt_{bio} was exceeded. The biofilm step time was assumed to be 5 mins in the simulation.

By applying the OpenMP and the chemical/biological time scales into the cathodic transient model, the calculation in different coding part was computed simultaneously, and the computing time was largely reduced. Table 5.3 presents the computing time comparison in different operation system and computation methods after the chemical/biological time scales were added into the codes. In

Table 5.3. Computation time comparison in different environments and methods (Time scale considered).

	Trial 1	**Trial 2**	**Trial 3**	**Trial 4**
Windows system	√			
Linux system		√	√	
OpenMP			√	√
HPC (Newton)				√
Running time	37 hours	29 hours	22 hours	16 hours

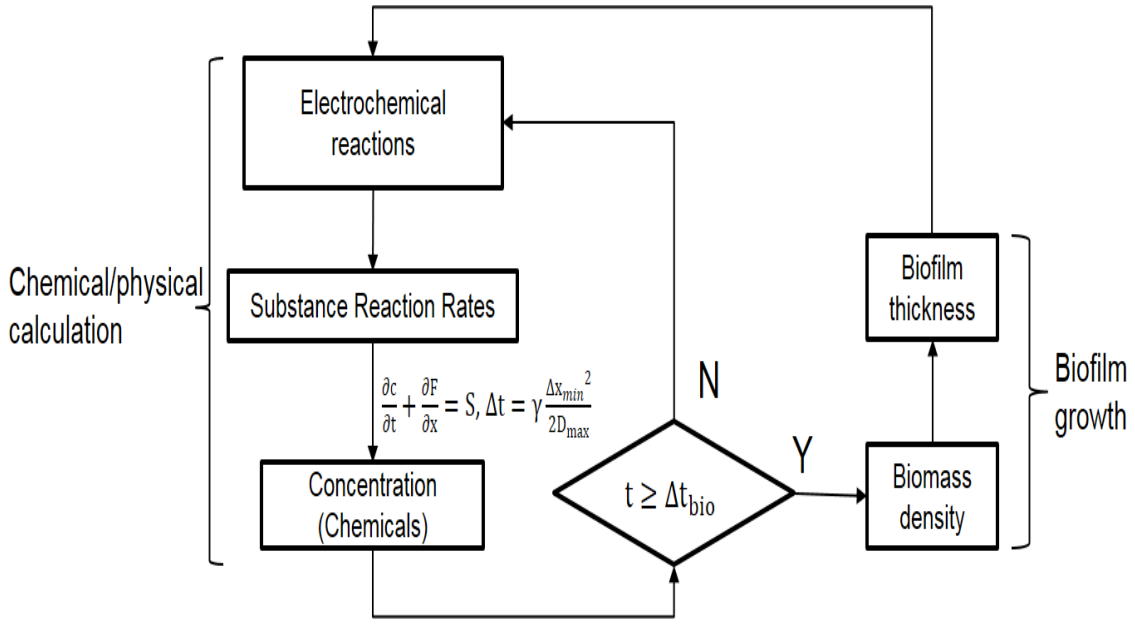

Figure 5.4 The hybrid step time for the chemical substance and biofilm growth calculation.

the Windows system, the code was executed by the NetBeans IDE 7.4, it spent around 37 hours to get the simulation results. However, with the OpenMP and running the same codes in the high performance computer (Newton), it only spent around 16 hours to get all the simulation results.

5.2.3 Mass balance

In the air-cathode MFC reactor, oxygen diffuses from air through the cathode structure into bulk liquid, the oxygen experiences both gas and liquid phases. Henry's law, shown in the Eqn. (5.2), is used to describe the equilibrium between dissolved oxygen and gaseous oxygen at the PTFE-carbon cloth interface.

$$\mathrm{H}_{\mathrm{O}_2,\mathrm{cc}} = \frac{\mathrm{c}_{\mathrm{O}_2,\mathrm{gas}}}{\mathrm{c}_{\mathrm{O}_2,\mathrm{aq}}} \tag{5.2}$$

where $c_{O2,aq}$ is the concentration of dissolved oxygen (mg/L), $c_{O2,gas}$ is the concentration of gaseous oxygen (mg/L), and $H_{O2,cc}$ is the Henry's law constant (dimensionless).

For mass transport in the cathode, a transient mass balance is the basis for both steady state and transient state models, as shown in Eqn. (5.3).

$$\frac{\partial \mathrm{c_i}}{\partial \mathrm{t}} = \mathrm{D_i}\frac{\partial^2 \mathrm{c_i}}{\partial \mathrm{x}^2} + \mathrm{r_i} \tag{5.3}$$

where i is the substance in cathode, c_i is the concentration of species i, D_i is the effective diffusion coefficient, and r_i is the reaction rate of species i for each mobile species.

The explicit Finite Volume Method was used as the computational method for the modeling calculations. Concentrations were calculated at discrete control volumes on a meshed layer. Eqn. (5.3) can be approximated, as shown in Eqn. (5.4):

$$c_k^{n+1} = c_k^n + \frac{\Delta t}{\Delta x} D\left(F_{k-1/2}^n - F_{k+1/2}^n\right) + r_k^n, \quad k = 1\,,\, 2, \cdots,\, M \tag{5.4}$$

where k is the sequence number for the control volume, n is the iteration, Δt is the step time, Δx is the length of the control volume, F is mass flux, and M is the total number of the control volume. Because each species diffuses from layer to layer, the concentration calculation must be solved between each layer. As shown in Figure 5.5, the concentration flux at a control volume boundary can be calculated as shown in Eqn. (5.5) and Eqn. (5.6).

$$F_{left}^n = D_1 \frac{c_b^n - c_{M_1}^n}{\Delta x_1} \tag{5.5}$$

$$F_{right}^n = D_2 \frac{c_{M_1+1}^n - c_b^n}{\Delta x_2} \tag{5.6}$$

where c_b is the boundary concentration, M_1 is the serial number of a control volume, and Δx_1 and Δx_2 are the length of control volumes in Layer 1 and Layer 2. Since mass is conserved, the flux at the boundaries does not change. Therefore the equations for calculating concentration as well as boundary flux can be shown in Eqn. (5.7) and Eqn. (5.8):

$$c_b^n = \frac{\Delta x_2 D_1 c_{M_1}^n + \Delta x_1 D_2 c_{M_1+1}^n}{\Delta x_1 D_2 + \Delta x_2 D_1} \tag{5.7}$$

$$F_{M_1+\frac{1}{2}}^n = F_{left}^n = F_{right}^n = -D_2 \frac{c_{M_1+1}^n - c_b^n}{\frac{1}{2}\Delta x_2} \tag{5.8}$$

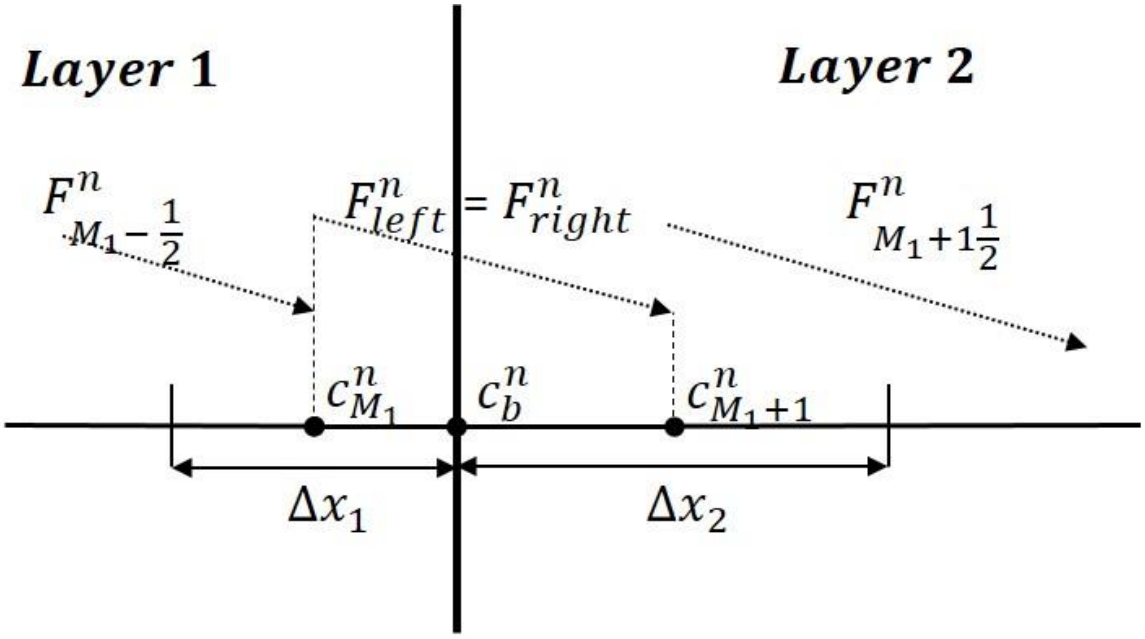

Figure 5.5 Schematic of boundary between two domains**.**

5.2.4 Electron balance

Electron transfer in the biofilm has been investigated extensively, yielding several theories to describe the mechanisms by which electrons are transferred from the microbes to an electrode; these include chemical shuttles produced by microorganisms, protein nanowires, and chemically active redox enzymes added from an external source [82]. Recent research has considered the conductivity of the biofilm itself found at the anode and cathode [10, 83, 84]. Despite uncertainty regarding the mechanism for electron transfer in the biofilm, the cathode current can be simulated based on the electrochemical equations for the cathode biofilm and cathode catalyst layer, as shown in Eqn. (5.9) and Eqn. (5.10).

$$0 = \frac{\partial \mathrm{i_{cl}}}{\partial \mathrm{x}} + \frac{\gamma_{\mathrm{cl}} \mathrm{Fr_{O_2,cl}}}{\mathrm{M_{O2}}} \tag{5.9}$$

$$0 = \frac{\partial \mathrm{i_{bio}}}{\partial \mathrm{x}} + \frac{\gamma_{\mathrm{bio}} \mathrm{Fr_{O_2,AAB}}}{\mathrm{M_{O2}}} \tag{5.10}$$

where i is the current density (A/m^2), γ is the electron equivalence (mol e^-/mol O_2). The total current is the sum of the current density in the biofilm and catalyst layer, as shown in Eqn. (5.11):

$$\mathrm{I} = (\int \mathrm{i_{cl}} \mathrm{dx} + \int \mathrm{i_{bio}} \mathrm{dx}) \mathrm{S_{area}} \tag{5.11}$$

where I is the current from the external circuit into the cathode, and S_{area} is the geometric cathode area (m^2).

In experiments, the out circuit of the microbial fuel cell was connected to an external resistance (R_{ext}), and the cell voltage was calculated based on Eqn. (5.12) when the current is measured for a particular resistor:

$$V_{cell} = IR_{ext} \tag{5.12}$$

It is noted that, due to voltage losses, the actual voltage measured for an MFC is less than the theoretical value at open circuit and any operating current. The voltage losses are roughly divided into activation overpotential η_{act}, concentration overpotential η_{con}, and ohmic overpotential η_r. These three overpotentials dominate at different current densities: activation overpotential in the low-current region, ohmic overpotential at moderate cell current, and concentration overpotential at the highest current densities achieved by a system [37]. In an MFC, the operating voltage can be described as the departure from equilibrium voltage caused by the various overpotentials:

$$V_{cell} = \left(E_C^0 - |\eta_{C,act}| - |\eta_{C,con}|\right) - \left(E_A^0 + |\eta_{A,act}| + |\eta_{A,con}|\right) - |\eta_r| \tag{5.13}$$

where E_C^0 is the cathode equilibrium voltage (mV), E_A^0 is the anode equilibrium voltage (mV). The ohmic overpotential is calculated by the Eqn. (5.14).

$$|\eta_{ohm}| = I(R_A + R_{bl} + R_C) \tag{5.14}$$

where R_A is the electronic resistance of the anode (Ω), R_{bl} is the ionic resistance of bulk liquid (Ω), and R_C is the electronic resistance of cathode (Ω). Development of a concentration gradient, when electrochemical current is comparable to mass transport rate, leads to concentration overpotential [37], described in Eqn. (5.15).

$$\eta_{con} = \frac{RT}{4F} \lg\left(1 - \frac{i}{i_{o,C}}\right) \tag{5.15}$$

where $i_{0,C}$ is the cathode limiting current density (A/m^2) [37].

Because this work only simulated the cathode in a MFC reactor, experimental anode potentials were used in the Eqn. (5.16).

$$E_A = E_A^0 - |\eta_{A,act}| - |\eta_{A,con}| - IR_A \quad (5.16)$$

By combining Eqn. (5.15) and the Eqn. (5.16), activation overpotential in the cathode can be described as a function of current and equilibrium potentials.

$$|\eta_{C,act}| = E_C^0 - I(R_{ext} + R_{bl} + R_C) - \frac{RT}{4F}\lg\left(1 - \frac{i}{i_{o,C}}\right) - E_A \quad (5.17)$$

5.3 Cathode Transient Model Analysis

5.3.1 Cathode transient model algorithm

The one-dimensional cathodic transient model was constructed by C++ programming in Linux system. The OpenMP was adopted to increase the computing time. The time scale was also considered in the coding.

With the time scale and OpenMP consideration, the comprehensive algorithm for the cathodic transient model was concluded and shown in Figure 5.6. Similar to the cathodic steady state model, the anode potential was fixed so that the cathode activation overpotential can be calculated based on the first principle electrochemical relation, then the current density was derived from the Bulter-Volmer equation by the calculated overpotentials. According to the stoichiometric relations for the substance in the cathodic model, the reaction rates were derived and the source term in the mass transport equation would be known and applied for calculating the substance concentration distribution in the

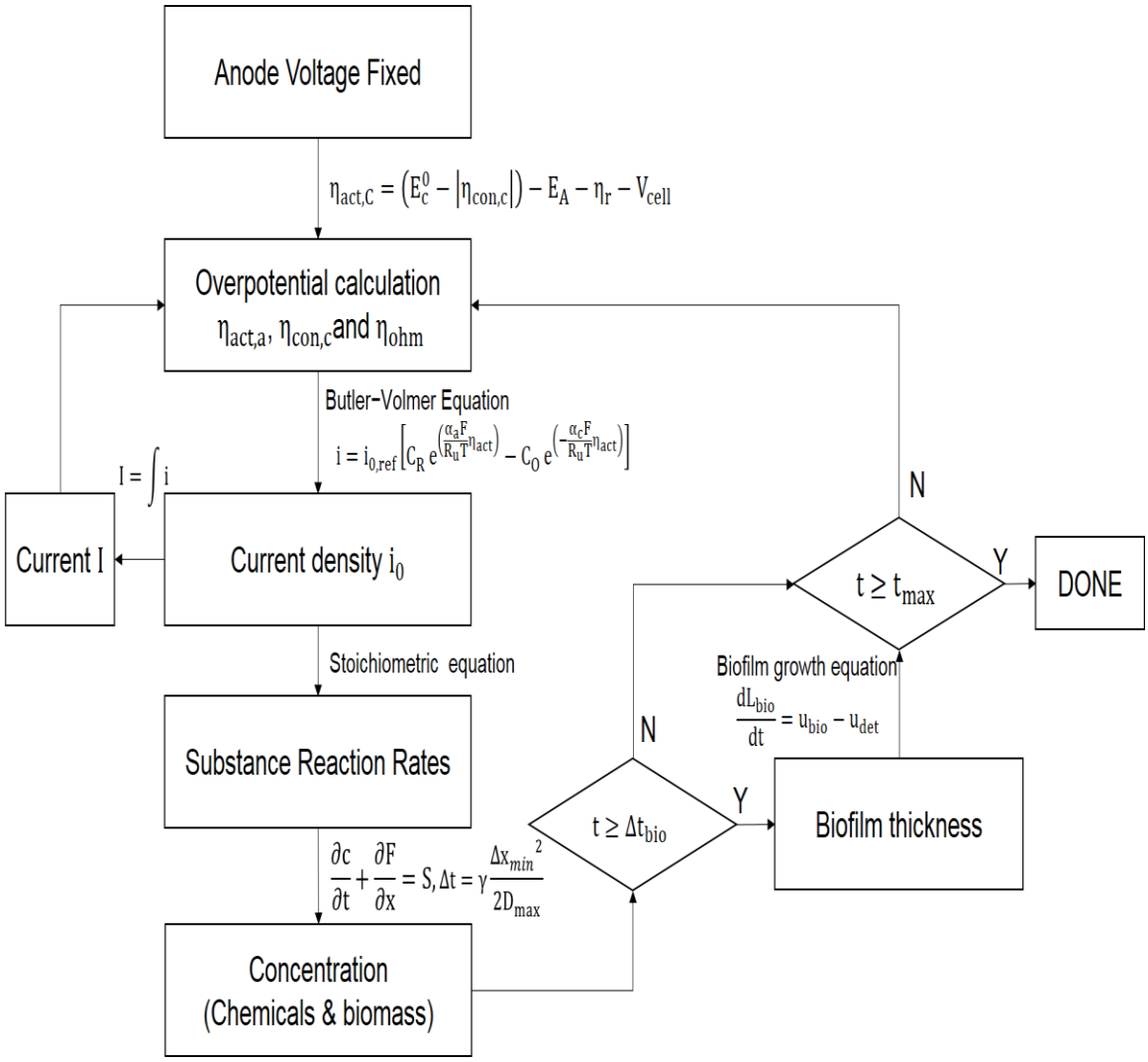

Figure 5.6 The algorithm for the cathodic transient model.

cathodic domains and bulk liquid. The calculation for the chemical and biological substances part adopted the OpenMP that the oxygen (O_2), hydroxide (OH^-), acetate (CH_3COO^-), and biomass density (including AAB and HAB in the cathodic biofilm, and suspended biomass in the bulk liquid) were computed in several parallel threads. After the calculating the chemical and biological substances, the biofilm growth time step were compared. The biofilm thickness was calculated in every biofilm growth step time (Δt_{bio} = 5 mins), or the biofilm thickness calculation part would be neglected if the accumulated time was smaller than the biofilm growth step time Δt_{bio}. Then the updated current was computed based on the new concentration and electrochemical environment. The time was compared with the maximum simulation time, and if the time was larger than the simulation time, the computation was terminated.

5.3.2 Cathode transient model analysis

The cathode transient model focuses on species changes (e.g. biomass, acetate and hydroxide) and the effects of environmental changes on the biomass (AAB, HAB in the cathode biofilm and suspended biomass). Side-reactions that may impact the electrode or membrane materials are not considered in the transient model. A simulation period of 15 days was assumed since experimental cells generally achieved stable performance in this time period. Based on experimental measurements, the range of initial dissolved oxygen (D.O.) across many cell builds was 2.9 – 4.2 mg/L, thus D.O. was set to 4.2 mg/L. Figure 5.7 shows the cathodic biofilm thickness growth, average acetate concentration and

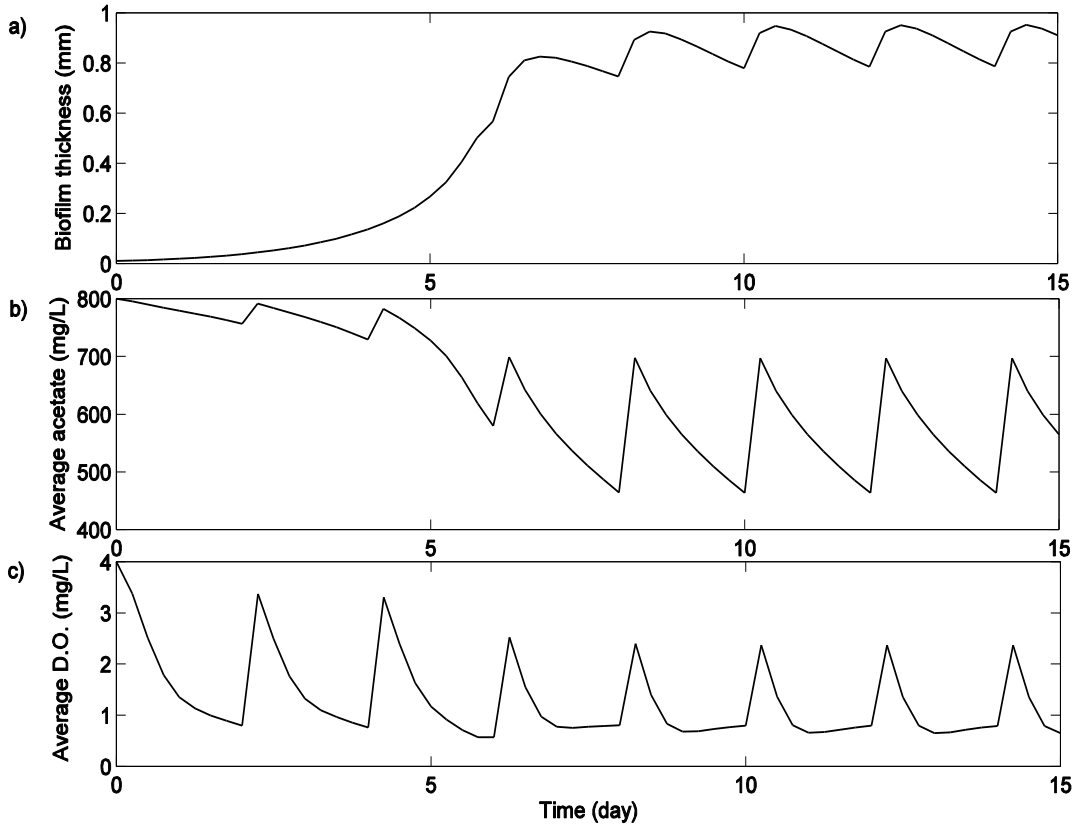

Figure 5.7 Simulation results for cathodic biofilm thickness and average D.O. (dissolved oxygen) in bulk liquid over 15 days: a) Cathodic biofilm thickness; b) average acetate concentration in the reactor; c) average D.O. in the reactor.

average D.O. in the reactor over 15 days. In Figure 5.7 a), the biofilm required almost one week to achieve fully grown thickness approaching 1 mm, which agreed with the cathodic biofilm thickness range observed experimentally. Also the biofilm thickness became stable between 0.8 - 1.0 mm after 7^{th} day, so it is reasonable to assume that the thickness of biofilm is unchanged in the steady state model. Upon reaching a stable, maximum biofilm thickness, the biofilm thickness fluctuates with acetate concentration, as shown in Figure 5.7 b). Two days after each bulk liquid refreshment, most of the acetate is consumed resulting in decreased biomass growth rate as the acetate concentration reaches a minimum. As is apparent in Figure 5.7 c), D.O follows a similar trend, reaching maxima upon each bulk liquid replacement. It can be seen in Figure 5.7 a) and Figure 5.7 c) that the D.O. actually increases slightly over every 2 day cycle from day 8 onward; meanwhile average D.O. starts to shrink after one week when the cathodic biofilm thickness growth becomes stable. It is noted that the anodic biomass functions only in an anaerobic environment, thus it is beneficial for the one chamber MFC system to have the lower D.O. in the bulk liquid possible. Although the cathodic microorganisms compete with the anodic *exoelectrogens* for acetate, the cathodic biofilm minimize oxygen diffusion into the bulk with suspended biomass further removing oxygen from the bulk liquid before reaching the anode.

The cathodic time dependent model simulated three types of biomass: HAB, AAB and suspended biomass. Figure 5.8 shows the average density of the

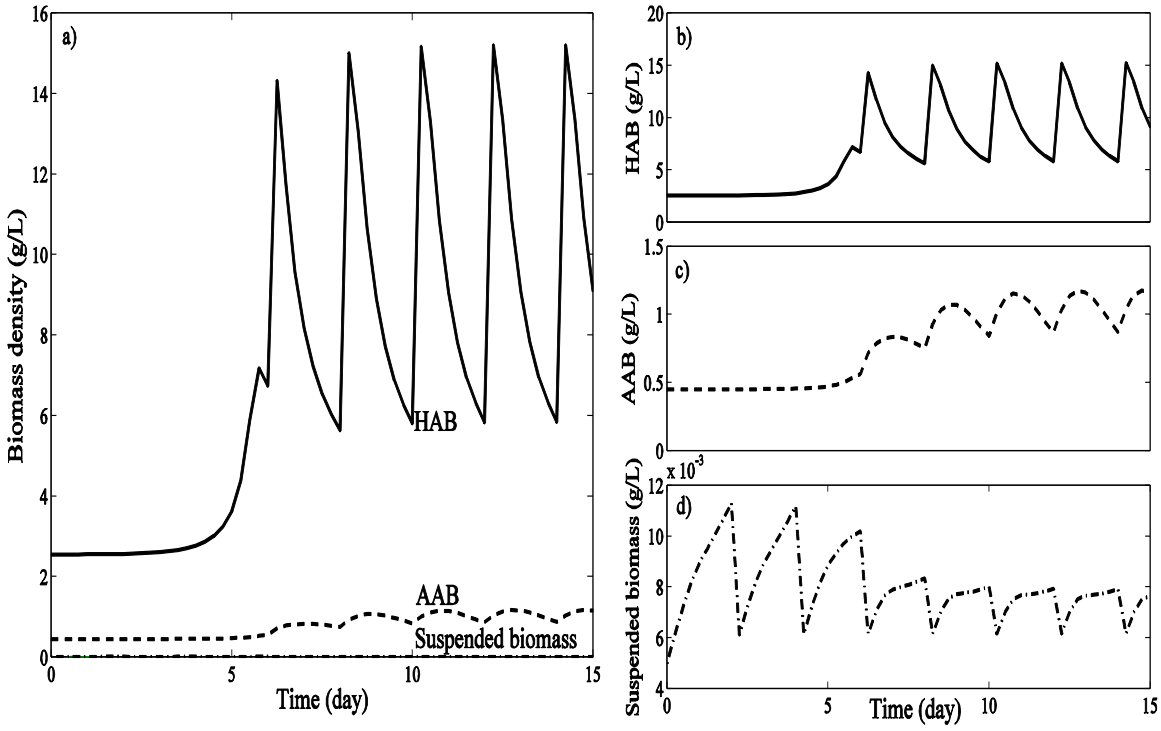

Figure 5.8 Simulation results for cathodic average HAB, AAB and average suspended biomass in bulk liquid over 15 days: a) average HAB concentration; b) average AAB concentration; c) average suspended biomass.

biomass over 15 days. In Figure 5.8 a), the biomass densities of these three are compared. The HAB biomass dominates the biofilm population and its density follows the changes in acetate concentration; conversely, AAB growth is relatively stable and only comprises approximately 15 wt% in the cathodic biofilm. Because this simulation neglected the anode biofilm (which is much thinner than the cathode biofilm), the suspended biomass originates from the cathode detached biomass which then can grow in suspension. As shown in Figure 5.8 c), the density of the suspended biomass decreased as the D.O. content decreased in the bulk liquid, but was always four orders of magnitude smaller than the biofilm biomass densities.

Figure 5.9 shows the calculated distribution of the HAB and AAB biomass density in the cathodic biofilm over time. Biomass density increases rapidly, as does the biofilm thickness growth rate. In this simulation, the stable total biomass density is around 16.5 g/L - 18.0 g/L. Zhang and Bishop measured biofilm density experimentally and found a range of 11.1 g/L - 107.8 g/L. The biofilm density depends on biofilm thickness, porosity, and biomass cultures, leading to the difference in the upper limit of biofilm density between this work and the experimental reference [85].

The transport and distribution of D.O. and acetate were also simulated across the cathode. In Figure 5.10, the D.O. distribution is shown. Oxygen is consumed most rapidly in the Pt/C catalyst layer, as indicated by the slope of the oxygen concentration profile. In absolute terms, more D.O. is consumed in the

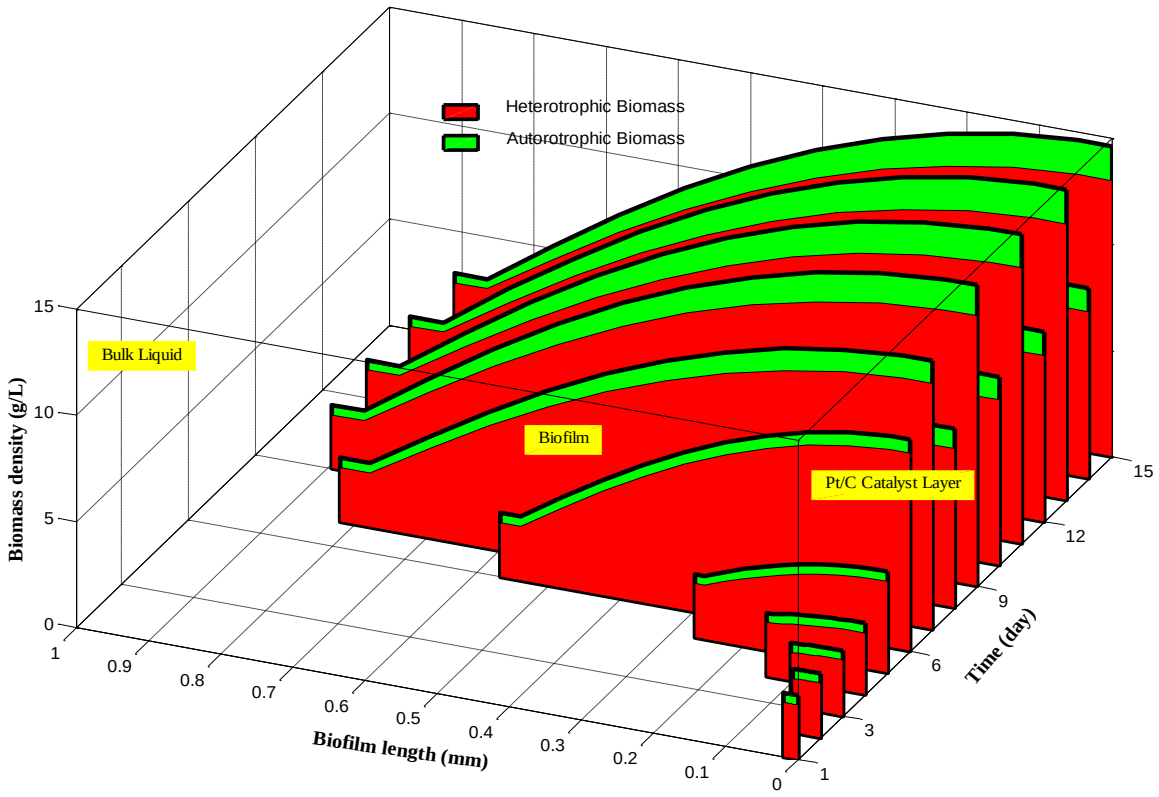

Figure 5.9 Simulation of AAB biomass density and HAB biomass density over 15 days.

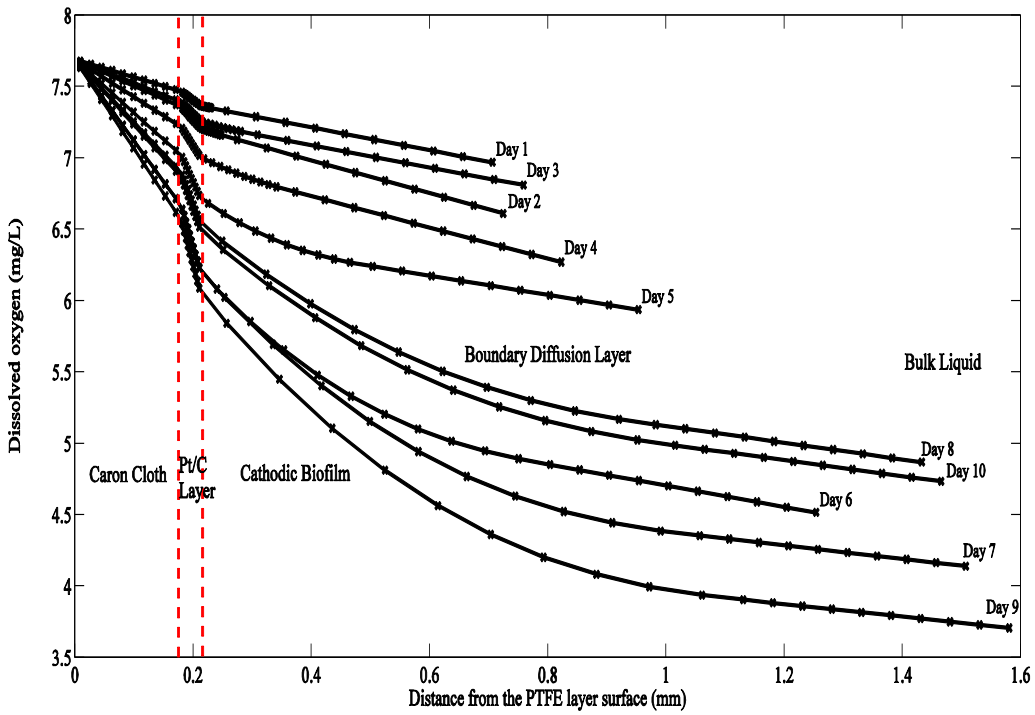

Figure 5.10 Simulation of the dissolved oxygen in cathodic side over 10 days.

cathode biofilm, albeit at a slower rate, than in the Pt/C layer owing to its much greater thickness across the cathode. Figure 5.11 shows the acetate concentration in the full reactor. Because the model neglected the anode biofilm consumption, Figure 5.11 only reflects the acetate consumption in the cathode and suspended biomass.

5.4 Conclusion

A one-dimensional, multi-species time dependent cathode-bulk liquid model was formulated. By adopting the parallel computing schematic – OpenMP and the time scale for biological growth, the simulation successfully output and presented a full picture of the cathode-bulk liquid dynamic environment, and the intrinsic relationship among the chemical/electrochemical/biological parameters was evaluated. The simulation described the density development of each biomass community over half a month cultivation, illustrating the competition between biomass communities in the biofilm and the suspended biomass. Besides, the simulation described the cathodic biomass growth and dissolved species distributions over time. Competition between the anode and cathode biofilms for available acetate was considered, as well as the oxygen-removing contribution the cathode and suspended biomass made to ensure an anaerobic anode.

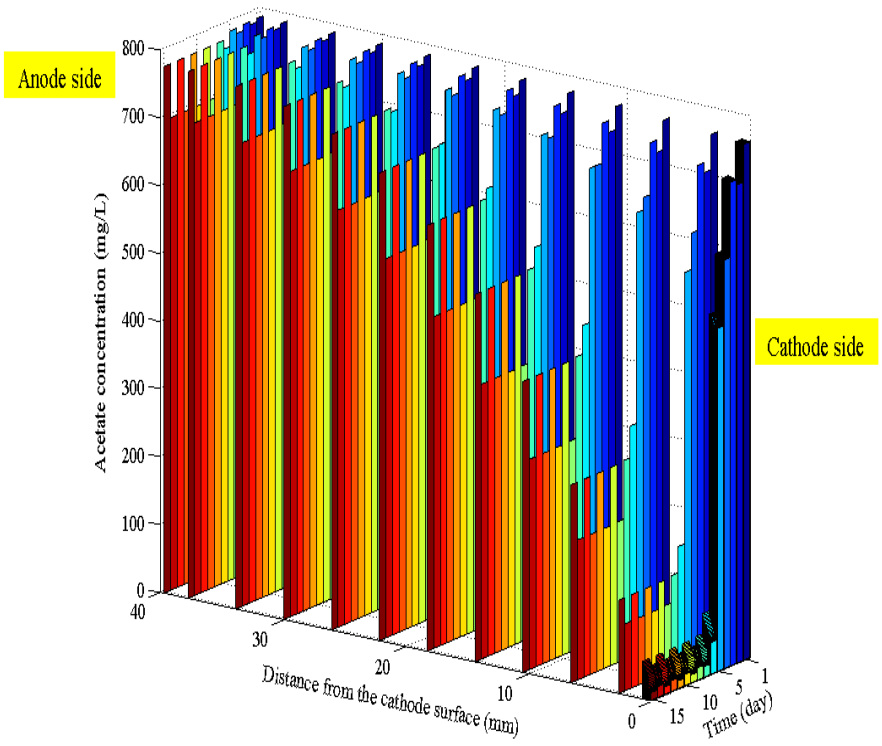

Figure 5.11 Simulation of acetate concentration in MFC reactor over 15 days.

CHAPTER VI

FULL MICORIBAL FUEL CELL STEAD STATE MODEL

This chapter reveals the research work in the computational model for the whole single chamber air-cathode microbial fuel cell system, which firstly coupled the functions of mass transport, biological and electrochemical reactions in both the anodic and cathodic electrodes. Computational fluid dynamics and Monod-Nernst analysis were applied into the model reactions in the cathodic catalyst and biofilms in both electrodes. The integration of the algorithm analysis in this model drew a full picture from a macro-perspective that how the MFC reactor works on electricity generation, and dug the details from a micro-perspective that the mass transport through the electrode materials and reactor liquid. Besides, this model studied the influences by the liquid pH (H^+/OH^- transport) and the electric migration term on the concentration overpotential; and analyzed how the buffers regulate the liquid pH environment in the reactor to improve the power generation of the MFC reactor. The simulation results were compared and validated with the experiment data. The results fitted the experimental potential curves and power density well in different external resistance conditions. Further, this model provided information of the mass transport in different current density and gave quantitative analysis of different overpotentials for anode/cathode in MFC. Overall, this comprehensive modeling system offered an effective method to analyze the inherent relations and optimize the MFC system.

6.1 Full MFC Structure

This model is based on the single chamber air-cathode MFC, the 3D structure is shown in Figure 6.1. The bulk liquid part is cylindrical and it separates the anode and cathode. In this reactor, the anode material is carbon paper and located in the left side, the cathode contains several layers and located in the right side. The ARB attach to the carbon paper and form into a thin biofilm. The carbon paper structure is a flat surface and attached by the biofilm, this design simplifies relations among parameters and optimizes simulation effects, but on the other hand, reduces the MFC power output. On the cathodic side, from inner to outer side, the materials for cathode are: Pt/Carbon catalyst layer, carbon cloth layer, PTFE layer. The structure parameters and constants of the MFC reactor are shown in Table 6.1. In both electrodes, the microorganisms attach to Pt/Carbon catalyst layer and form biofilms, their biofilm thickness is constant in the steady state.

6.2 Methods for Full Cell Steady State Model

6.2.1 Mass balance for substrate transport

The mass transport equations are for the domains in the full cell system. In simulation the reactor is divided into several domains based on the physical properties of the materials. From cathode to anode, they are PTFE layer, carbon cloth, Pt/C catalyst layer, cathodic biofilm, bulk liquid, anodic biofilm and carbon

Table 6.1. Model parameters for full cell steady state model.

Name	Description	Values	Unit
$c_{Ac,0}$	Initial Concentration, sodium acetate [a]	800	mg/L
$c_{O2,g}$	Boundary concentration, gaseous oxygen [a]	237.66	mg/L
$c_{O2,ref}$	Reference concentration in reactor, oxygen	3.79	mg/L
$D_{Ac,liq}$	Diffusion coefficient in liquid, acetate [b]	1.21×10^{-9}	m^2/s
$D_{CO3,liq}$	Diffusion coefficient in liquid, CO_3^{2-} [c]	8.00×10^{-10}	m^2/s
$D_{HCO3,liq}$	Diffusion coefficient in liquid, CO_3^{2-} [c]	1.09×10^{-9}	m^2/s
$D_{H2CO3,liq}$	Diffusion coefficient in liquid, $H2CO_3$ [c]	1.09×10^{-9}	m^2/s
$D_{HPO4,liq}$	Diffusion coefficient in liquid, HPO_4^{2-} [c]	7.60×10^{-10}	m^2/s
$D_{H2PO4,liq}$	Diffusion coefficient in liquid, $H2PO_4^{-}$ [c]	8.80×10^{-10}	m^2/s
$D_{H3PO3,liq}$	Diffusion coefficient in liquid, $H3PO_4$ [c]	1.00×10^{-9}	m^2/s
$D_{NH3,liq}$	Diffusion coefficient in liquid, NH_3 [c]	1.64×10^{-9}	m^2/s
$D_{NH4,liq}$	Diffusion coefficient in liquid, NH_4^{-} [c]	1.97×10^{-9}	m^2/s
$D_{OH,liq}$	Diffusion coefficient in liquid, hydroxide [c]	4.59×10^{-9}	m^2/s
$D_{O2,liq}$	Diffusion coefficient in liquid, oxygen[b]	2.10×10^{-9}	m^2/s

Table 6.1. Continued.

Name	Description	Values	Unit
E_C^0	Cathode equilibrium voltage[b] (v.s. SHE)	552	mV
F	Faraday constant[b]	96485	C/mol
K_{AcH}	Half-max-rate acetate concentration, heterotrophic biomass	150	mg/mol
K_{O2}	Half-max-rate oxygen concentration in cathode	0.128	mg/L
K_{O2A}	Half-max-rate oxygen concentration, autotrophic biomass	1.28	mg/L
K_{O2H}	Half-max-rate oxygen concentration, heterotrophic biomass	1.28	mg/L
L_{bio}	Initial length, cathode biofilm	0.01	mm
L_{bl}	Length, bulk liquid [b]	39.0	mm
L_{bdl}	Length, boundary diffusion layer [b]	0.5	mm
L_{cc}	Length, carbon cloth [b]	0.18	mm
L_{cl}	Length, Pt/C catalyst layer [b]	0.032	mm
pH_0	pH in bulk liquid	7.08	\
P_0	Gas pressure[b]	1.01×10^5	Pa
$q_{max.AcH}$	Maximum specific rate of acetate utilization[e]	1.00×10^{-4}	(mg Ac)/(mg HAB·s)
$q_{max.Acsus}$	Maximum specific rate of acetate utilization	1.00×10^{-4}	(mg Ac)/(mg SUS·s)
R	Gas constant	8.314	J/mol·K

Table 6.1. Continued.

Name	Description	Values	Unit
$q_{max.AcA}$	Maximum specific rate of oxygen utilization, autotrophic biomass	2.00×10^{-5}	(mg O_2)/(mg AAB·s)
$S_{cathode}$	Cathode's cross sectional area in MFC[b]	7.07×10^{-4}	m^2
T	Temperature	303.15	K
X_{abio}	Concentration in anodic biofilm	24.0	g/L
X_{cbio}	Concentration in cathodic biofilm	25.0	g/L
X_{sus}	Suspended biomass concentration in liquid	0.05	g/L
ε_{bio}	Porosity, biofilm	0.95	\
ε_{cc}	Porosity, carbon cloth [b]	0.75	\
ε_{cl}	Porosity, Pt/C catalyst layer [b]	0.30	\
η_K	Cathode half-max overpotential	240.028	mV
ρ_{bl}	Density, bulk liquid [b]	1.05	g/cm^3
ρ_{bio}	Density, bacteria	1.54	g/cm^3
σ	Mass fraction of HAB in biofilm	0.85	\
σ_{abio}	Conductivity, anode biofilm	0.02	S/m
σ_{bl}	Conductivity, bulk liquid [b]	0.755	S/m
σ_{cbio}	Conductivity, Pt/C catalyst layer	0.05	S/m
σ_{cc}	Conductivity, carbon cloth	1.00×10^{5}	S/m
σ_{cl}	Conductivity, Pt/C catalyst layer	1.00×10^{3}	S/m

Table 6.1. Continued.

Values for other model parameters were assumed based on common practical experience.

a is from experimental data.

b is from Reference [72].

c is from Reference [86].

d is from Reference [73].

e is from Reference [37].

f is from Reference [87].

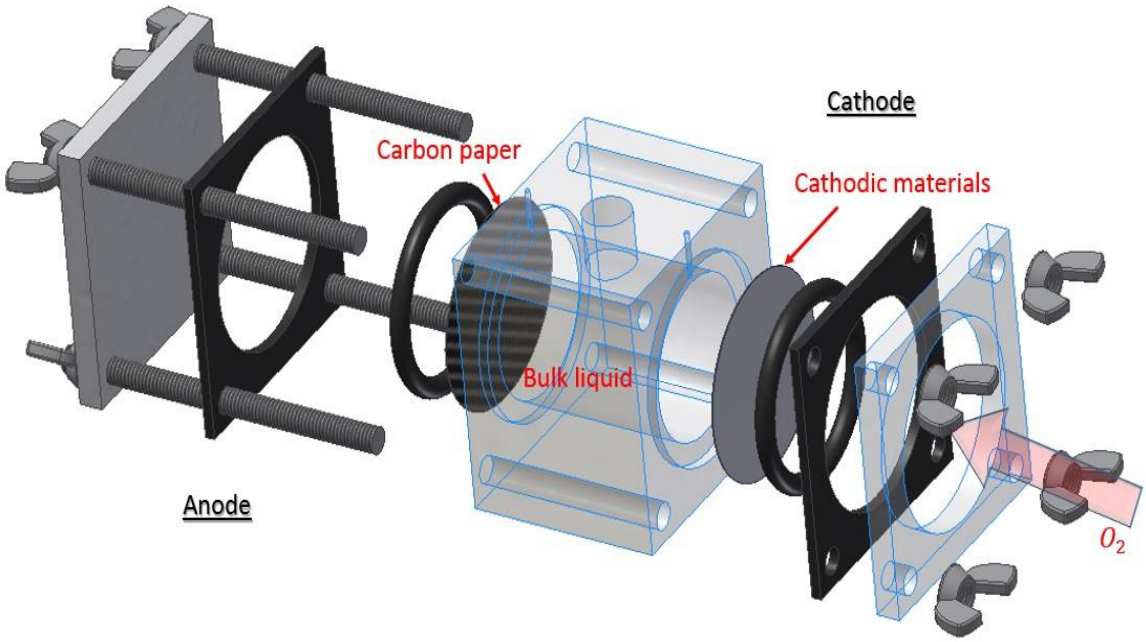

Figure 6.1 Structure of a single chamber air-cathode MFC reactor.

paper, shown in Figure 6.2. The PTFE layer is hydrophobic material, and it is assumed that only gas phase exits in the interspace of PTFE layer. In the full cell model, the simulation for this domain is neglected to simplify the calculation. The amount of the dissolved oxygen is calculated according to Henry's law. Also to improve the computational accuracy, two boundary diffusion layers were added into the model separately approached to the anodic biofilm and the cathodic biofilm. The boundary diffusion layers are still bulk liquid. Figure 6.2 also illustrates some initial conditions of the main substance we considered in the full cell model.

The mass transport Nernst–Planck equation for the substance is shown in the Eqn. (6.1).

$$\frac{\partial c_i}{\partial t} = -\nabla\left(F_{diff} + F_{mig}\right) + r_i \tag{6.1}$$

The F_{diff} is the diffusion flux:

$$F_{diff} = -D_i \frac{\partial c_i}{\partial x} \tag{6.2}$$

The F_{mig} is the electric migration flux [36]:

$$F_{mig} = -\frac{z_i F}{RT} D_i \frac{\partial V}{\partial x} \tag{6.3}$$

where i is the substance species, c_i is the concentration, D_i is the effective diffusion coefficient, z_i is the charge of the ion, V is the local electric potential and r_i is the reaction rate. The reaction rate is the bioelectrochemical reactions in anodic biofilm and cathodic biofilm. In this model, it was assumed that the metabolism of ARB was the only biological reaction in the anodic biofilm. The

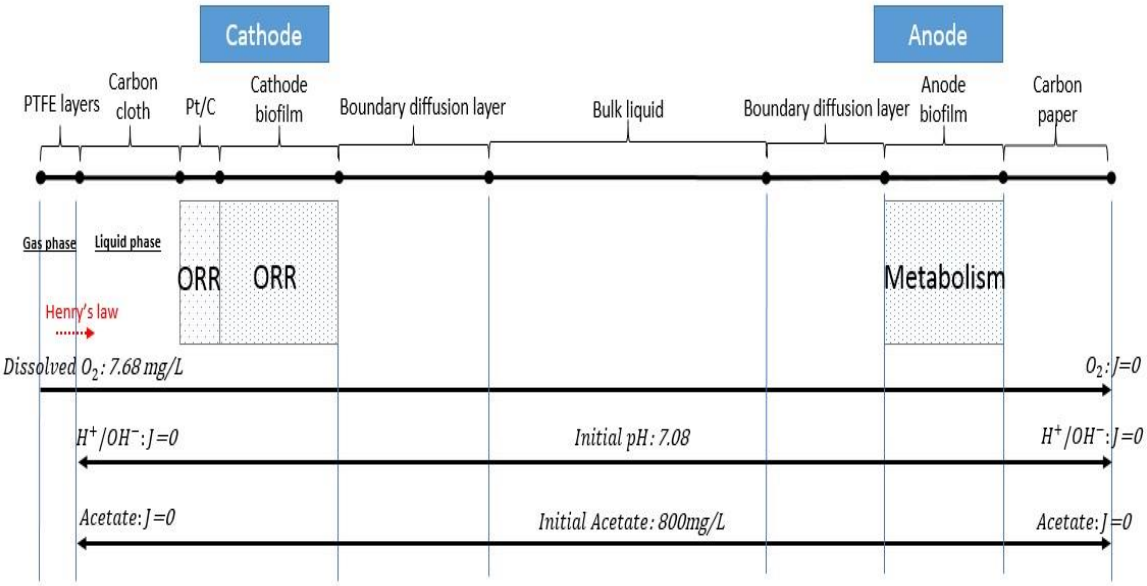

Figure 6.2 Schematic diagram for the full cell system domains in MFC.

ARB transfer the electrons from reduced acetate to the electrode – carbon paper. The movement of the electrons causes the local potential distribution over the anodic biofilm. Meanwhile, the metabolism is also affected by the acetate concentration supplied for local bacteria. The ARB reaction rate is related to the local overpotential and local electron source (acetate), and the Monod-Nernst equation offers a connection for ARB metabolism connections [10], shown in the Eqn. (6.4), this equation is also validated by the kinetic experiments [88].

$$r_{Ac,ARB} = -q_{Ac,ARBmax} X_{ARB} \left(\frac{c_{Ac}}{c_{Ac}+K_{Ac}}\right)\left(\frac{1}{1+\exp(-\frac{F}{RT}\eta_{act,A}+\frac{F}{RT}\eta_{K,A})}\right) \quad (6.4)$$

where $r_{Ac,ARB}$ is ARB acetate reaction rate (mg/L·s), $q_{Ac,ARBmax}$ is ARB maximum specific rate of acetate consumption (mg Ac/mg ARB·s), X_{ARB} is the ARB concentration (mg/L), c_{Ac} is local acetate concentration (mg/L), $\eta_{act,A}$ is the anodic activation overpotential (V), $\eta_{K,A}$ is the half-maximum activation overpotential (V) [10], F is the Faraday constant, T is the temperature, and R is the ideal gas constant. Other participate substances in reaction were calculated based on the stoichiometric numbers in the reactions.

On the other hand, the same as the ORR which has been stated in the Chapter V: the ORR in cathode is in both Pt/C catalyst layer and cathodic biofilm. In the catalyst layer, the oxygen is the electron acceptor and OH^- is generated. While there are different cultures of biomass in the cathodic biofilm. This model simplified the biomass into two groups: autotrophic aerobic biomass (AAB), and heterotrophic aerobic biomass (HAB). The electrons from the out circuit also distribute in both catalyst layer and biofilm layer. The porous catalyst structure is

the same as it is in the traditional PEM fuel cell, therefore the reaction rate calculation in catalyst layer is described by a simplified Bulter-Volmer expression in Eqn. (6.5) [89].

$$r_{O_2,cl} = -\frac{1}{4F}\left[i_{c,0}\frac{c_{O2}}{c^*_{O2}}\exp\left(-\frac{\beta F}{RT}\eta_{act,C}\right)\right]M_{O_2}\delta_{cl} \quad (6.5)$$

where $r_{O2,cl}$ is oxygen reaction rate in the catalyst layer (mg/L·s), $i_{c,0}$ is the exchange current density in cathode (A/m^2), c^*_{O2} is the saturation concentration of oxygen (g/L), β is the symmetric factor, M_{O2} is oxygen molar mass (mg/mol) in catalyst layer, and δ_{cl} is the catalyst specific area (m^{-1}). In the biofilm layer, this model applied the Monod-Nernst equation for cathodic calculation. The Eqn. (6.6) is the AAB reaction rate calculation in cathodic biofilm, and the Eqn. (6.7) is the HAB reaction rate calculation in cathodic biofilm.

$$r_{O_2,AAB} = -q_{O_2,\,AABmax}X_{AAB}\frac{c_{O_2}}{K_{O_2,AAB}+c_{O_2}}\frac{1}{1+\exp\left(-\frac{F}{RT}\eta_{act,C}+\frac{F}{RT}\eta_{K,C}\right)} \quad (6.6)$$

$$r_{Ac,HAB} = -q_{Ac,\,HABmax}X_{HAB}\frac{c_{O_2}}{K_{O_2,HAB}+c_{O_2}}\frac{c_{Ac}}{K_{Ac,HAB}+c_{Ac}}\frac{1}{1+\exp\left(-\frac{F}{RT}\eta_{act,C}+\frac{F}{RT}\eta_{K,C}\right)} \quad (6.7)$$

where $r_{O2,AAB}$ is AAB oxygen reaction rate (mg/L·s), $q_{O2,AABmax}$ is maximum specific rate of oxygen consumption (mg O_2/mg AAB·s) for AAB, X_{AAB} is the AAB concentration (mg/L), K_{O2} is the half-max-rate oxygen concentration (mg/L), η_{act} is the cathodic activation overpotential (V), $\eta_{K,C}$ is the cathodic half-max overpotential (V), $r_{Ac,HAB}$ is HAB acetate reaction rate (mg/L·s), $q_{Ac,HABmax}$ is maximum specific rate of acetate consumption (mg Ac/mg HAB·s) for HAB, X_{HAB} is the HAB concentration (mg/L).

6.2.2 Current generation

Generally the overpotential analysis of MFC is the same as the traditional fuel cells. The overpotential can be divided into three types: activation overpotential η_{act}, ohmic overpotential η_{ohm} and concentration overpotential η_{con} in both cathode and anode [37]. The total overpotential η_{total} is shown in the Eqn. (6.8). The overpotential balance is shown in the Eqn. (6.9).

$$\eta_{total} = \eta_{act} + \eta_{con} + \eta_{ohm} \tag{6.8}$$

$$V_{cell} = \left(E_C^0 - |\eta_{C,act}| - |\eta_{C,con}|\right) - \left(E_A^0 + |\eta_{A,act}| + |\eta_{A,con}|\right) - |\eta_{ohm}| \tag{6.9}$$

In this model, it was assumed that the internal resistance was comprised of the anodic resistance R_A, cathodic resistance R_C, and electrolytic resistance in bulk liquid R_{BL} are shown in the Eqn. (6.10) and the Eqn. (6.11).

$$|\eta_{ohm}| = |\eta_{A,ohm}| + |\eta_{C,ohm}| + |\eta_{BL,ohm}| \tag{6.10}$$

$$|\eta_{ohm}| = IR_A + IR_C + IR_{BL} \tag{6.11}$$

The open circuit voltages v.s. Ag/AgCl for anode and cathode in this model have been measured from the experiments: the cathodic equilibrium voltage E_c^0 is -500.46 mV, the anodic equilibrium voltage E_A^0 is 273.73 mV. Also the cell voltage was measured based on the loaded external resistance and it is calculated by the Eqn. (6.12).

$$V_{cell} = IR_{ext} \tag{6.12}$$

In the simulations, the biofilm in both electrodes and the catalyst layer were assumed to be conductive and the electron conduction through the conductive

materials was described to be based on the electron balance and Ohm's law [10].

$$0 = \sigma \frac{\partial^2 \eta_{act}}{\partial x^2} + F\gamma r \tag{6.13}$$

where σ is the conductivity of local domain (S/m), η_{act} is the local activation overpotential (V), γ is the electron equivalence (mol e^-/mol), r is the reaction rate of substance (mol/L·s), the species is acetate for ARB in anodic biofilm and AAB in cathodic biofilm, is oxygen for the ORR in cathodic catalyst layer. This steady state equation is calculated based on two boundary conditions [10]:

$$\eta_{act}|_{x=0} = \eta_{ele,act} \tag{6.14}$$

$$\left.\frac{\partial \eta_{act}}{\partial x}\right|_{x=L} = 0 \tag{6.15}$$

where $\eta_{ele,act}$ is the activation overpotential at the electrode, and the other condition is boundary between the conductive material and electrolyte: On the anode side, it is the boundary between anodic biofilm between boundary diffusion layer; On the cathode side, it is the boundary between cathodic biofilm between boundary diffusion layer.

6.2.3 Buffer liquid system

The buffer is a common way to optimize the reactor liquid which maintains a feasible pH environment for the ARB to generate electrons and reduces the concentration overpotentials. This PhD research did not only build a steady state model for the MFC whole system including anode, cathode and electrolyte, but also gave the simulation analysis to the buffer system, e.g. NH_4Cl, $NaHCO_3$, PBS

(Phosphate Buffered Saline) and their effects to the pH, mass transport and power output of the MFC system. The relation between pH and metabolism, ARB growth is still hard to be quantitatively analyzed till now [33], thus the model only simulated the pH influence to the MFC system potentials. The equation for the concentration overpotential is shown in Eqn. (6.16).

$$\eta_{con} = \frac{RT}{nF} \ln\left(\frac{c_{H^+/OH^-}}{c^0_{H^+/OH^-}}\right) \tag{6.16}$$

The concentration overpotential in anode is decided by H^+ concentration, and the concentration overpotential in cathode is decided by OH^- concentration. The local pH in bulk liquid is assumed to be derived by the concentration of protons in our study. In the Eqn. (6.16), $c_{H+/OH-}$ is local H^+/OH^- concentration, $c^0_{H+/OH-}$ is the initial H^+/OH^- concentration in bulk liquid. The initial pH in the simulation is assumed to be 7.08. Table 6.2 lists the buffer chemical dissociation equations which were applied is this model.

The pK_a is the acid dissociation logarithmic constant for each equation in Table 6.2. In our study, an algorithm was established for the calculation of the buffer chemical reactions in domains in MFC system, the algorithm and model equations with a flow diagram are shown in Figure 6.3. Based on the previous Eqn. (6.7-6.10), the overpotentials were calculated. In the Eqn. (6.3-6.6), r_{Ac}, r_{O2} and r_H are obtained in every domain in the full cell model system. The Eqn. (6.2) gives the mass transport calculations for substances and the substances concentrations are updated as well as the local pH in every control volume.

Table 6.2. Buffer chemical reactions in the full cell steady state model.

Buffer name	Equation	pK_a
H_2O	$H_2O \leftrightarrow OH^- + H^+$	14
NH_4Cl	$NH_4^+ \leftrightarrow NH_3 + H^+$	9.25 [90]
$NaHCO_3$	$H_2CO_3 \leftrightarrow HCO_3^- + H^+$	6.37 [91]
	$HCO_3^- \leftrightarrow CO_3^{2-} + H^+$	10.3 [91]
PBS	$H_3PO_4 \leftrightarrow H_2PO_4^- + H^+$	2.12 [92]
	$H_2PO_4^- \leftrightarrow HPO_4^{2-} + H^+$	7.21 [92]
	$HPO_4^{2-} \leftrightarrow PO_4^{3-} + H^+$	12.32 [92]

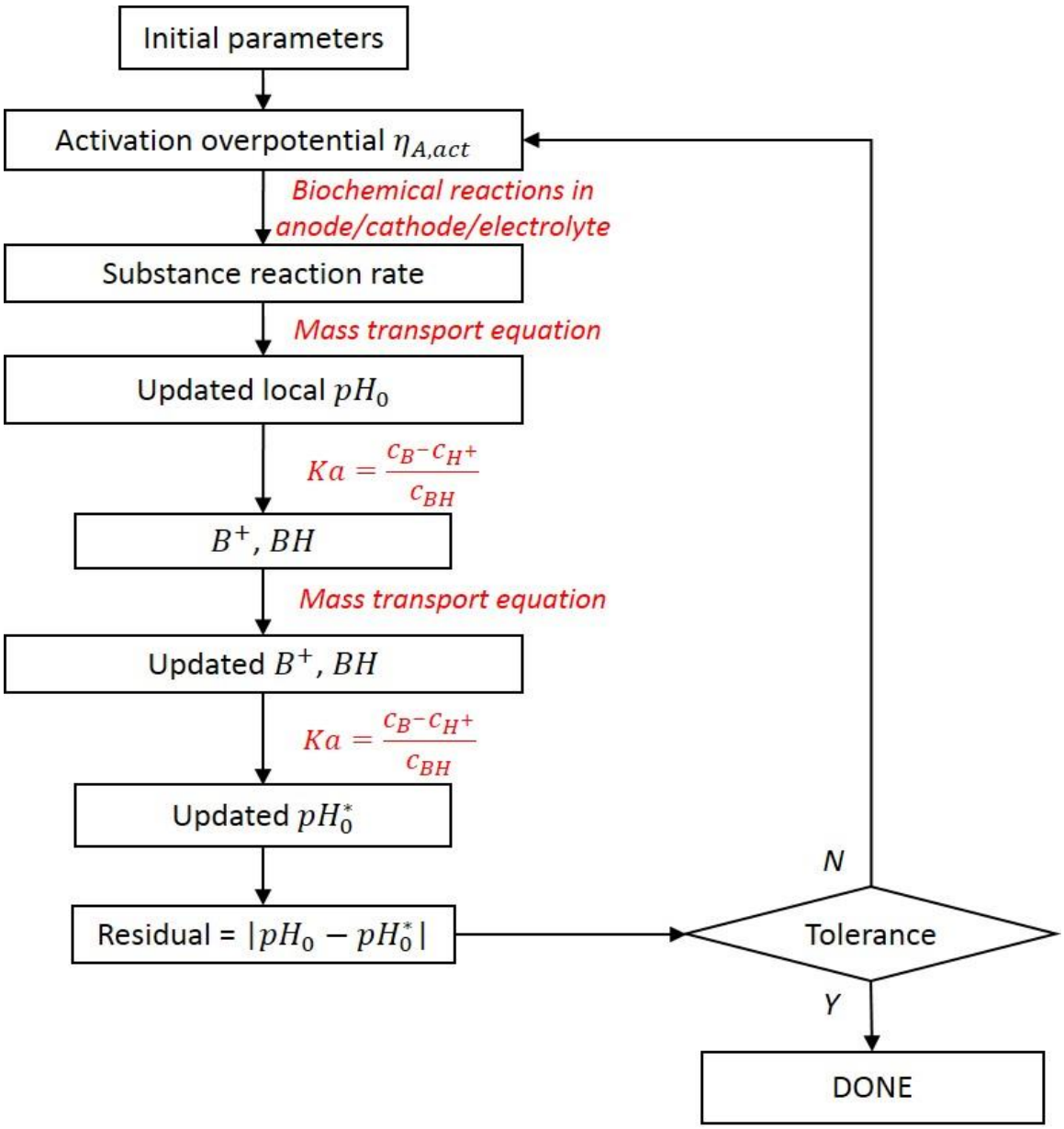

Figure 6.3 Flow diagram of the algorithm for buffer chemical reaction and pH in MFC system modeling.

Because of the change of pH, the original buffer chemical reaction balance is broken and the new balance needs to be reach. The balance equation for buffer chemicals can be represented by the Eqn. (6.17).

$$K_a = \frac{c_B - c_{H^+}}{c_{BH}} \tag{6.17}$$

$$BH \leftrightarrow B^+ + H^+ \tag{6.18}$$

where K_a is the dissociation constant which is a quantitative measure of the strength of an acid in chemical solution. c_{BH} and c_{B^-} represent the concentrations for buffer chemicals in the equilibrium. This simulation assumed the reaction rates in the dissociation equilibrium (Eqn. (6.18)) are much faster than the reaction rates in mass transport equation [33]. The new local concentrations for B^+ and BH are measured from the Eqn. (6.17). Then the change of buffer everywhere needs the mass transport equation to update the buffer concentration, new balance is built and new pH are obtained based on the Eqn. (6.17) shown in the Figure 6.3. The residual from two different pH values are calculated and is compared with tolerance to decide the next computational step.

Picioreanu et al. [33] also presented us the method to simulate the pH and buffer chemical solution in the half-cell MFC performance. It assumed that the reaction of the dissociation equilibrium is calculated based on the Eqn. (6.19).

$$r_{a,BH} = k_{BH}\left(c_{BH} - \frac{c_B - c_{H^+}}{K_a}\right) \tag{6.19}$$

where the k_{BH} is the rate constant for the dissociation equilibrium (s^{-1}) and it is assumed in the simulation. In this study, both our buffer algorithm and the Picioreanu et al. algorithm (k_{BH} is assumed to be 10^{-10} s^{-1} in the calculation) are

applied into the full cell model to calculate the pH profile with buffer chemicals. The simulation results applied with these two algorithms are compared and the maximum error is less than 0.8 %. Therefore this algorithm is acceptable to apply for the full cell buffer model system.

6.3 Full Cell Model Analysis

With the full cell steady state model, three modeling cases were simulated: 1). Experiment results simulation and concentration overpotential impact analysis; 2). Different buffer chemical liquid are compared; 3). Different concentrations of buffer chemical liquid are compared. In the steady state simulation, the external resistance was changed to be 50Ω, 75Ω, 130Ω, 170Ω, 210Ω, 250Ω, 500Ω, 750Ω, 1000Ω, 2000Ω, 4000Ω in every simulation. The electrochemical (polarization curves, power density, overpotentials et al.), substances distribution (oxygen, acetate, buffer chemicals et al.), and pH profiles were simulated and analyzed from the full cell steady state model.

6.3.1 Numerical evaluation for the electric migration in the mass transport

The chemical mass transport in the microbial fuel cell is decided by the convection, diffusion and electric migration. There were no stirring and the flow of the fluid was small in the single chamber MFC reactor, thus the convection was neglected in the simulation. This model was adopted to discuss the influence by the electric migration. Two groups of simulation have been conducted, the governing equation for mass transport in the first group of simulation contained

both diffusion and electric migration terms, while the second group of simulation only included the diffusion term, as it shows in Eqn. (6.20).

$$\frac{\partial c_i}{\partial t} = D_i \frac{\partial^2 c_i}{\partial x^2} + r_i \tag{6.20}$$

where i is the substance species, c_i is the concentration, D_i is the effective diffusion coefficient, and r_i is the reaction rate.

As it shows in Figure 6.4, the electric migration indeed has influence to the power production in the mass transport equation. Considering the electric migration flux in the mass transport in bulk liquid as well as in the anodic/cathodic layers, the power production is increased by 7.4 % compared with the simulation results that only diffusion is considered. Since the electric migration term is a minor influence for the mass transport, it is reasonable to neglect this term [36]. In the simulations for the full cell model, only the buffer amount comparison in 6.3.4 section considered both diffusion and electric migration since the buffer concentration affects the electric migration and electric conductivity of the bulk liquid.

6.3.2 Experiment with buffer simulation

In this case, the experiment data were fitted by the simulation. The measured parameters, (including the buffer liquid parameters) for simulation were the same as they were in the experiment. The buffer liquid contains 17.77 mM of NaH_2PO_4/H_2O, 32.23 mM of Na_2HPO_4, 1.74 mM of KCl and 5.79 mM of

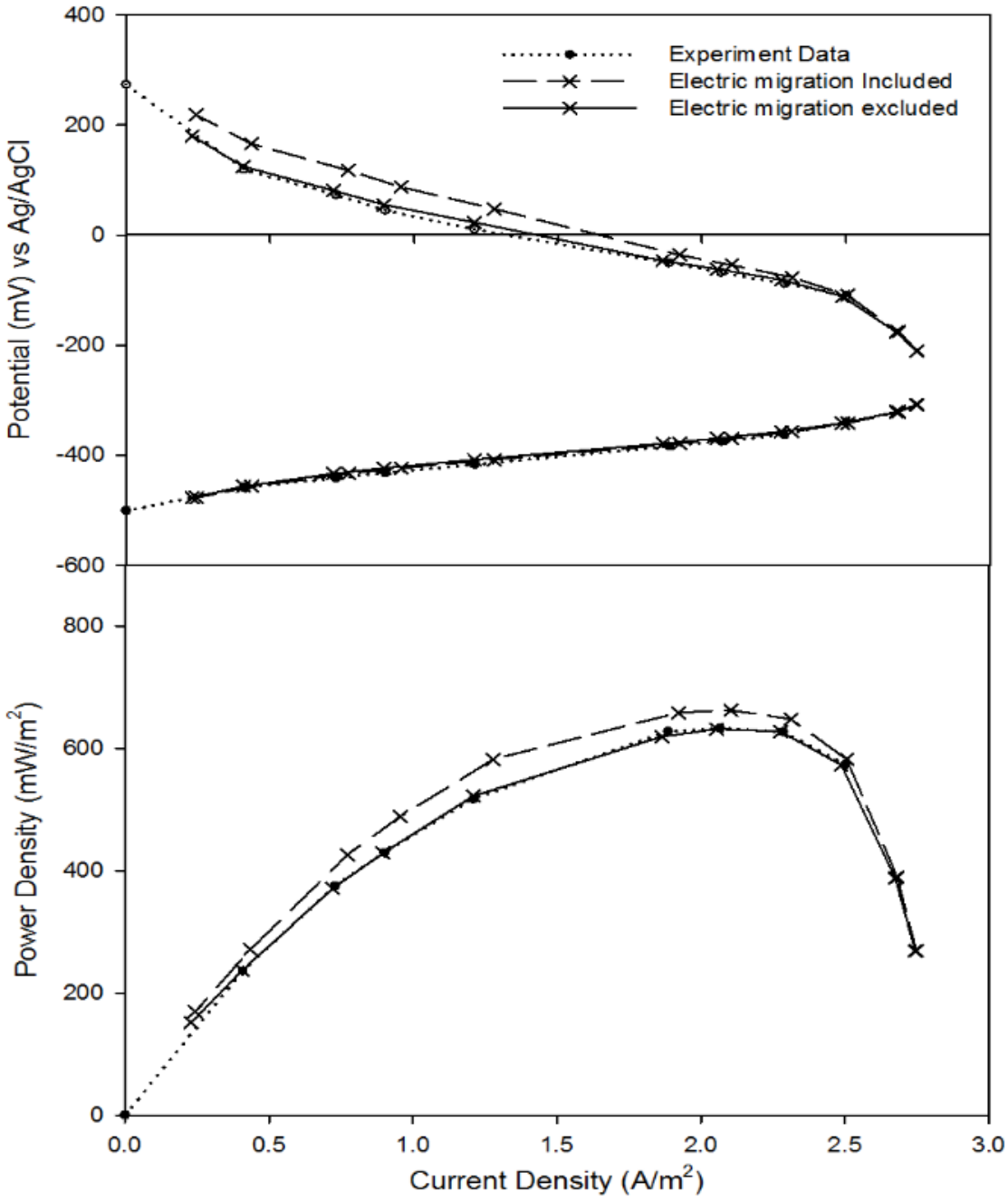

Figure 6.4 The electric migration term influence to the power production in MFC.

NH_4Cl. The case without any buffer was simulated and presented the effects by buffer to improve the current density and power output. Besides, the ideal situation (the H^+/OH^- concentration overpotential is completely eliminated) was also revealed here in the simulation to reflect the concentration overpotential influence to the MFC system.

The simulation gave us a direct perspective to exam the impact of the buffer system in the bulk liquid for MFC reactor. Figure 6.5 presents us the polarization and power density curves to compare the buffer impacts to the MFC energy production. The “Experiment Data” curve is the data from the lab, it is the reference to check the simulation results. “50 mM Buffer” is assumed that 50 Mm buffer liquid is added into the bulk liquid and regulates the pH and the reactions for the whole MFC system including the anodic/cathodic side and bulk liquid part. Figure 6.5 shows that the “50 mM Buffer” has very good fitting compared with the “Experiment Data”. “No Buffer” is the simulation result that no buffer is added into the bulk liquid to regulate the pH in reactor. Less power is produced by the “No Buffer” simulation, the “No Buffer” MFC reactor power production is average 9.80 % lower than the “50 mM Buffer” simulation is. At the same time, more potentials are lost for the cathodic side, the anodic potential changes slightly compared with the “50 mM Buffer” anodic potential curve. Also the “Ideal” situation was simulated, which is assumed that the pH change has no effects to the MFC reactions, the “Ideal” MFC reactor produces average 21.87 % higher power than

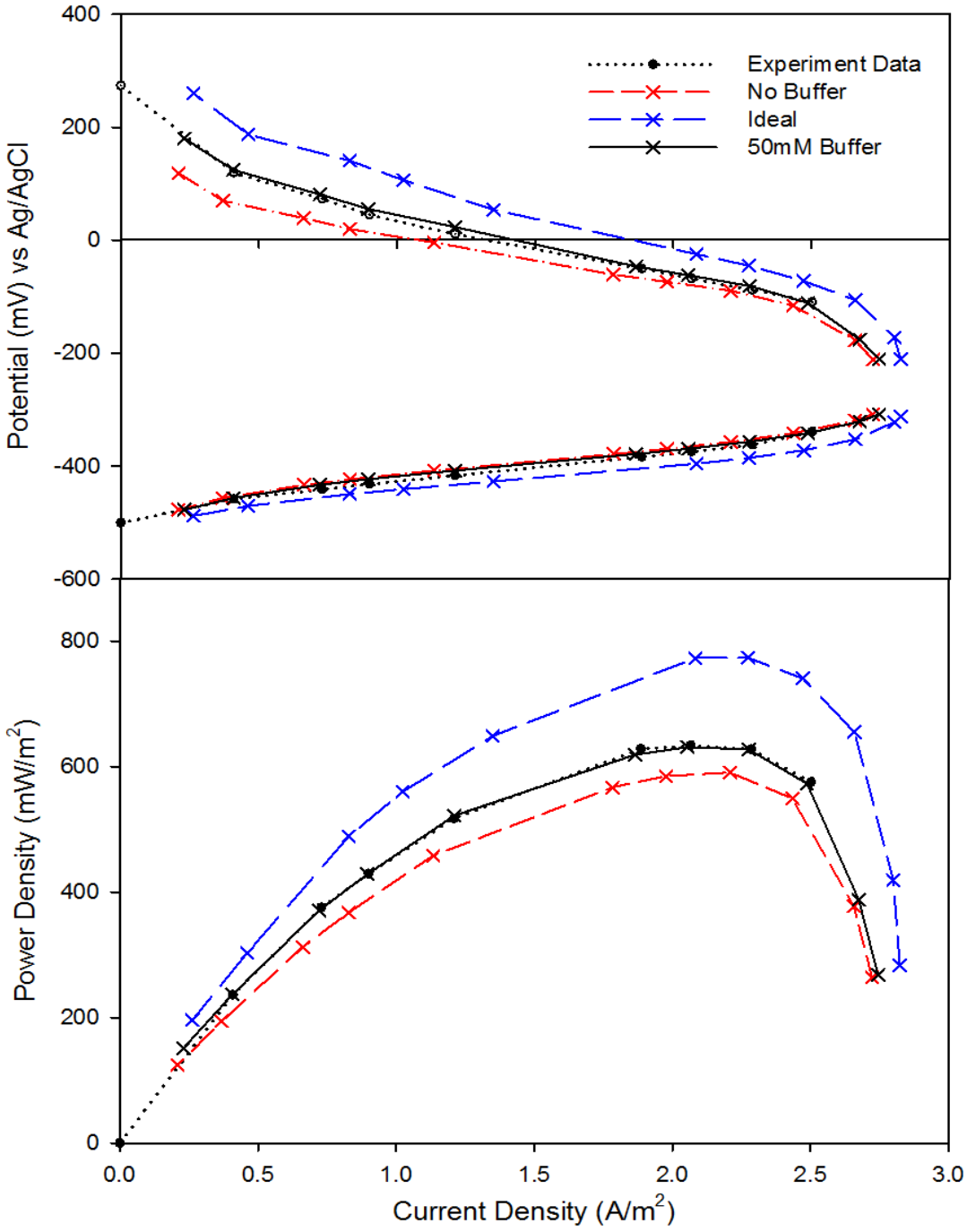

Figure 6.5 Polarization and power density curves comparison.

the “50 mM Buffer” simulation does. The overpotentials in both anodic and cathodic sides are obviously reduced in “Ideal” simulation.

The simulation also gave the pH distribution with different external resistance and different current density, shown in Figure 6.6. The cathodic higher pH is from the production of OH^- and the anodic lower pH is because of the production of H^+. The bulk liquid initial pH is set to be 7.08, while the simulated results show in Figure 6.6 that pH < 7.08 distributes a broader range in bulk liquid part and pH < 7.08 locates the portion which is close to cathode side. This is because of the diffusion coefficient of protons is much larger than OH^-‘s, which leads to a faster diffusion of protons in the bulk liquid, therefore the bulk liquid in reactor is in slightly acidic condition.

Figure 6.7 gives the pH change over different current density for both “No Buffer” and “50 mM Buffer”. Since the simulation of “Ideal” ignored the pH influence, the profile of pH “Ideal” isn’t presented in Figure 6.7. The buffer shown in Figure 6.7 gave an obvious impact to the pH in both anodic and cathodic sides especially for the anodic pH improvement.

According to Eqn. (6.16), it is known that the concentration of H^+/OH^- affects the mass transport overpotential in microbial fuel cell. Therefor the buffer solution is added to help to reduce the concentration overpotential to increase the power production. However, the simulation results presented the truth that the buffer solution has limited capacity to increase the power for MFC single

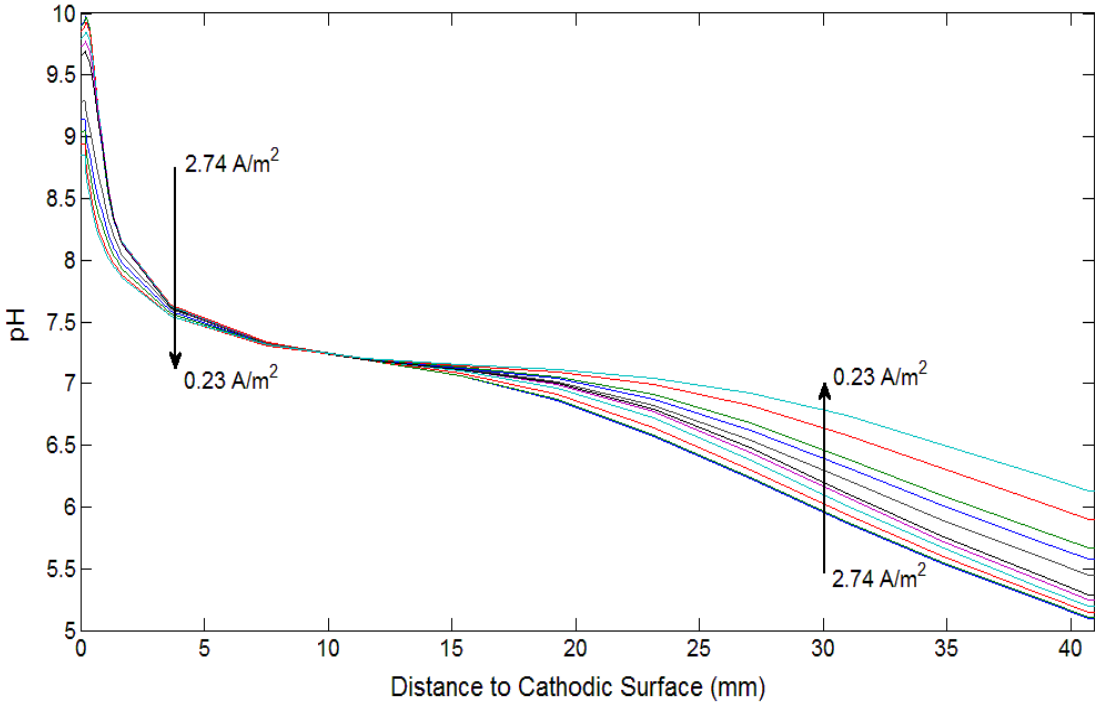

Figure 6.6 pH distribution for different current situation in “50 mM Buffer” simulation.

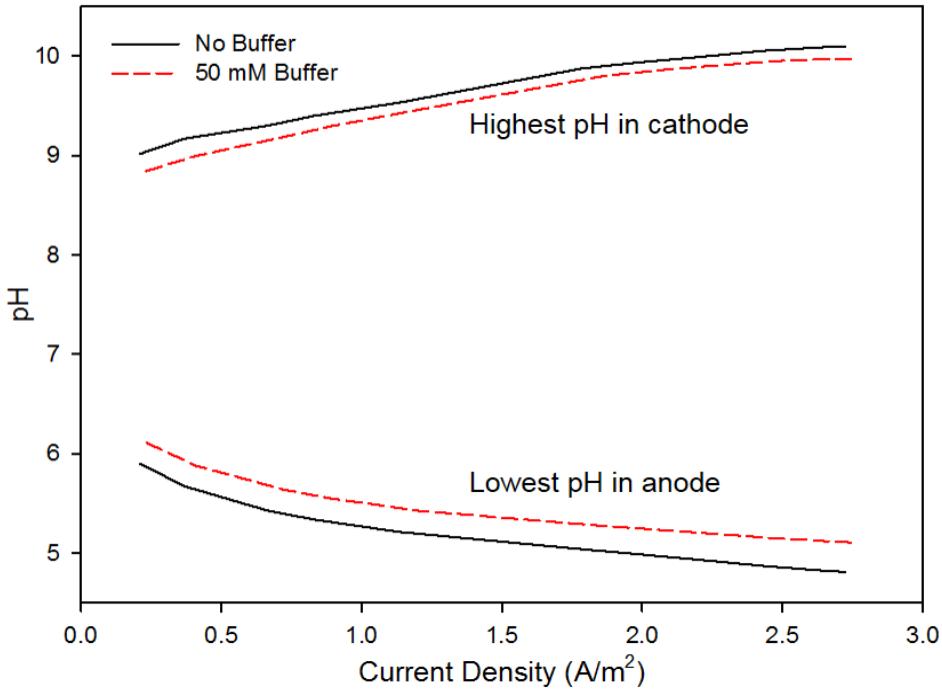

Figure 6.7 pH comparison for “No Buffer” and “50 mM Buffer”.

chamber reactor. If the “Ideal” simulation is the best simulation that the influence from the concentration overpotential from pH is totally eliminated, it can be inferred that the “50 mM Buffer” contributes to eliminate 31.41 % pH influence. However the buffer cannot 100 % remove the pH influence, the anodic/cathodic would always have H^+/OH^- concentration changes even though the pH of bulk liquid part can be close to neutral.

6.3.3 Comparison for different buffer solutions

This full cell model dug deeper on the contribution of buffer to the power production by comparing the power generation curves and pH change of different buffer chemicals. Three common buffer solutions were simulated: “50 mM PBS” is the simulation of MFC reactor with 50 mM phosphate buffered saline as buffer solution, “50 mM $NaHCO_3$” is the simulation of MFC reactor with 50 mM sodium bicarbonate as buffer solution, and “50 mM NH_4Cl” is the simulation of MFC reactor with 50 mM ammonium chloride as buffer solution.

In Figure 6.8 a), the simulation are the polarization and power density curves generated from the MFC reactor with different buffer solutions. The results shows that the 50 mM PBS performance the best in improving the power density, though different buffer solutions is not necessary to lead to obvious difference, especially for the anodic potential changes. Meanwhile, the Figure 6.8 b) reveals the simulation results on lowest/highest pH in MFC. The buffer solutions stop the massive changes of pH environment for both anodic and

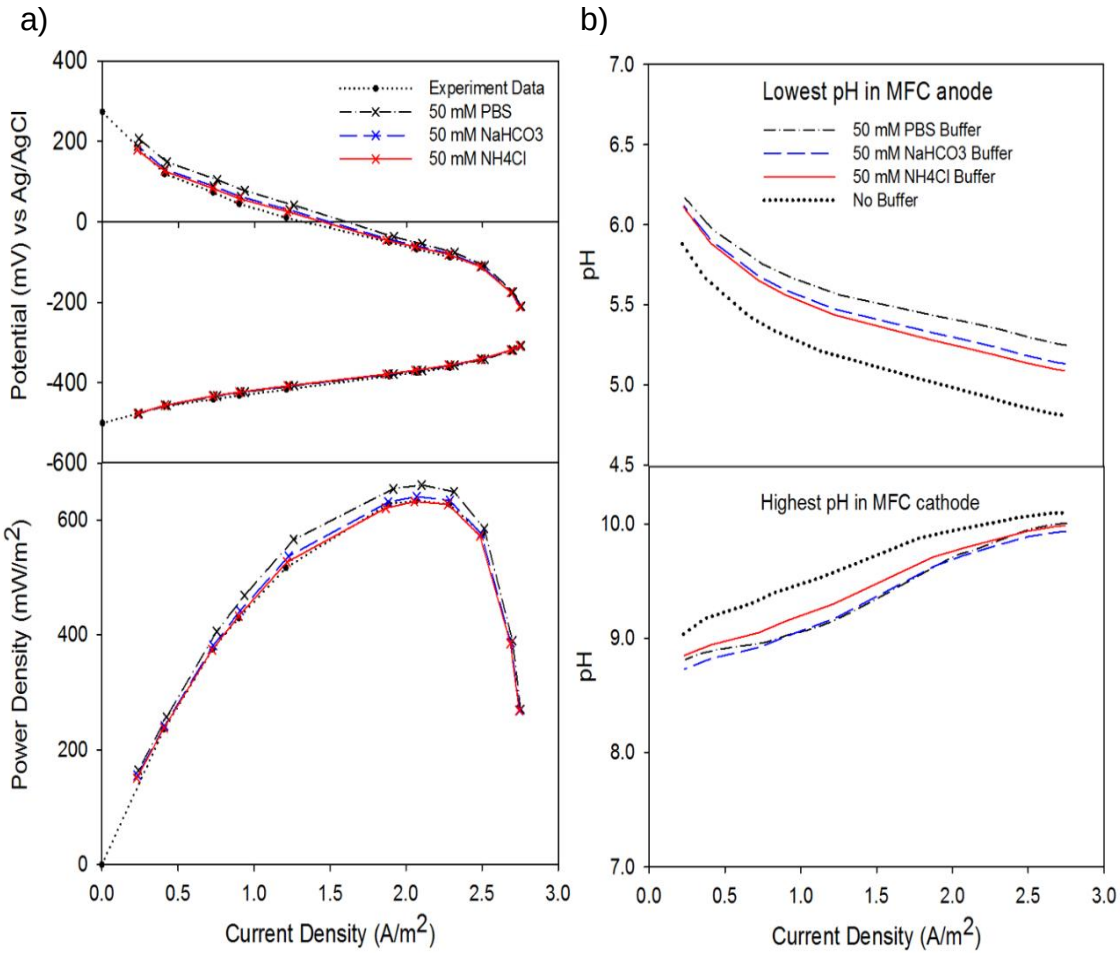

Figure 6.8 Polarization curves and pH profiles for different buffer solutions.

cathodic side compared with no buffer MFC pH simulation. Generally, the 50 mM PBS buffer works most effectively among these three buffer solutions, though capacity of the PBS buffer recedes in cathodic side when the current density is larger. According to the data from Table 6.2, there are three equilibrium reactions (neutralization reactions) for phosphate, there are three types of conjugate bases (PO_4^{3-}/HPO_4^{2-}/$H_2PO_4^-$) and more H^+ can be reacted to conjugate base for same amount moles of buffer solutions. However the smaller diffusion coefficient phosphate limits the transport of the PBS to react when the current density becomes larger. In this model, the diffusion coefficient of PO_4^{3-} is a magnitude smaller than the diffusion coefficient for both NH_4^+ and HCO_3^-. Particularly in the cathodic layers where the porosity aggravates the difficulty for the mass transport and equilibrium reaction, less amount of H^+ is produced to neutralize the pH in cathode.

As presented previously, the buffer conduces to reduce the concentration overpotential in addition to create a friendly pH environment for microbes. The benefit of the modeling is that it supplies details on the concentration losses. Figure 6.9 presents the total concentration overpotentials for the MFC whole system (including both cathode and anode). The buffer chemical equilibrium balances obviously decrease the concentration overpotential compared with the “No Buffer” simulation, while the buffer chemicals limitedly change the overall potential losses since the concentration overpotential takes a small part in the total overpotential.

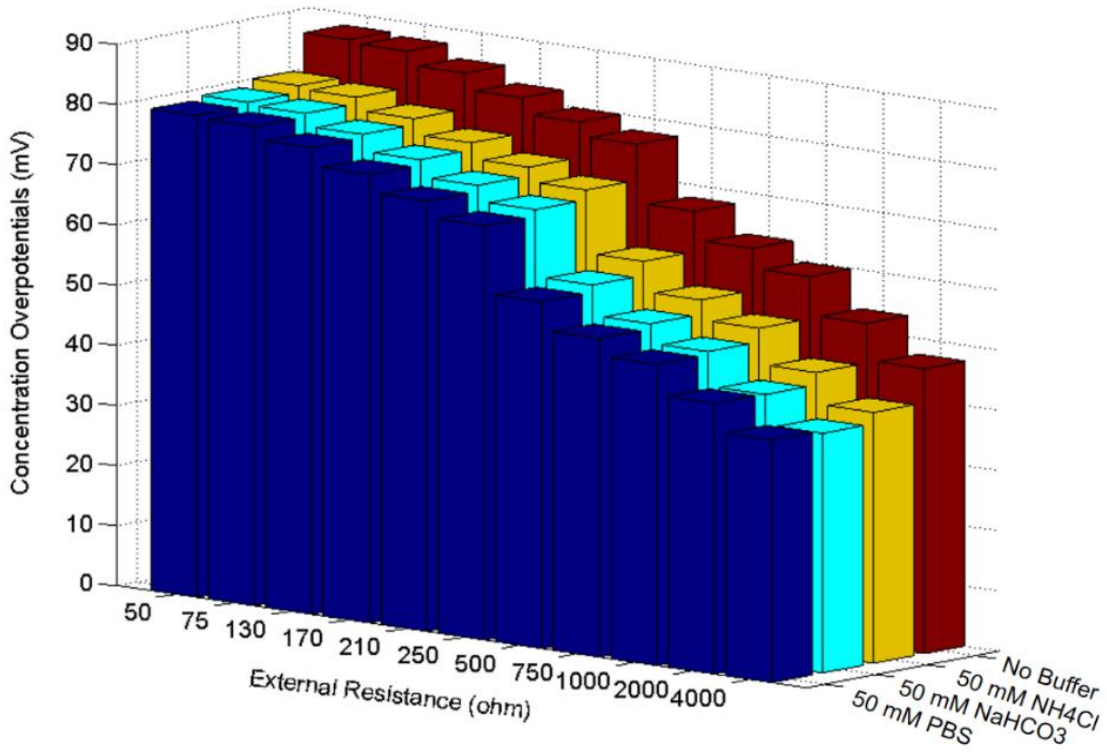

Figure 6.9 The concentration overpotentials from different buffer systems comparisons.

Figure 6.10 gives the comparisons for the buffer chemicals in anode and cathode respectively. The bar chart in Figure 6.10 a) tells the information we already know that the PBS works better to reduce the concentration potential losses, followed by $NaHCO_3$ and then by NH_4Cl. The same trend as it shows for the total concentration potential losses. While in the Figure 6.10 b), the phosphate buffer works worst when the external resistance is smaller (current density is higher), the phosphate buffer works the best when the external resistance is larger (current density is lower). This phenomenon echoed the PBS simulation results shown in Figure 6.8. The phosphate chemicals are larger molecules and smaller diffusion coefficient compared with the $NaHCO_3$ and NH_4Cl, and the phosphate chemicals are more difficult to transport through the layers in the cathode especially when more phosphate are needed in the higher current density.

6.3.4 Comparison for different amounts of the PBS buffer solution

In previous simulations, the bulk liquid conductivity was assumed to be an unchanged constant no matter how the concentration of the bulk liquid change, that the conductivity of the bulk liquid was neglected for simplifying the modeling work. However, the change of the bulk liquid conductivity is related to the concentration of the bulk liquid and is able to influence the power production of the MFC. This full cell model considered changing the amount of phosphate buffer into the reactor liquid and simulated the full cell system to see the influence by the bulk liquid conductivity.

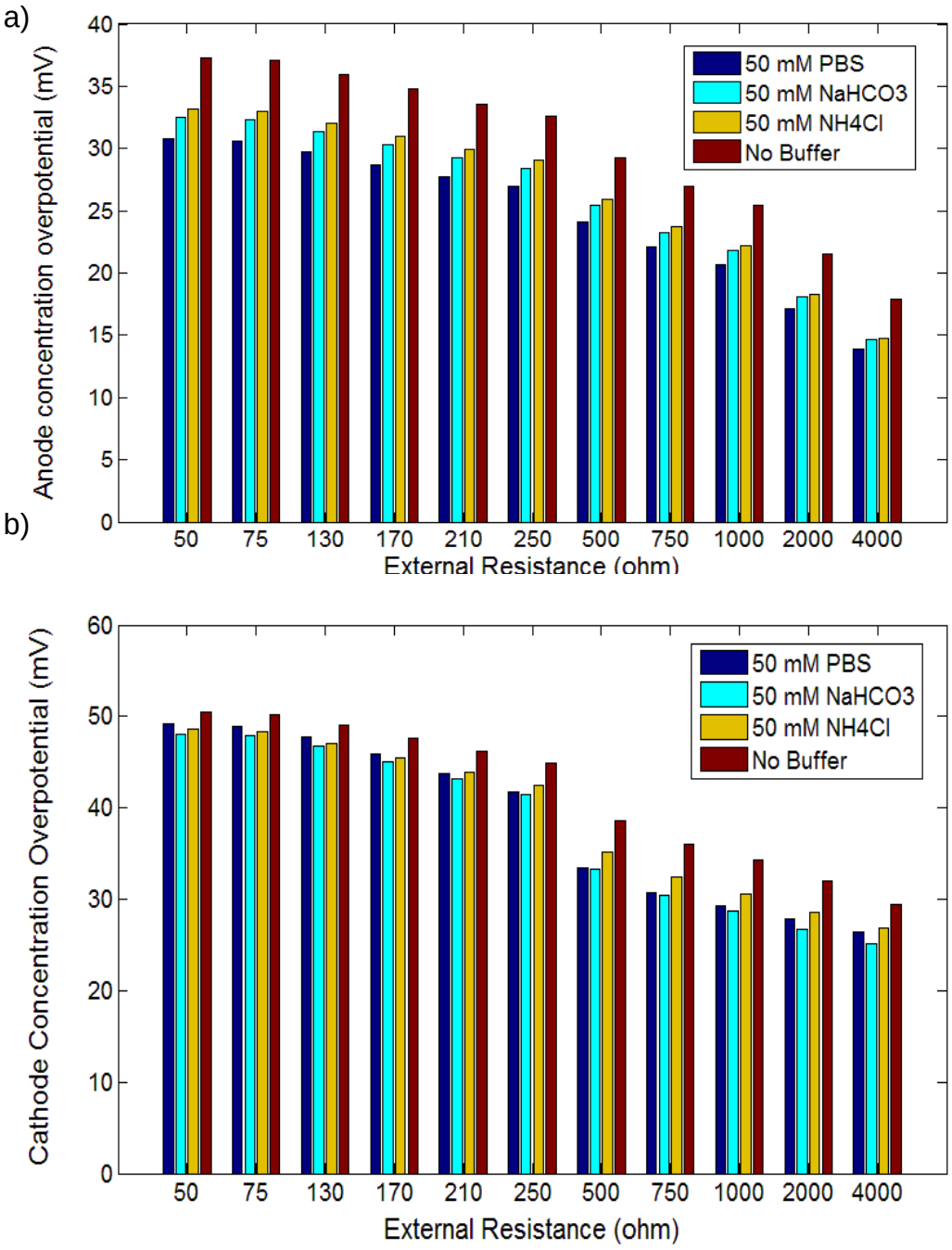

Figure 6.10 Concentration overpotentials comparisons.

50 mM, 100 mM and 200 mM phosphate buffers were simulated. The conductivity of bulk liquid with 50 mM PBS is 5.9 mS/cm [93], the conductivity of bulk liquid with 100 mM PBS is 10.2 mS/cm [93], and the conductivity of bulk liquid with 200 mM PBS is 22.0 mS/cm [94]. Figure 6.11 shows the simulation results comparing different concentration amounts. More amount of the buffer is added into the reactor, better conductive the bulk liquid is, and lower internal resistance the bulk liquid has, thus more power is generated from the reactor. While the PBS costs more than other two buffer solutions, which means it might spend more to improve the power production in a relative small range. Therefore it is not a good idea to add as much PBS into the reactor to improve the pH environment and reduce the internal resistance when the cost is considered for the organics degradation by MFC technology.

6.4 Conclusion

It is presented in this chapter that the simulation and analysis for H^+/OH^- diffusion and the influence from the pH change to the electrochemical reactions, the impact to power density of whole MFC system. The model for single chamber MFC system including anode, bulk liquid and cathode was built to comprehensively analyze the mass transport (diffusion term and electric migration term are included), biological and electrochemical reactions in the whole system. The numerical method was determined for the combinations of anode and cathode which were two relatively independent system in model, and the method was used for the steady state simulation for each external resistance

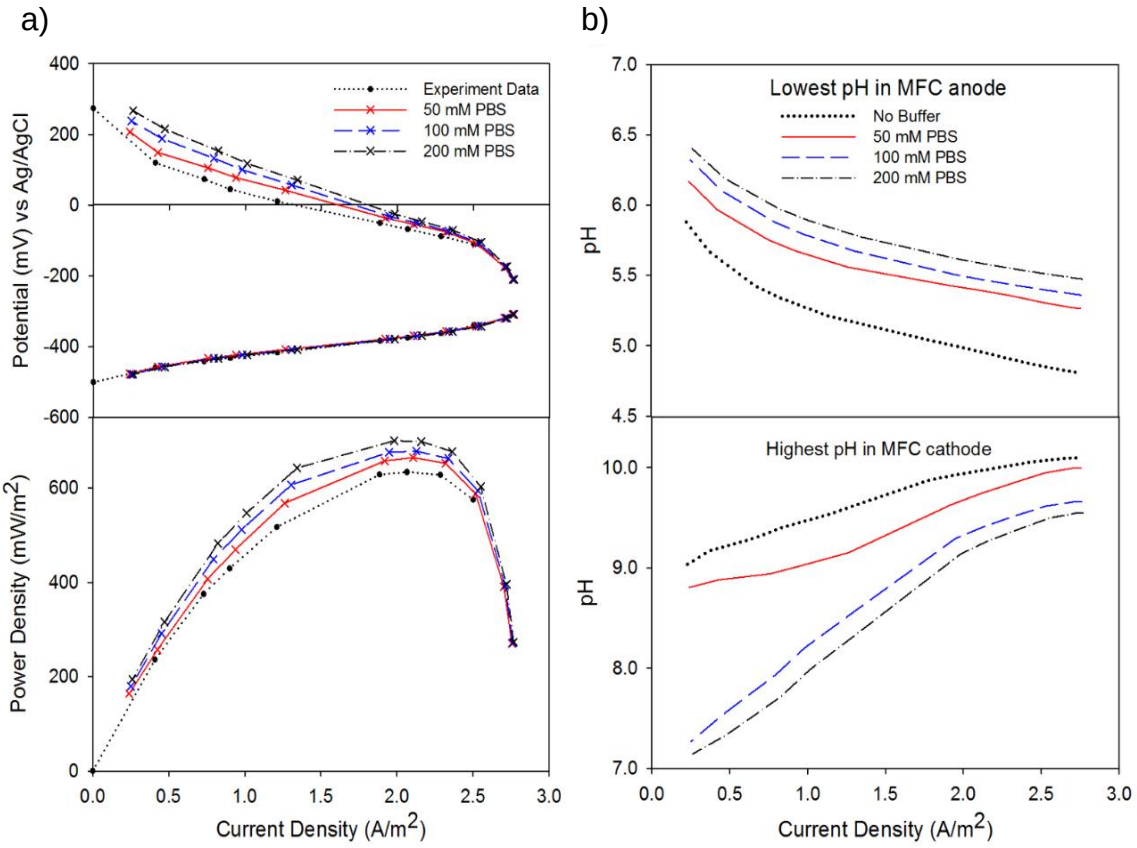

Figure 6.11 Polarization curves and pH profiles for different PBS concentration solutions.

to compare and validate by the experiment data. This model evaluated the electric migration and gave the simulation and analysis that the electric migration has much minor influence to current generation in the single chamber MFC.

This full cell model considered the pH impacts to the overpotential, and neglected the pH influence to the biomass growth in bulk liquid. The buffer solution and its role was considered and simulated in the steady state full cell model. Three buffer solutions (PBS, $NaHCO_3$, NH_4Cl) were simulated and compared in this this model. The PBS buffer solution with three equilibrium equations is more capable in the pH neutralization, while the large diffusion coefficient of the chemicals in PBS prevents the reactions when the current density becomes larger. Also different amounts of buffer solution in the model were compared, the power production influence by the buffer's conductivity were estimated. It is revealed that the larger amount of buffer solution can improve the production of power density from MFC except affecting pH neutralization.

LIST OF REFERENCES

1. EIA, U., *Annual energy review 2011.* US Energy Information Administration, Tech. Rep, 2012.
2. EIA, U., *International energy statistics.* US Energy and Information Administration, Washington, DC [available at http://www. eia. gov/countries/data. cfm], 2011.
3. REN21, P.S., *Renewables 2014: Global Status Report*. 2014: REN21 Secretariat Paris, France.
4. Panwar, N., S. Kaushik, and S. Kothari, *Role of renewable energy sources in environmental protection: a review.* Renewable and Sustainable Energy Reviews, 2011. **15**(3): p. 1513-1524.
5. McCarty, P.L., J. Bae, and J. Kim, *Domestic wastewater treatment as a net energy producer–can this be achieved?* Environmental science & technology, 2011. **45**(17): p. 7100-7106.
6. Potter, M.C., *Electrical effects accompanying the decomposition of organic compounds.* Proceedings of the Royal Society of London. Series B, Containing Papers of a Biological Character, 1911: p. 260-276.
7. Logan, B.E., *Microbial Fuel Cells*. 2008, Hoboken, New Jersey: John Wiley & Sons, Inc. 200.
8. Shi, L., et al., *Respiration of metal (hydr) oxides by Shewanella and Geobacter: a key role for multihaem c-type cytochromes.* Molecular microbiology, 2007. **65**(1): p. 12-20.

9. Parameswaran, P., et al., *Kinetic, electrochemical, and microscopic characterization of the thermophilic, anode-respiring bacterium Thermincola ferriacetica.* Environ Sci Technol, 2013. **47**(9): p. 4934-40.

10. Kato Marcus, A., C.I. Torres, and B.E. Rittmann, *Conduction-based modeling of the biofilm anode of a microbial fuel cell.* Biotechnol Bioeng, 2007. **98**(6): p. 1171-82.

11. Zhang, X.-C. and A. Halme, *Modelling of a microbial fuel cell process.* Biotechnology Letters, 1995. **17**(8): p. 809-814.

12. Kim, B.H., et al., *Anode, cathode, microbial catalyst*. 1999, Google Patents.

13. Bergel, A., D. Féron, and A. Mollica, *Catalysis of oxygen reduction in PEM fuel cell by seawater biofilm.* Electrochemistry Communications, 2005. **7**(9): p. 900-904.

14. Bond, D.R., et al., *Electrode-reducing microorganisms that harvest energy from marine sediments.* Science, 2002. **295**(5554): p. 483-5.

15. Cheng, S., H. Liu, and B.E. Logan, *Increased performance of single-chamber microbial fuel cells using an improved cathode structure.* Electrochemistry Communications, 2006. **8**(3): p. 489-494.

16. Pham, T.H., et al., *Improvement of cathode reaction of a mediatorless microbial fuel cell.* Journal of Microbiology and Biotechnology, 2004. **14**(2): p. 324-329.

17. Raghavulu, S.V., et al., *Effect of anodic pH microenvironment on microbial fuel cell (MFC) performance in concurrence with aerated and ferricyanide catholytes.* Electrochemistry Communications, 2009. **11**(2): p. 371-375.

18. Thrash, J.C., et al., *Electrochemical stimulation of microbial perchlorate reduction.* Environmental science & technology, 2007. **41**(5): p. 1740-1746.

19. Clauwaert, P., et al., *Biological denitrification in microbial fuel cells.* Environmental Science & Technology, 2007. **41**(9): p. 3354-3360.

20. Yan, H., T. Saito, and J.M. Regan, *Nitrogen removal in a single-chamber microbial fuel cell with nitrifying biofilm enriched at the air cathode.* water research, 2012. **46**(7): p. 2215-2224.

21. Logan, B.E., et al., *Microbial Fuel Cells: Methodology and Technology†.* Environmental Science & Technology, 2006. **40**(17): p. 5181-5192.

22. Popat, S.C., et al., *Importance of OH(-) transport from cathodes in microbial fuel cells.* ChemSusChem, 2012. **5**(6): p. 1071-9.

23. Yuan, Y., S. Zhou, and J. Tang, *In situ investigation of cathode and local biofilm microenvironments reveals important roles of OH- and oxygen transport in microbial fuel cells.* Environ Sci Technol, 2013. **47**(9): p. 4911-7.

24. Santoro, C., et al., *Effects of gas diffusion layer (GDL) and micro porous layer (MPL) on cathode performance in microbial fuel cells (MFCs).* International Journal of Hydrogen Energy, 2011. **36**(20): p. 13096-13104.

25. Rismani-Yazdi, H., et al., *Cathodic limitations in microbial fuel cells: An overview.* Journal of Power Sources, 2008. **180**(2): p. 683-694.

26. Grady, C.L., et al., *Biological Wastewater Treatment*. 2011: Iwa Publishing.

27. Picioreanu, C., et al., *A computational model for biofilm-based microbial fuel cells.* Water Res, 2007. **41**(13): p. 2921-40.

28. Rittmann, B.E. and P.L. McCarty, *Model of steady-state-biofilm kinetics.* Biotechnology and Bioengineering, 1980. **22**(11): p. 2343-2357.

29. Wanner, O. and W. Gujer, *A multispecies biofilm model.* Biotechnology and Bioengineering, 1986. **28**(3): p. 314-328.

30. Wanner, O. and P. Reichert, *Mathematical modeling of mixed-culture biofilms.* Biotechnology and bioengineering, 1996. **49**(2): p. 172-184.

31. Xavier, J.B., C. Picioreanu, and M.C. van Loosdrecht, *A general description of detachment for multidimensional modelling of biofilms.* Biotechnol Bioeng, 2005. **91**(6): p. 651-69.

32. Babauta, J.T., H.D. Nguyen, and H. Beyenal, *Redox and pH microenvironments within Shewanella oneidensis MR-1 biofilms reveal an electron transfer mechanism.* Environ Sci Technol, 2011. **45**(15): p. 6654-60.

33. Picioreanu, C., et al., *Model based evaluation of the effect of pH and electrode geometry on microbial fuel cell performance.* Bioelectrochemistry, 2010. **78**(1): p. 8-24.

34. Zhu, X., et al., *Microbial community composition is unaffected by anode potential.* Environmental science & technology, 2014. **48**(2): p. 1352-1358.

35. Reguera, G., et al., *Extracellular electron transfer via microbial nanowires.* Nature, 2005. **435**(7045): p. 1098-101.

36. Torres, C.I., A. Kato Marcus, and B.E. Rittmann, *Proton transport inside the biofilm limits electrical current generation by anode-respiring bacteria.* Biotechnol Bioeng, 2008. **100**(5): p. 872-81.

37. Mench, M.M., *Fuel cell engines*. 2008: John Wiley & Sons.

38. Benziger, J., et al., *Oxygen mass transport limitations at the cathode of polymer electrolyte membrane fuel cells.* AIChE Journal, 2011. **57**(9): p. 2505-2517.

39. Zhao, Y., *Effects of Oxygen Transport on Performance of Microbial Fuel Cell*, in *Environmental Engineering*. 2013, The Pennsylvania State University. p. 46.

40. Jung, S., M.M. Mench, and J.M. Regan, *Impedance characteristics and polarization behavior of a microbial fuel cell in response to short-term changes in medium pH.* Environmental science & technology, 2011. **45**(20): p. 9069-9074.

41. He, Z., et al., *Effect of electrolyte pH on the rate of the anodic and cathodic reactions in an air-cathode microbial fuel cell.* Bioelectrochemistry, 2008. **74**(1): p. 78-82.

42. Popat, S.C., et al., *Buffer pKa and Transport Govern the Concentration Overpotential in Electrochemical Oxygen Reduction at Neutral pH.* ChemElectroChem, 2014. **1**(11): p. 1909-1915.

43. NABIR, P., *Composition, reactivity, and regulation of extracellular metal-reducing structures (nanowires) produced by dissimilatory metal reducing bacteria.* 2005.

44. Strycharz-Glaven, S.M., et al., *On the electrical conductivity of microbial nanowires and biofilms.* Energy & Environmental Science, 2011. **4**(11): p. 4366.

45. Liu, H., R. Ramnarayanan, and B.E. Logan, *Production of Electricity during Wastewater Treatment Using a Single Chamber Microbial Fuel Cell.* Environmental Science & Technology, 2004. **38**(7): p. 2281-2285.

46. Logan, B., et al., *Graphite fiber brush anodes for increased power production in air-cathode microbial fuel cells.* Environmental science & technology, 2007. **41**(9): p. 3341-3346.

47. Newman, J. and K.E. Thomas-Alyea, *Electrochemical systems*. 2012: John Wiley & Sons.

48. Hirschenhofer, J., et al., *Fuel cell handbook.* 1998.

49. Marcus, A.K., C.I. Torres, and B.E. Rittmann, *Evaluating the impacts of migration in the biofilm anode using the model PCBIOFILM.* Electrochimica Acta, 2010. **55**(23): p. 6964-6972.

50. Bird, R.B., W.E. Stewart, and E.N. Lightfoot, *Transport phenomena*. 2007: John Wiley & Sons.

51. Kirby, B.J., *Micro-and nanoscale fluid mechanics: transport in microfluidic devices*. 2010: Cambridge University Press.

52. Heitjans, P. and J. Kärger, *Diffusion in condensed matter: methods, materials, models*. 2006: Springer Science & Business Media.

53. Eberl, H., et al., *Mathematical Modeling of Biofilms*. 2006, London, UK: IWA Publishing. 208.

54. Picioreanu, C., M.C. van Loosdrecht, and J.J. Heijnen, *Two-dimensional model of biofilm detachment caused by internal stress from liquid flow.* Biotechnology & Bioengineering, 2001. **72**(2): p. 205-218.

55. Pinto, R.P., et al., *Multi-population model of a microbial electrolysis cell.* Environ Sci Technol, 2011. **45**(11): p. 5039-46.

56. Picioreanu, C., J.U. Kreft, and M.C.M. van Loosdrecht, *Particle-Based Multidimensional Multispecies Biofilm Model.* Applied and Environmental Microbiology, 2004. **70**(5): p. 3024-3040.

57. Heijnen, J.J., *Impact of Thermodynamic Principles in Systems Biology*, in *Biosystems Engineering II*, C. Wittmann and R. Krull, Editors. 2010, Springer Berlin Heidelberg. p. 139-162.

58. Zeng, Y., et al., *Modelling and simulation of two-chamber microbial fuel cell.* Journal of Power Sources, 2010. **195**(1): p. 79-89.

59. Picioreanu, C., M.C. Van Loosdrecht, and J.J. Heijnen, *Mathematical modeling of biofilm structure with a hybrid differential-discrete cellular automaton approach.* Biotechnology and bioengineering, 1998. **58**(1): p. 101-116.

60. Kwok, W., et al., *Influence of biomass production and detachment forces on biofilm structures in a biofilm airlift suspension reactor.* Biotechnology and bioengineering, 1998. **58**(4): p. 400-407.

61. Kiely, P.D., et al., *Long-term cathode performance and the microbial communities that develop in microbial fuel cells fed different fermentation endproducts.* Bioresource Technology, 2011. **102**(1): p. 361-366.

62. Sukkasem, C., et al., *Upflow bio-filter circuit (UBFC): Biocatalyst microbial fuel cell (MFC) configuration and application to biodiesel wastewater treatment.* Bioresource technology, 2011. **102**(22): p. 10363-10370.

63. Wesselingh, J. and R. Krishna, *Mass transfer in multicomponent mixtures*. 2000: Delft University Press Delft.

64. Perry, R.H., et al., *Perry's chemical engineers' handbook*. Vol. 7. 1997: McGraw-hill New York.

65. Liu, H., et al., *Scale-up of membrane-free single-chamber microbial fuel cells.* Journal of Power Sources, 2008. **179**(1): p. 274-279.

66. Villadsen, J., J. Nielsen, and G. Lidén, *Bioreaction engineering principles*. 2011: Springer Science & Business Media.

67. Van't Riet, K., *Review of measuring methods and results in nonviscous gas-liquid mass transfer in stirred vessels.* Industrial & Engineering Chemistry Process Design and Development, 1979. **18**(3): p. 357-364.

68. Mackay, D. and W.Y. Shiu, *A critical review of Henry's law constants for chemicals of environmental interest.* Journal of physical and chemical reference data, 1981. **10**(4): p. 1175-1199.

69. Sander, R., *Compilation of Henry's law constants, version 3.99.* Atmos. Chem. Phys. Discuss., 2014. **14**(21): p. 29615-30521.

70. Yuan, Y., S. Zhou, and L. Zhuang, *Polypyrrole/carbon black composite as a novel oxygen reduction catalyst for microbial fuel cells.* Journal of Power Sources, 2010. **195**(11): p. 3490-3493.

71. Comsol, A., *COMSOL multiphysics user's guide.* Version: September, 2005.

72. Stewart, P.S., *Diffusion in biofilms.* Journal of bacteriology, 2003. **185**(5): p. 1485-1491.

73. Yuan-Hui, L. and S. Gregory, *Diffusion of ions in sea water and in deep-sea sediments.* Geochimica et cosmochimica acta, 1974. **38**(5): p. 703-714.

74. Rittmann, B.E., et al., *Results from the multi-species benchmark problem(BM 3) using one-dimensional models.* Water Science & Technology, 2004. **49**(11-12): p. 163-168.

75. Beun, J.J., et al., *Poly-β-hydroxybutyrate metabolism in dynamically fed mixed microbial cultures.* Water Research, 2002. **36**(5): p. 1167-1180.

76. McNaught, A.D. and A. Wilkinson, *IUPAC Compendium of chemical terminology*. 2000, International Union of Pure and Applied Chemistry.

77. Almasi, G.S. and A. Gottlieb, *Highly parallel computing*. 1989: Benjamin/Cummings publ. co. Redwood City (Ca).

78. Gropp, W., E. Lusk, and A. Skjellum, *Using MPI: portable parallel programming with the message-passing interface*. Vol. 1. 1999: MIT press.

79. Pacheco, P., *An introduction to parallel programming*. 2011: Elsevier.

80. Picioreanu, C., M.C. Van Loosdrecht, and J.J. Heijnen, *Effect of diffusive and convective substrate transport on biofilm structure formation: a two-dimensional modeling study.* Biotechnology and bioengineering, 2000. **69**(5): p. 504-515.

81. Lichtner, P.C., *Continuum model for simultaneous chemical reactions and mass transport in hydrothermal systems.* Geochimica et Cosmochimica Acta, 1985. **49**(3): p. 779-800.

82. You, S., et al., *A graphite-granule membrane-less tubular air-cathode microbial fuel cell for power generation under continuously operational conditions.* Journal of Power Sources, 2007. **173**(1): p. 172-177.

83. Malvankar, N.S., et al., *Tunable metallic-like conductivity in microbial nanowire networks.* nature nanotechnology, 2011. **6**(9): p. 573-579.

84. Ren, Z., et al., *Characterization of Microbial Fuel Cells at Microbially and Electrochemically Meaningful Time scales.* Environ. Sci. Technol., 2011. **45**(6): p. 2435.

85. Zhang, T.C. and P.L. Bishop, *Density, porosity, and pore structure of biofilms.* Water Research, 1994. **28**(11): p. 2267-2277.

86. Falkowski, P.G. and J.A. Raven, *Aquatic photosynthesis*. 2013: Princeton University Press.

87. Beun, J., et al., *Poly-β-hydroxybutyrate metabolism in dynamically fed mixed microbial cultures.* Water Research, 2002. **36**(5): p. 1167-1180.

88. Torres, C.I., et al., *Kinetic Experiments for Evaluating the Nernst−Monod Model for Anode-Respiring Bacteria (ARB) in a Biofilm Anode.* Environmental Science & Technology, 2008. **42**(17): p. 6593-6597.

89. Broka, K. and P. Ekdunge, *Modelling the PEM fuel cell cathode.* Journal of Applied Electrochemistry, 1997. **27**(3): p. 281-289.

90. Goldberg, R.N., N. Kishore, and R.M. Lennen, *Thermodynamic quantities for the ionization reactions of buffers.* Journal of physical and chemical reference data, 2002. **31**(2): p. 231-370.

91. Greenwood, N.N. and A. Earnshaw, *Chemistry of the Elements*. 1997: Elsevier.

92. Powell, K.J., et al., *Chemical speciation of environmentally significant heavy metals with inorganic ligands. Part 1: The Hg2+–Cl–, OH–, CO32–, SO42–, and PO43–aqueous systems (IUPAC Technical Report).* Pure and applied chemistry, 2005. **77**(4): p. 739-800.

93. Huang, L. and B.E. Logan, *Electricity generation and treatment of paper recycling wastewater using a microbial fuel cell.* Applied microbiology and biotechnology, 2008. **80**(2): p. 349-355.

94. Kelly, A.E., et al., *Low-conductivity buffers for high-sensitivity NMR measurements.* Journal of the American Chemical Society, 2002. **124**(40): p. 12013-12019.

VITA

Shiqi Ou was born in Yueyang, China. He obtained his B.S. degree in 2010 and M.S. degree in 2012 from the Department of Automotive Engineering at Dalian University of Technology, Dalian, China. He attended The University of Tennessee in 2012 to pursue his Ph.D. degree in Mechanical Engineering, and worked in Volvo Trucks North America Inc. as a Co-op engineer in 2015. He obtained his Ph.D. degree in 2015.